UNIVERSIDAD POLITÉCNICA DE MADRID
Escuela Técnica Superior de Ingenieros de Caminos, Canales y Puertos

Expanding the floating catalyst synthesis of inorganic 1D nanomaterials and their assembly into macroscopic networks

DOCTORAL THESIS

Submitted for the degree of Doctor by:

Isabel Gómez Palos
MSc. in Materials Engineering

Madrid, 2024

UNIVERSIDAD POLITÉCNICA DE MADRID
Escuela Técnica Superior de Ingenieros de Caminos,
Canales y Puertos

Doctoral Degree in Engineering of Structures, Foundations and Materials

Expanding the floating catalyst synthesis of inorganic 1D nanomaterials and their assembly into macroscopic networks

DOCTORAL THESIS

Submitted for the degree of Doctor by:

Isabel Gómez Palos
MSc. in Materials Engineering

Under the supervision of:
Dr. Juan José Vilatela
Dr. Álvaro Ridruejo

Madrid, 2024

Title: Expanding the floating catalyst synthesis of inorganic 1D nanomaterials and their assembly into macroscopic networks

Author: Isabel Gómez Palos

Doctoral Programme: Engineering of Structures, Foundations and Materials

Thesis Supervision:

Dr. Juan José Vilatela, Senior Researcher, IMDEA Materials, Madrid, Spain (Supervisor)
Dr. Álvaro Ridruejo, Professor, Universidad Politécnica de Madrid, Madrid, Spain (Supervisor)

External Reviewers:

Thesis Defense Committee:

Thesis Defense Date:

This thesis has been partially supported by the Madrid Regional Government under UPM/APOYO-JOVENES- F6TCCN-145-GGT34M, and a final stage by the European Commission under the ERC CONSOLIDATOR GRANT Universal processing route for high performance nanostructured yarns (UNIYARNS) under contract 101045394.

Para Álvaro y Alejandra

Acknowledgement

I want to express my gratitude to my supervisor, Juanjo Vilatela, for welcoming me into the team and giving me the opportunity to work on this charming yet challenging project. I'm grateful for his guidance, for encouraging me to become an independent researcher while always being available to talk about science and share his expertise with insightful advice.

I am also profoundly thankful for having Alvaro Ridruejo as my co-supervisor, for his generous support in helping me navigate Spanish academia and for his assistance with my migratory and professional journey.

Warm thanks go to my colleagues in the MNG group (and Floatech), whose friendship and caring spirit gave me much energy and will to continue. I'm impressed with all of you; you are great scientists! Special thanks to those with whom I collaborated directly and who own part of this Thesis. Ricardo, for being the first and for passing on hard-earned lessons, also for being the best flatmate ever! Miguel Vazquez, for teaching me all the "plumbing" skills and for your methodical and creative approach. Luis Arévalo, thank you for helping me with your expertise as a skilled reactor tamer. David, Mabel, Nabil and Raúl De, for taking the results further and sharing your vision.

I also extend my appreciation to the technical team and staff at IMDEA Materials, whose dedication ensures the institute's smooth and efficient operation. I am equally grateful to the administrative staff at UPM for their support in managing all the practicalities, allowing me to focus on my research. My thanks also go to the ANEE Group and Adam Boies for their warm hospitality and support during my time in Cambridge.

Finally, I am deeply grateful to the amazing individuals I have met during these years at IMDEA who have become friends. Above all, I wish to acknowledge the support and love of my family and life partner, whose understanding and encouragement have been vital throughout this process.

Abstract

Floating Catalyst Chemical Vapour Deposition (FCCVD) represents a promising method for assembling one-dimensional (1D) nanostructures into macroscopic materials for high-performance applications. This approach employs an aerosol of nanoparticles to catalyse the growth of high-aspect-ratio nanowires or nanotubes, which grow inside the reaction chamber floating in a gas stream. These nanostructures can aggregate into aerogels and then be shaped into freestanding macroscopic materials similar to nanotextiles.

Despite its promise, only a limited range of materials have been synthesised via this method. This thesis aimed to extend FCCVD synthesis to new materials, using silicon carbide (SiC) and tin oxide (SnO) nanowires, as model systems to deepen understanding of the nanowire growth mechanism and variables affecting FCCVD synthesis. Additionally, this work explores the challenges in reactor experimental setup, focusing on process monitoring, in-situ sampling, catalyst generation, and precursor injection stability.

The first phase (Chapter 3) was focused on SiC nanowires growth via FCCVD, achieving ultrafast growth rate up to 3 orders of magnitude above conventional substrate-based processes. The high aspect ratio (1800) of the nanowires favoured their entanglement into freestanding SiC nanowire networks. In situ collection of reaction products as they evolved through the reactor identified a 3-cm growth zone around 1130 °C. The use of hydrogen aided the inhibition of competitive products from precursor decomposition (Si, C and SiC nanoparticles), and promoted the catalysed formation of SiC nanowires, the only thermodynamically stable product in the Fe-Si-C system.

In the second phase (Chapter 4), the insights gained from SiC nanowire research were applied to the design and construction of a new FCCVD reactor to improve reproducibility and accelerate the synthesis parameter exploration. A thermal evaporator replaced the existing system, improving control over catalyst particle size and concentration. A nebulizer-based system was developed to quantify precursor delivery and prevent premature decomposition. Additionally, an in-line monitoring system using a scanning mobility particle sizer (SMPS) was implemented to track catalyst and precursor injection and product formation in real-time.

The final phase (Chapter 5) was dedicated to the synthesis of SnO nanowires in the newly developed FCCVD reactor. The setup enabled the isolation of distinct growth stages: precursor decomposition, Au-Sn alloying and nanowire growth. Low precursor concentration and the use of H_2 inhibited the formation of SnO_2 soot nanoparticles. SnO growth and improved selectivity were achieved only through careful synchronisation of species injection along the catalyst path. Studies with air injection showed that the tin content in the alloy catalyst particles during oxygen exposure strongly influences nanowire nucleation over catalyst deactivation by surface oxidation. Growth termination was attributed to oxygen gradients that cause rapid oxidation of the catalyst surface or inhibit the formation of an oxide layer in the nanowire. Finally, despite their short aspect ratio, self-standing sheets were prepared by a simple wet-processing method.

This thesis provides a comprehensive overview of nanowire growth using FCCVD, comparing SiC and SnO nanowires with existing literature. It demonstrates that FCCVD enables faster growth than substrate-based CVD due to higher impingement rates of precursor species on the catalyst, shifting the growth limitation from diffusion to incorporation and solidification. The study shows that selectivity towards 1D nanostructures increases under dilute conditions, particularly in a reductive atmosphere, by minimising competing homogeneous nucleation. Its results highlight the importance of increasing nanowire length to facilitate aerogel formation at feasible catalyst concentrations to enable the production of continuous nanowire fibres.

Resumen

La Deposición Química de Vapores con Catalizador Flotante (FCCVD) es un método prometedor para ensamblar nanoestructuras unidimensionales (1D) en materiales macroscópicos. Este enfoque utiliza un aerosol de nanopartículas para catalizar el crecimiento de nanohilos o nanotubos de alta relación de aspecto. Durante su crecimiento en la cámara de reacción, estas nanoestructuras pueden formar nanotextiles autosoportados.

A pesar de su potencial, solo pocos materiales han sido sintetizados mediante este método. El objetivo de esta tesis es extender la síntesis por FCCVD a nuevos materiales, utilizando nanohilos de carburo de silicio (SiC) y óxido de estaño (SnO) como sistemas modelo para profundizar en la comprensión del mecanismo de crecimiento y las variables que afectan la síntesis por FCCVD. Además, este trabajo aborda los desafíos en la configuración experimental usada hasta ahora.

La primera fase (Capítulo 3) se centró en el crecimiento de nanohilos de SiC mediante FCCVD. Este método condujo a un crecimiento ultrarrápido, hasta 3 órdenes de magnitud superior a los procesos convencionales en sustrato. Su alta relación de aspecto (1800) favoreció su ensamblaje en redes de nanohilos de SiC autosostenidas. La recolección in situ de productos de reacción, a medida que evolucionaban a través del reactor, permitió la identificación de la zona de crecimiento. El uso de hidrógeno ayudó a inhibir la formación de productos no deseados en la descomposición del precursor (Si, C y nanopartículas de SiC). Finalmente, se encontró que el único producto termodinámicamente estable de una nanopartícula de catalizador de Fe sobresaturada con C y Si es un nanohilo de SiC.

En la segunda fase (Capítulo 4), los conocimientos adquiridos durante la primera fase, se aplicaron al diseño y construcción de un nuevo reactor FCCVD. Un evaporador térmico reemplazó al sistema existente, ofreciendo un mayor control sobre el tamaño y la concentración del catalizador. Se desarrolló un sistema de inyección para cuantificar la alimentación de precursor y prevenir su descomposición prematura. Además, se implementó un sistema de monitoreo en línea para rastrear en tiempo real la inyección de especies y la formación de productos sólidos.

La fase final (Capítulo 5) se dedicó a la síntesis de nanohilos de SnO en el nuevo reactor FCCVD. La configuración permitió aislar distintas etapas de crecimiento: descomposición del precursor, aleación Au-Sn y crecimiento de nanohilos. La baja concentración de precursor y el uso de H_2 inhibieron la formación de nanopartículas indeseadas de SnO_2. La selectividad hacia nanohilos de SnO se logró a través de la sincronización de inyección de especies a lo largo del trayecto del catalizador. Se encontró que el contenido de estaño en las partículas de aleación antes de ser expuesto al oxígeno influye fuertemente en la formación de nanohilos frente a la desactivación del catalizador por oxidación superficial. Finalmente, a pesar de su corta relación de aspecto, se prepararon láminas autosoportadas mediante procesamiento en dispersión.

Esta tesis proporciona una visión integral del crecimiento de nanohilos mediante FCCVD, comparando los nanohilos de SiC y SnO con los datos existentes en la literatura. Demuestra que FCCVD permite un crecimiento más rápido que los métodos basados en sustrato debido a mayores tasas de colisiones de las especies precursoras en el catalizador, cambiando la limitación del crecimiento de la difusión a la incorporación y solidificación. El estudio muestra que la selectividad hacia nanoestructuras 1D aumenta bajo condiciones diluidas, particularmente en una atmósfera reductora, al minimizar la nucleación homogénea competitiva. Además, destaca la importancia de aumentar la longitud de los nanohilos para facilitar la formación de aerogeles a concentraciones factibles de catalizador, posibilitando la producción de fibras continuas de nanohilos.

Table of Contents

List of Figures

List of Tables

Abbreviations and Acronyms

1D	One dimensional
BNNT	Boron Nitride Nanotubes
CNT	Carbon Nanotubes
CVD	Chemical Vapour Deposition
DMA	Differential Mobility Analyzer
FCCVD	Floating Catalyst Chemical Vapour Deposition
GSD	Geometric Standard Deviation
HMDS	Hexamethyldisilane
HRTEM	High Resolution Transmission Electron Microscopy
MFC	Mass Flow Controller
NW	Nanowires
PES	Polyethersulfone
SAXS	Small Angle Xray Scattering
SCVD	Substrate Chemical Vapour Deposition
SDG	Spark discharge generator
SEM	Scanning Electron Microscopy
SiCNW	Silicon Carbide nanowires
SiNW	Silicon nanowires
SMPS	Scanning Mobility Particle Sizer
TGA	Thermal Gravimetric analysis
UPM	Universidad Politécnica de Madrid
VLS	Vapour-Liquid-Solid
WAXS	Wide Angle X-ray Scattering

1. Introduction

One-dimensional (1D) nanostructures, such as nanotubes and nanowires, are highly crystalline inorganic building blocks with elongated dimensions. Their diameter is typically on the order of nanometres, and their length ranges from hundreds of nanometres to several micrometres. Their large aspect ratio grants them exceptional axial properties, inherent defect tolerance and enormous surface-to-volume ratio.[1] However, assembling individual 1D nanostructures into macroscopic structures for applications like electrodes, membranes, or structural elements presents two main challenges, most notably producing high aspect ratio nanowires in very large amounts and with high selectivity.

Current synthesis and assembling technologies often involve long and precise processing, such as using templated lithography. Porous structures, such as anodic aluminium oxide, can be used to constrain the growth to only one direction inside the template channels. Similarly, pre-existing 1D nanostructures can become templates for new structures, by coating the surface with the desired material and later removing the inner structure. [2,3] These methods, while offering high precision, are not suitable for large-scale production due to their high cost and complex fabrication processes.

Other synthesis methods, like hydrothermal or electrodeposition, are often used for large production but require an additional assembly step where a large amount of solvent is needed to form a homogenous dispersion, which is later filtered. Gas-phase processing techniques like conventional CVD forests[4] are very effective in producing large amounts of oriented material in batches.

An emerging alternative is to continuously synthesise 1D nanostructures suspended in the gas phase and directly assemble them into macroscopic network materials. Floating Catalyst Chemical Vapour Deposition (FCCVD) follows the growth principle of CVD but eliminates the need for a substrate. Instead, a flowing aerosol of nanoparticles catalyses the synthesis of high-aspect-ratio nanoparticles (nanowires or nanotubes). These 1D nanoparticles can then aggregate to form an aerogel, which can be shaped into a freestanding macroscopic nanotextile. A schematic representation of the process is depicted in Figure 1.1.

In addition to its large production capacity, FCCVD significantly reduces the use of solvents and binders. In the manufacturing of anodes for lithium-ion batteries (LIBs), this reduction corresponds to an energy savings of approximately one-quarter of the total energy required for cell production, or nearly 50 kg CO_2-equivalent per kWh $^{-1}$.[5] This leads to electrodes with a high fraction of active material, which translates into enhanced properties such as higher conductivity and capacity in transparent conductors and energy storage applications.[5]

As a technology still under development, only a few materials have been synthesised with this method: carbon nanotubes (CNTs),[6] boron nitride nanotubes (BNNT),[7] gallium arsenide nanowires (GaAsNWs, both doped and undoped),[8] and more recently, silicon nanowires (SiNWs).[9] These achievements, though fruit of independent research efforts from various groups around the world, collectively highlight the inherent complexity of FCCVD yet also its potential for future advancements.

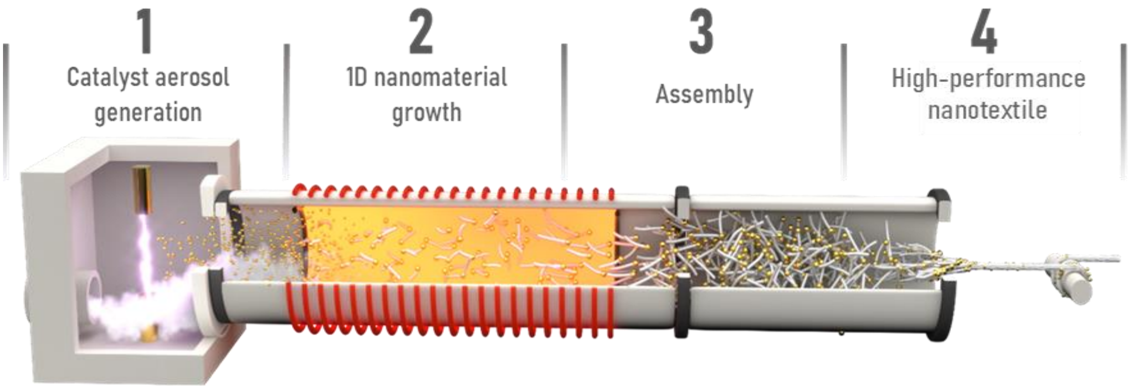

Figure 1.1 Schematic of a typical set-up for the synthesis of 1D nanoparticles based on the FCCVD method. The process begins with a catalyst aerosol generator, followed by a reaction zone where 1D nanoparticles grow, and then a section where assembly occurs, resulting in a nanotextile.

1.1. FCCVD History

The origins of FCCVD can be traced back to the 1980s when it was initially employed to produce vapour-grown carbon fibres (VGCFs) through the decomposition of carbon sources in a high-temperature, continuous flow reactor using transition metal catalysts.[10] This technique subsequently evolved into the synthesis of carbon nanotubes (CNTs), including controlled production of single-walled carbon nanotubes (SWCNTs) and initial scaling-up efforts. [11,12] A significant breakthrough occurred with the discovery that the addition of sulphur during FCCVD significantly increased CNT length, facilitating their entanglement in the gas phase and enabling the formation of freestanding strands.[13] Soon after, the exploration of reaction conditions and different catalyst materials led to the demonstration of spinning continuous macroscopic sheets and fibres directly drawn from the aerogels of CNTs -percolated network with ultra-low density- produced inside the FCCVD reactor.[6,14]

Inspired by the success of CNTs, researchers at Berkeley and the AFOSR successfully synthesised boron nitride nanotubes (BNNTs) using FCCVD. [7,15] Further developments in high-pressure plasma reactors substantially increased the growth rate and production capacity.[16] Numerous studies have since focused on the synthesis of BNNTs and the characterisation of their macroscopic ensembles.[17,18]

In parallel, Samuelson's research group at Lund University studied the gas-phase formation of crystalline compound nanoparticles. In 2012, they reported the growth of GaAs nanowires using a method analogous to FCCVD, which they named “aerotaxy”.[19] The process consisted in the use of an aerosol of gold nanoparticles as catalysts to grow GaAs nanowires in the gas phase. They did extensive research, focusing on achieving compositional control,[20,21] understanding and controlling flow patterns in continuous reactors,[8] and scaling up manufacture for optoelectronic applications.[22,23]

Most recently, Si nanowires (SiNW),[9,24] were successfully grown and assembled in the gas phase at IMDEA Materials facilities. FCCVD-produced SiNWs exhibit remarkable mechanical properties and exceptional electrochemical capacity for lithium-ion storage as battery anodes.[5]

1.2. The FCCVD Process

To fully understand the FCCVD process, we not only need to examine the similarities between the FCCVD-grown material synthesis, but also highlight the key differences between FCCVD and its parent process, conventional substrate-based CVD (SCVD). These seemingly subtle differences have profound implications for the reaction conditions and the resulting solid products. Table 1.1 summarises the main features of these two synthesis modes.

Table 1.1 FCCVD vs SCVD main features

	SCVD	**FCCVD**
	Reaction conditions	
Common growth mechanism	VLS	VLS
Reactor type	Close to CSTR	Plug flow reactor (PFR)
Residence time	≈ 3000 s	≈1-60 s
Pressure	high vacuum to atmospheric	close to atmospheric
Catalyst generation	Lithography, deposition on substrate	Aerosol
Reaction temperature (°C)	Limited by side reactions contaminating thin film	Allows higher Temp.
Growth velocity (nm s^{-1})	0.1 – 100	100 – 10^6
Catalyst particle size	Control through patterning	Limited control through aerosol selection
	Reaction products	
Ensemble format	Vertically aligned and attached to a substrate	From random to preferentially aligned networks
1D nanoparticle materials synthesised	> 70 (see Annex 1)	CNT, GaAs(P)NW, BNNT, SiNW, SiCNW

A fundamental difference between FCCVD and conventional SCVD lies in the reaction environment. In FCCVD, the catalyst aerosol, precursors and reaction gases, all flow through the reactor vessel, typically a ceramic tube. This reaction mode resembles a continuous tubular reactor typically idealised as a plug flow reactor (PFR). The temperature in this type of reactor is non-constant, with heating gradients that can go up to 50 °C. After they are fed at the inlet and travel through the reactor tube, the species evolve according to the temperature; three central moments are present in every FCCVD reaction: 1) Precursor decomposition and catalyst aerosol aggregation, which typically occurs during the heating ramp 2) Interaction precursor-catalyst and segregation of 1D nanostructure, near or at the hot zone and 3) aggregation and assembly, occurring right after and simultaneously with growth. Although the nature of the reaction is highly dynamic, all happen in very short residence times, typically less than 60 seconds.

The same growth takes 100 times longer in conventional SCVD. Very importantly, in SCVD, there is usually continuous precursor feed to the stationary catalyst, and the reaction zone temperature is nominally constant and uniform. This reaction mode resembles more to a continuous-stirred tank reactor (CSTR). Figure 1.2 shows a schematic representation of the two reactor modes.

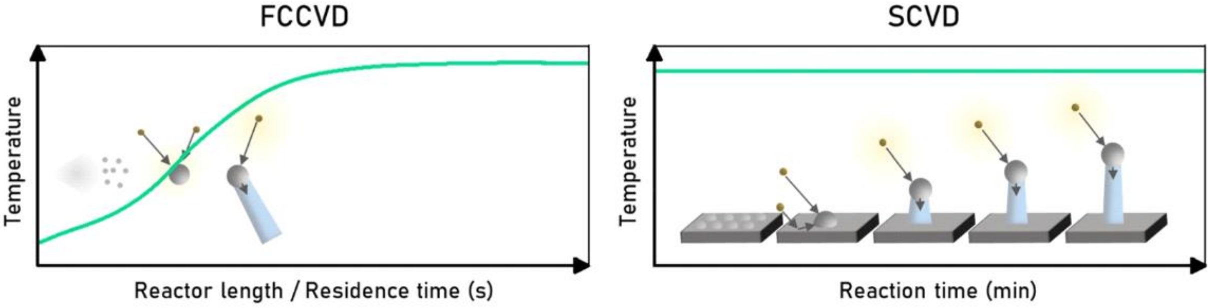

Figure 1.2. Schematic representation of FCCVD and SCVD reaction modes.

The FCCVD (and SCVD) process can be divided into 4 steps or subprocesses that are continuous and dynamic by themselves.

1) Catalyst generation
2) Precursor injection and decomposition
3) Nanowire growth
4) Self-Assembly and collection.

1.2.1. Catalyst Generation

For 1D nanostructures to grow, the catalyst requires to be a nanoparticle ranging typically 2 - 100 nm and the diameter of the catalyst particle is directly related to the diameter of the produced nanowire.

When a substrate is used, the catalyst material is typically deposited as a thin film on a substrate, followed by an annealing process (dewetting) to transform it into nanodrops. The diameter of these nanoparticles depends on the thin film's thickness and homogeneity. In most sophisticated studies, the substrate surface or thin film can be intentionally patterned employing lithographic techniques, achieving a predetermined size or spacing between the resulting nanoparticles.[2] Another common practice involves the use of a colloidal solution of nanoparticles or precursors containing the catalyst species, followed by a thermal treatment to evaporate undesired products. Regardless of the chosen method, the substrate undergoes various external processes, including cleaning, surface preparation, material deposition, and annealing, before being ready for nanowire growth. While some of these steps may not be technically complex, they are time-consuming, and the material production is limited to the small area of the substrate.

In contrast, FCCVD introduces the catalyst to the reaction chamber in the gas phase. This can be achieved by either generating the nanoparticles directly inside the reactor or introducing an external gas flow containing pre-formed catalyst particles.

CNT growth traditionally uses in situ formation of catalyst nanoparticles through the decomposition and nucleation of a precursor. Fe catalyst nanoparticles are formed from Ferrocene, which is in solution with the carbon supplier and an enhancer. The liquid precursors are introduced directly to the reactor through an aerosol-promoting injector. After the pyrolysis of ferrocene, iron atoms agglomerate until they form a particle with a size that can promote nanowire growth.

An external nanoparticle generator is preferred for the synthesis of Si nanowires by FCCVD. Schäufele *et al.* from IMDEA Materiales[9] generate an aerosol of gold particles via resistive heating of a gold source in an evaporation chamber. The evaporated catalyst is carried to the reaction chamber by a continuous gas flow while cluster formation occurs, increasing the size of the nanoparticle. However, this uncontrolled agglomeration process can lead to a broader nanoparticle size distribution, impacting the uniformity of the nanowire diameter.

Apart from the direct evaporation of metal sources, a spark discharge generator (SDG) can be used to generate catalysts of all conductive elements from the periodic table and their mixtures. SDG operates by applying high voltage between two electrodes to initiate a discharge event (spark) from the positive towards the negative electrode. Once the voltage reaches a critical threshold, a plasma channel forms, resulting in a spark that causes immediate vaporisation of the electrode surface upon impact. This method offers several advantages: it does not necessitate a crucible or expensive precursors, is not constrained by melting points, and can be executed at atmospheric pressure.

External catalyst generation provides high nanoparticle concentrations, typically higher than 10^5 cm^{-3} for the methods mentioned. Some strategies can be used to increase the production, such as increasing the resistance temperature or the frequency of the spark. However, increased particle concentration does not necessarily equate to higher number concentrations. If the aerosol concentration exceeds approximately 10^8 cm^{-3}, the particles will agglomerate to maintain concentrations below this threshold (Figure 1.3). In both cases, a large carrier gas flow is used to preserve a high concentration of smaller nanoparticles and prevent agglomeration before entering the reactor.[25,26]

To avoid the polydispersity of as-produced aerosols, Heurlin *et al.* from Lund University[19], employ a more sophisticated system to grow diameter-monodisperse GaAs nanowires. It consists of a high-temperature furnace for Au evaporation and formation of agglomerates, followed by a nanoparticle size selector with a particle charger and a differential mobility analyser (DMA), and finally, a sintering furnace to shape the round form of the nanocatalyst. This system allows the control of the nanowire diameter, quality and quantity.

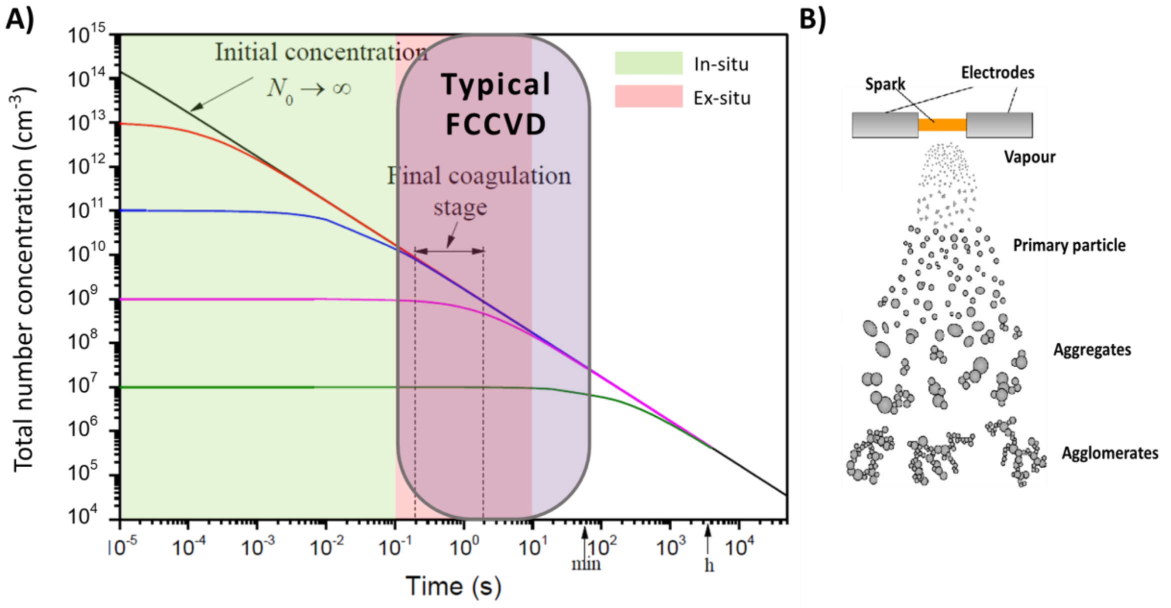

Figure 1.3 A) Total number concentration of the floating catalyst (aerosol)[27]. B) Scheme of the particle aerosol evolution, from [28].

1.2.2. Precursor Injection

The process begins with the selection of suitable precursors, typically gases or volatile compounds containing the desired elements for the target material. If the precursors are not gaseous initially, they are converted into a gaseous form, often through vaporisation or sublimation.

In SCVD, precursors are continuously fed onto the stationary catalyst, allowing for precise control over the precursor concentration and reaction conditions within the reactor. One of the primary challenges in SCVD regarding precursor utilisation is the formation of a “depletion layer”, where the local precursor concentration gradually decreases during nanowire growth. This depletion occurs due to the consumption of the precursor as it reacts with the catalyst. The diminishing precursor concentration results in reduced growth rates and non-uniformities in nanowire dimensions. Regions closer to the precursor source generally experience less depletion, leading to longer nanowires with larger diameters compared to those farther away.[29]

In contrast, FCCVD involves continuously injecting precursors into a flowing gas stream containing catalyst nanoparticles. The gas flow promotes efficient mixing between the precursors and catalyst nanoparticles, facilitating faster and more uniform reaction rates (discussed in the next section).

The specific method of precursor injection in FCCVD depends on the chosen precursor type and properties (e.g. viscosity, vapour pressure). Very low delivery rates, typically around 1 ml/h, are commonly used, presenting challenges in achieving uniform injection. The most common methods of precursor introduction to the reactor include:

- **Gas flow:** In general, it is preferable to use gas precursors, as is the case of Silane (SiH_4) or methane for Si nanowires and CNTs, respectively, to simplify the mixing and flow rate control.
- **Direct Liquid injection:** Liquid precursors are atomised using an injector nozzle before entering the hot zone of the reactor. Special attention must be paid to the vaporisation process to control the amount of precursor injected and achieve uniformity. Various types of injector nozzles can be used for efficient vaporisation, including Venturi effect nozzles[30], which operate on the Bernoulli principle, where a surrounding gas flow creates a low-pressure zone aiding in precursor vaporisation; heated systems can further assist in promoting vaporisation[31]; ultrasonic nozzles, which employ high-frequency waves to generate small droplets (aerosols) from the liquid precursor[32]; and electrospray nozzles, which employ an electric field for the same purpose.[33] The choice of nozzle type depends on precursor properties and the desired flow rate.
- **Bubbler systems for liquid and solid precursor:** This method is widely used in SCVD; the liquid or solid precursor (usually in powder form) is placed in a temperature-controlled zone inside the reactor or in an upstream vessel. A carrier gas then transports the precursor vapours into the reaction zone. Precautions must be taken to prevent unwanted condensation and to ensure consistent vaporisation. Solid salts can also be used in solution to enable liquid injection.

The selection and optimisation of the precursor injection method play a crucial role in achieving the desired nanowire characteristics, such as diameter, composition, and crystallinity. Typical injection flows in

Liquid metalorganic precursors are commonly used due to their volatility and tailored properties, particularly around organic ligands that can influence the decomposition behaviour.[34,35] This tool is especially useful when the catalyst is formed in situ, i.e., inside the reactor. The catalyst and target material precursor are introduced together, so their selection requires careful analysis. The process yield depends on individual decomposition temperatures and the ability to interact once the catalyst is prepared (Figure 1.4). Poor synchronisation of precursor decomposition can lead to the encapsulation of the catalyst in unwanted material clusters (e.g., amorphous carbon), affecting product quality and purity. Solely controlling the injection point can improve the size distribution, aspect ratio, crystallinity and conversion of CNTs.[36]

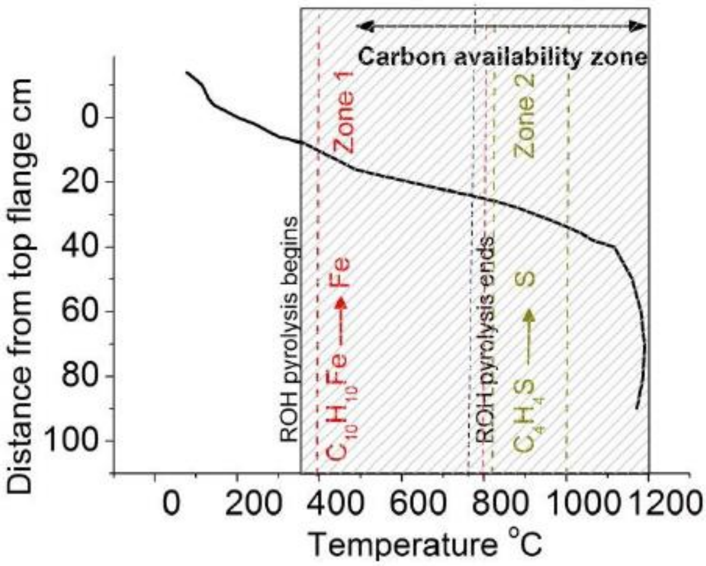

Figure 1.4 Decomposition temperatures of catalyst and enhancer-containing species along with the carbon availability zone in CNTs synthesis. Image from [37].

1.2.3. Nanowire Growth

The growth mechanism involved in either floating catalyst or substrate-based CVD is known as the Vapour-Liquid-Solid (VLS) mechanism, which takes its name from the fact that it requires a liquid catalyst nanoparticle and gas precursors to grow solid nanowires (Figure 1.5). The classic mechanism description proposes that the gas-phase precursors decompose upon contact with a metal catalyst nano-size droplet, acting as a collector. This process forms a metal alloy within the particle's liquid phase. As more material is collected, supersaturation is achieved, and the target material is extruded layer-by-layer in solid 1D structures to maintain solvothermal equilibrium. A steady state is sustained by the continuous supply of gas precursors, which ensures constant crystal growth.

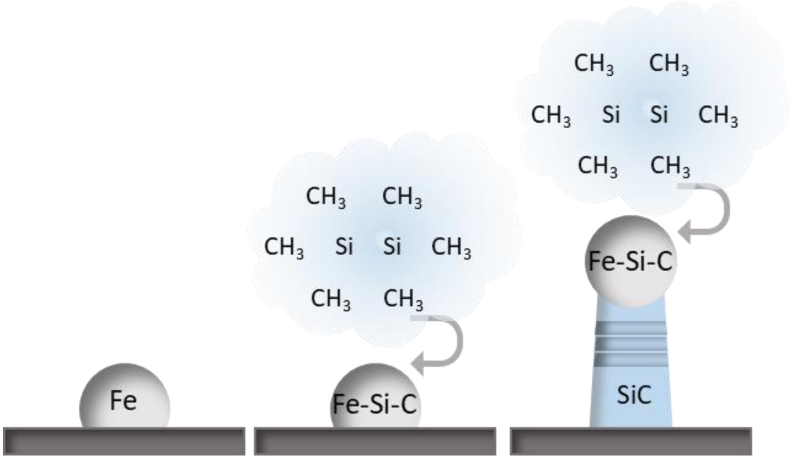

Figure 1.5 VLS growth mechanism diagram for SiC nanowires. The precursor containing Si and C decomposes and is absorbed by the Iron catalyst; after saturation, SiC is extruded.

From a thermodynamic point of view, the liquid catalyst particle ($\mu_{catalyst}$) should have a lower chemical potential than the precursors in the gas phase (μ_{vapour}) but larger than the solid crystal phase to grow (μ_{solid}). In this way, the driving force goes from the vapour to the liquid particle to the precipitation of a solid. [38]

$$\mu_{vapor} > \mu_{catalyst} > \mu_{solid}$$

Nevertheless, this model does not explain the rapid and unidirectional growth of the nanowires. Recently, more explanations of the catalytic effect have been developed based on preferential interface nucleation. This preferential site would be the interface of the three phases involved in the process (precursor vapour, catalyst and solid crystal). Therefore, the nucleation and growth of nanowires are mainly produced at this point, while the vapour-solid nucleation is reduced.[39]

For the VLS mechanism to occur, the catalyst particle and the desired nanowire material must comply with two requirements: 1) they must present a suitable solubility, and the mixture of the species should be described as a eutectic system where, at a certain composition and temperature, a stable liquid phase forms. And 2) The eutectic point (the lowest temperature at which the two materials can form the liquid phase) must lie within the temperature and pressure range the experimental setup can provide. This ensures that the catalyst is in a liquid state at the working conditions, allowing the material to dissolve into the catalyst and precipitate as a nanowire.

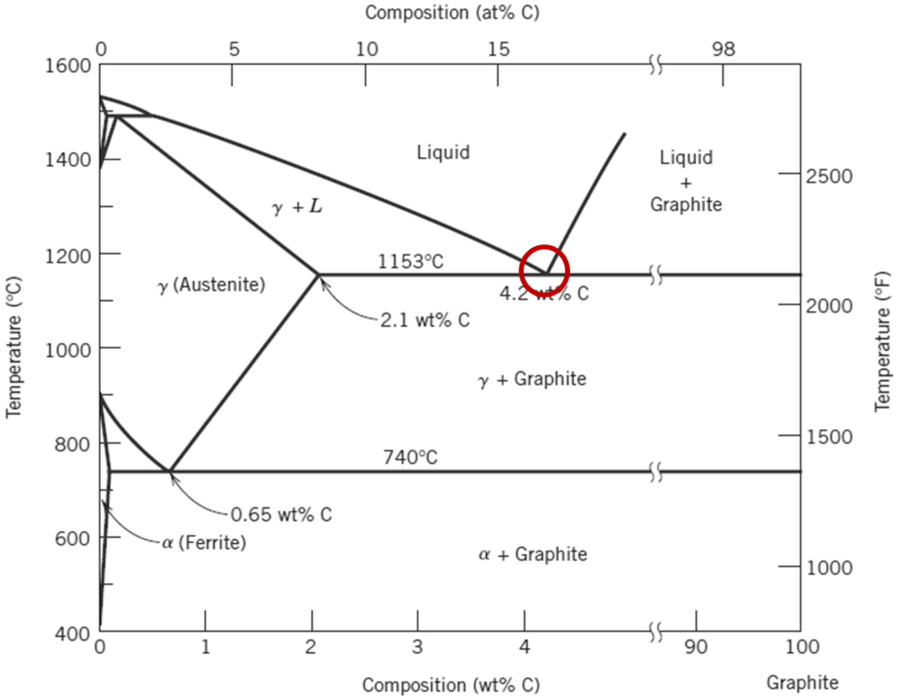

Figure 1.6 Iron-Carbon phase diagram. Modified from ref [40].

The phase diagram in Figure 1.6 is presented as an example, it corresponds to the equilibrium phases of iron and carbon mixtures. The eutectic point (circled in red) is achieved at 1147 °C and it allows 4.3 % of carbon in the liquid alloy. If we keep the temperature constant and the concentration of carbon increases due to the decomposition of carbonaceous materials in the gas phase into the liquid catalyst, the liquid alloy will follow a supersaturation state that ends up in the extrusion of solid material in the form of a carbon nanotube to find the equilibrium.

Analysing the nanowire nucleation process as a solidification of a bulk alloy is a simplification, but some experimental observations argue in favour. For example, the minimum experimental temperatures used for the growth of various nanotubes and nanowires by FCCVD are close to the eutectic temperature on the corresponding phase diagram (see Table 1.2).

Some studies[41–43] have reported the growth of nanowires at temperatures below the eutectic point, where the catalyst remains in the solid state, called vapour-solid-solid (VSS) growth. In such cases, the precursor either diffuses through the solid catalyst or migrates along its surface. Since diffusion in the solid phase is significantly slower than in the liquid phase, this process leads to at least one order of magnitude lower growth rates compared to VLS growth.

The growth mechanism becomes more complex in the case of 1D nanostructures made of more than one element. In binary nanowires, the two elements usually have different solubilities in the catalyst.[44] Often, one element mixes easily with the metal, while the other barely does. This means that during growth, the nucleation happens because of the supersaturation of the more soluble one, while the nanowire layer growth depends on the availability of the less miscible species.[41]

GaAs and SnO_2 nanowires with gold catalyst are examples of this. At the synthesis temperature, the catalyst can only form an alloy with Sn or Ga, as oxygen and arsenic have a very low solubility in Au. SnO_2 nanowires are formed because surrounding oxygen bonds preferentially with Sn. After the bond O-Sn-O is formed, their insolubility and high melting point result in the formation of a solid SnO_2 flake floating on the surface of the catalyst and acting as the seed for further nanowire growth (Figure 1.7 A).[45] In the case of GaAs, the incorporation of mainly Ga creates a Ga-rich surface layer on the liquid droplet. As As atoms reach the Ga-Au interface, they react with Ga to form GaAs, and the alloy becomes rapidly supersaturated, leading to the precipitation of a GaAs crystal (Figure 1.7 B). [46,47]

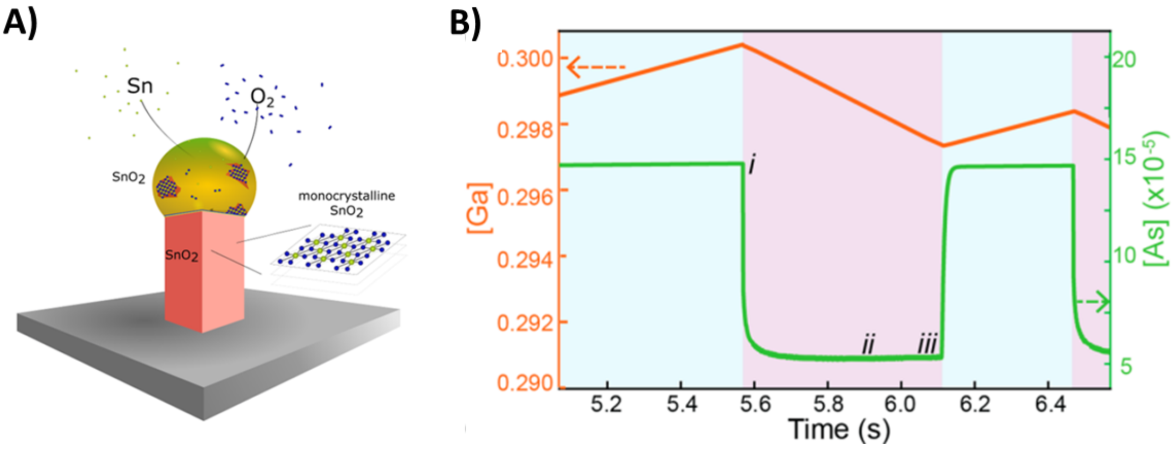

Figure 1.7 A) Schematic representation of tin oxide flake formation in the Au-Sn catalyst surface. Image from [45] B) Ga and As concentration (simulated) in the catalyst droplet as a function of time. The plot shows that the As concentration is orders of magnitude lower than the Ga concentration and depletes with the formation of each GaAs crystal layer. Image from [46]

While both SCVD and FCCVD rely on the VLS mechanism for nanowire growth, the resulting rates differ significantly, with FCCVD achieving orders of magnitude faster growth. This trend has been observed for all nanowires and nanotubes produced with this method so far. For instance, the average growth rate of Si nanowires grown with gold catalyst particles floating in the gas phase can reach 1400 nm/s, which is two orders of magnitude higher than conventional Au-catalysed SCVD growth of SiNWs, typically at around 2 to 15 nm/s. A similar velocity increase has been reported for CNT and GaAs nanowires.[9] Although not fully understood, the interaction between precursor-catalyst is a key factor.

Two major transport pathways have been suggested for the supply of precursor species to the catalyst in nanowire growth by CVD; one is the direct impinging of incoming atoms, and the other is the migration of adsorbed atoms by diffusion on the surface.

SCVD, usually performed at low pressure, is often described as a diffusion-limited[48] process, that is not surprising as the probability of the species for being adsorbed into a large-surface Is larger than the direct interaction with the catalyst. In this case, the growth rate follows a dependence of the form r^{-p}, where r is the catalyst radius and p is an exponent between 0.5 and 2 depending on growth conditions (Figure 1.8 A, B).[49]

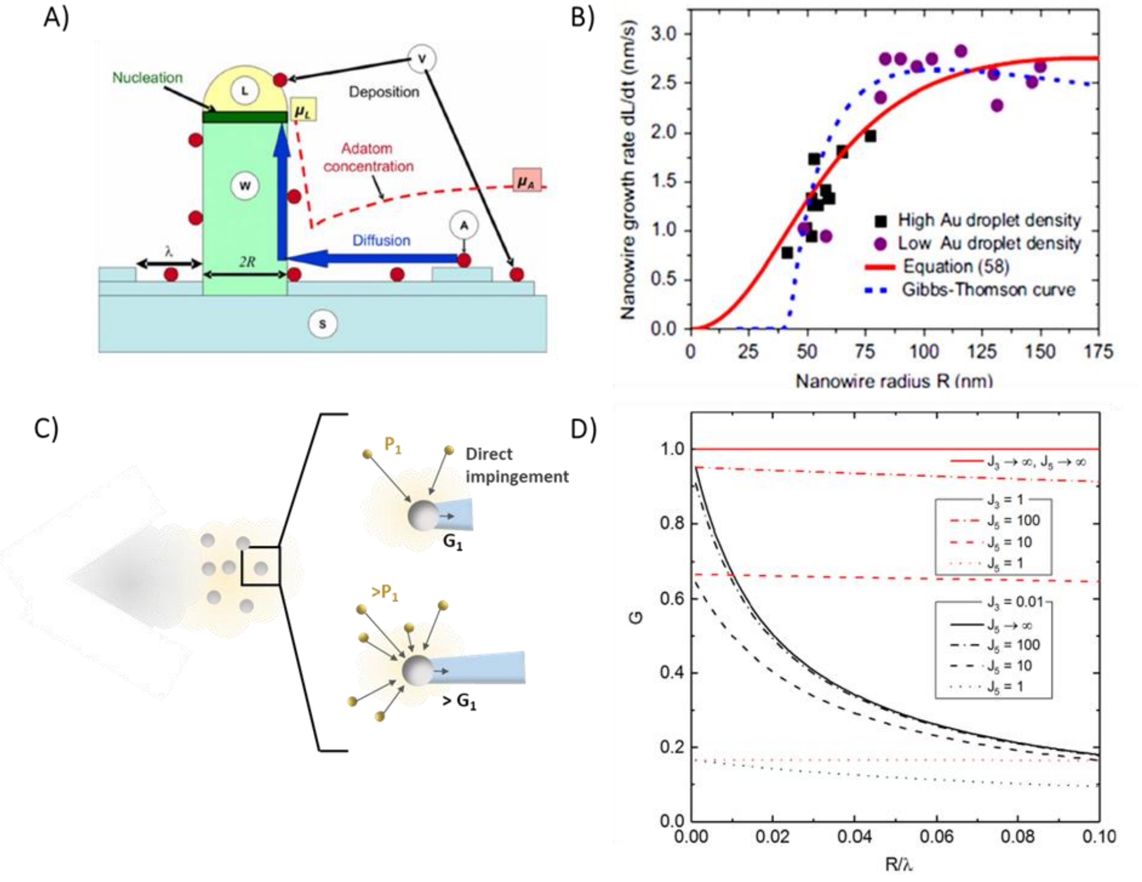

Figure 1.8 Dependence of nanowire growth rate for different VLS growth modes A) SCCVD is a diffusion-limited process,[48] C) whereas FCCVD growth is mainly contributed by direct impingement. B) Dependence of the nanowire rate with the radius of the substrate-supported catalyst.[49] D) In FCCVD, precursor partial pressures are sufficiently high, therefore the nanowire is limited by the incorporation kinetics, with no radius dependence, as depicted by the red lines at high impingement rates for both group III and V precursors (J_3 and J_5, respectively).[51]

Re-evaporation also plays a crucial role, when adatoms re-evaporate from the substrate, they can either get attached to the nanowire sidewall and evaporate again, or go out to the outer system. The escape probability of the atoms depends on the ratio between the nanowire length and the inter-wire spacing, thus, the growth rate finds a maximum when the nanowire arrange is able to trap re-evaporated atoms increasing the probability of their incorporation into the catalyst.[50] In such description, impingement of precursors or adatoms directly on the catalyst is explicitly neglected.

Without a substrate, the direct impinging of the species is the main pathway for the incorporation of atoms into the catalyst (Figure 1.8 C). The growth rate of GaAs,[8] and SiNWs[9] at higher pressures shows no such dependence on nanowire radius as seen in studies of SCVD at high pressure[51], the conditions used so far in FCCVD (>100 Pa) lead to a growth limited by adatom incorporation, as illustrated in Figure 1.8 D, where the increase in impingement rate of the group III precursor shifts the trend from diffusion-limited growth (black solid line) to incorporation-limited (solid red line).

Furthermore, even at similar and relatively high pressure, hence, both limited by the rate of impingement, FCCVD and SCVD are expected to have different collision rates of precursor molecules (or their derivatives) on the catalyst. When the catalyst is positioned statically, the precursor species need to travel further than when the catalyst travels along in the gas phase. For FCCVD, both the catalyst and the precursor are mobile and collide more effectively in the gas phase, explaining the extraordinarily fast growth rate.

Table 1.2 Reaction Conditions for FCCVD-grown 1D nanoparticles

Material	Catalyst	Temperature	Eutectic temperature (phase diagram)	Residence time	Catalyst concentration
Si	Fe	650 °C	360 °C (Au-Si)	10 s	10^{7} cm^{-3}
GaAs	Au	425 - 625 °C	350* °C (Au-Ga)		10^{6} cm^{-3}
BNNT	Ni	1200 °C	1018 °C (Ni-B)	167 s	10^{6} cm^{-3}
CNT	Fe	1050 - 1250 °C	1147 °C (Fe-C)	53 s	10^{6}-10^{9} cm^{-3}

*Lowest temperature for liquid mixture in the Ga-Au system also presents a eutectic point at 450 °C.

1.2.4. Self-assembly and product collection

Following nanowire growth, the collection method significantly impacts the material's final arrangement, properties and use. SCVD can produce well-aligned nanowires that are efficiently connected to the growth substrate. This characteristic makes SCVD ideal for applications in integrated electronics, where precise positioning and defined connections between nanowires are crucial for device functionality.[52,53]

On the other hand, for 1-D nanostructures growing in the gas phase, there are various strategies to recover the nanowires from the reaction stream. In the FCCVD significantly diluted synthesis of GaAs NW, the spare nanowires (Figure 1.9 A) are recovered efficiently, employing substrates in an electrostatic precipitator that takes advantage of the previously charged catalyst particle. Nevertheless, the synthesis conditions used in this example are far from conventional because, due to the precise selection of catalyst diameter, the concentration of produced nanowires was very low. When more common synthesis conditions are used (see Table 1.3), the nanowires or nanotubes get entangled as they grow, forming aggregates. In SiNW synthesis, these aggregates are continuously collected downstream via filtration using a conventional porous paper. The final product is a self-standing and homogenous nanotextile (Figure 1.9 B) that can be used readily as an electrode.

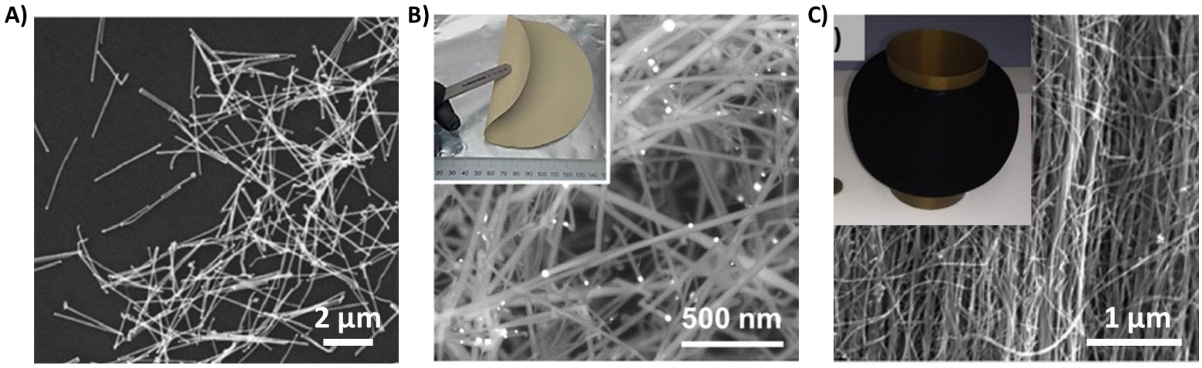

Figure 1.9 FCCVD grown materials collection A) GaAsP NW collected with electrodeposition on Si substrates. Image from [54] B) Si NW collected by filtration image from[27] C) CNTs collected by direct spinning. Image from [55]

At certain concentrations and nanoparticle lengths, the aggregates keep growing to form a full aerogel. In CNT synthesis, the ultra-long nanoparticles form a well-defined aerogel inside the reaction chamber that can be extracted by continuous, direct spinning from the gas phase to a meter-scale long fibre (Figure 1.9 C).

The ability to form aerogels in FCCVD is believed to be a consequence of the collision dynamics between the nanowires. Boies et al. have recently studied the kinetic base of the aerogel formation.[56] The work employed simulations and direct calculations to determine the first collision kernel of 1D nanoparticles considering their rotation, translation and geometric parameters, such as length.

This analysis revealed that FCCVD-grown nanowires typically fall into an intermediate regime where rotational and translational timescales are comparable.[56] Furthermore, the study suggests that collisions are enhanced for nanowires with a high difference in lengths and are 10 times higher than collisions between spherical nanoparticles.

Percolation theory is helpful to describe the conditions leading to formation of an aerogel of 1D nanoparticles. In a first approximation, Schäufele et al.[9] estimated the percolation threshold of individualised nanowires in a tubular reactor volume. The volumetric concentration (v) and aspect ratio (s) of the nanowires can be related to the probability of forming a continuous, interconnected network (aerogel). For ideal rod-shaped particles, a critical product of volume and aspect ratio (v·s) exists (0.5 s^{-1}), above which aerogel formation becomes favourable.[9]

Table 1.3 includes a comparison of v·s values for various FCCVD. The table highlights the wide range of operating conditions used with FCCVD and how these conditions translate into distinct macroscopic material formats. Lower v·s values favour the formation of individual nanowires, which can be subsequently assembled into specific arrangements for applications like thin layers. Conversely, higher v·s values promote the formation of macroscopic aerogels suitable for processes like continuous fibre spinning.

This concept provides a valuable future tool for predicting and controlling the material's final form (aerosol or aerogel) based on the FCCVD growth conditions.

Table 1.3 FCCVD 1D nanoparticle characteristics and reaction throughput.

Material	Mean Diameter	L	Growth rate	Aspect Ratio	Throughput	Volume concentration	(v·s)	Product Type
Si	20 nm	4.28 µm	1400 nm/s	214	0.2 g/h	2×10^{-8}	4.7×10^{-6}	Fabric
GaAs	65 nm	1.3 µm	1000 nm/s	20		2×10^{-9}	4×10^{-8}	Thin Film
BNNT	2 nm	10 µm		5000	0.02 g/h	1.1×10^{-5}	5.3×10^{-2}	Fibre
CNT	1.9 / 7.1 nm	7.6 / 234 µm	10^4-10^5 nm/s	4000 / 33000	0.06 g/h	$10^{-12}/10^{-7}$	6.2×10^{-9} /2.5×10^{-2}	Powder / Fibre

1.3. Throughput, size and morphology control

Chemical vapour deposition (CVD) based growth is generally considered a scalable approach for producing 1D nanoparticles. Floating catalyst chemical vapour deposition (FCCVD) offers an attractive example of this scalability. Vertically aligned carbon nanofiber (VACNF) or vapour-grown carbon fibre (VGCF) production is the longest-standing example of a large-scale FCCVD process. Industrial-grade VGCFs have been commercially available for decades, with production facilities established for years. As early as 2001, reports indicated production capacities were tens of tons per site.[57]

At the laboratory scale, FCCVD demonstrates significantly higher production capacities compared to traditional techniques. For instance, FCCVD furnaces can produce GaAs nanowires at a rate of 10^{11} nanowires per hour, which is 50 times higher than what can be achieved using a substrate-based approach in a similar experimental setup.[58] Nevertheless, this production capacity does not compete with industrial capacity.

Studies on CNTs have identified that achieving significant throughput will require not only improvements in conversion and collection efficiency but also substantial increases in both precursor and catalyst concentrations within the reaction zone. [59]

While FCCVD offers advantages in terms of product assembly and throughput, achieving precise control over the size, morphology, and selectivity of the nanowires during growth is crucial for optimising their properties for specific applications.

The diameter of the catalyst particle directly influences the diameter of the resulting nanowire. In FCCVD, unlike substrate-based CVD, where seed particles can be precisely controlled, catalyst nanoparticles are formed as an aerosol with an inherent broad size distribution (as shown in Figure 1.10).

Strategies like particle size selection or in-line sintering can be used to narrow the size distribution of catalyst particles. However, these methods often come at the cost of reducing the overall catalyst concentration, which contradicts the advantage of high throughput in FCCVD.

Furthermore, preserving the desired (narrow) size distribution of the catalyst aerosol throughout the FCCVD reactor proves challenging. The high operating temperatures and particle concentration can lead to particle coalescence, where smaller particles merge into larger ones, further broadening the size distribution. Any aerosol tends to converge towards a single-size distribution in times shorter than the typical residence time in the reactor (1-60 s)

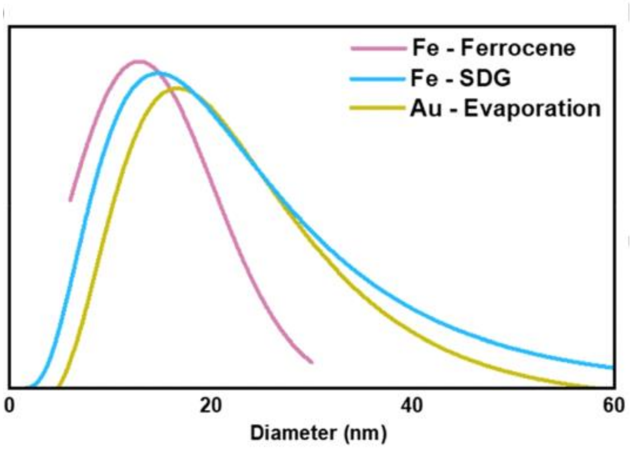

Figure 1.10 Broad catalyst size distributions for different aerosol generation methods: In-situ (ferrocene) and ex-situ (SDG, evaporation).[27]

Controlling the inner and outer diameters of nanotubes presents an even greater challenge. It has been achieved through the control of injection of precursors and gases,[36] optimisation of residence times,[60] and introduction of group 16 elements.[61]

While some progress has been made, achieving truly monodisperse diameter distributions remains a significant hurdle, particularly for optoelectronic applications. Composition and crystal control in FCCVD is rather unexplored. The research of Lund University in doped and undoped GaAs NW sets a good starting point. Similar to substrate-based CVD, the work by Sivakumar et al.[8] demonstrates that the growth temperature in FCCVD can influence the crystallographic phase of the nanowires. The wires have a base filled with dense stacking faults under all investigated growth conditions, which they attributed to the higher precursor partial pressure that promotes faster nucleation in the seed particle before unidirectional growth.

They also manage to vary the composition of the nanowires by doping them with P by adding small quantities of dopant precursor to the catalyst in the alloying zone.[20] And took it even further, synthesising core-shell structures and *pn*-junctions[23] by adding consecutive growth chambers in series.

1.4. Undesired Products and Selectivity

While our discussion has thus far focused on one-dimensional (1D) growth, the inherent dynamic nature of FCCVD leads to a variety of products beyond the desired 1D nanostructures. In fact, the specific conditions that promote nanowire growth represent a relatively narrow window within the broader range of achievable parameters in FCCVD reactors.

Current FCCVD processes typically operate under conditions with very low precursor concentrations, which is favourable for vapour-liquid-solid (VLS) growth. However, the short residence time of species within the reactor can lead to a multitude of undesired reactions. These reactions include the nucleation and growth of non-catalyst-mediated solids, unwanted interactions with the catalyst, unintended surface reactions (e.g., with reactor walls), and even significant gas-phase reactions. A visual representation of these potential pathways is depicted in Figure 1.11 A. These unwanted reactions may not only contaminate the final product but also contribute to precursor depletion[62] or promote unproductive decomposition pathways,[63] thus hindering 1D growth. This section will delve deeper into these challenges and explore strategies for enhancing selectivity towards 1D growth.

Non-catalysed solids essentially refer to nanoparticles that nucleate either in the gas phase or as a layer on top of any surface, including the reactor wall or the already-formed nanoparticle. While various catalyst-free methods aim to generate similar nanoparticle aerosols, they are deemed undesirable impurities analogous to carbon soot when creating macroscopic network materials. Instances of "soot" particles of GaAs, Si NW, and CNTs are evident in the synthesis of various nanowires by FCCVD, as depicted in Figure 1.11 B.

Controlling the formation of soot over nanowires is paramount. For example, in the Au-catalysed synthesis of Si NW, the low temperature during nanowire growth ensures that the formed Si soot remains amorphous, facilitating discrimination between the two products, even only looking into the colour of the samples. Later, quantification of the mass fraction of each product can be done, for instance, using Raman spectroscopy and XRD.[64] The facile discrimination of the products allowed Schäufele et al. to find an optimum and rather low SiH_4/H_2 ratio, where nearly 100% selectivity to SiNWs can be achieved. Higher silane concentration produced increasingly more nucleation of amorphous nanoparticles, *i.e.*, Si soot.

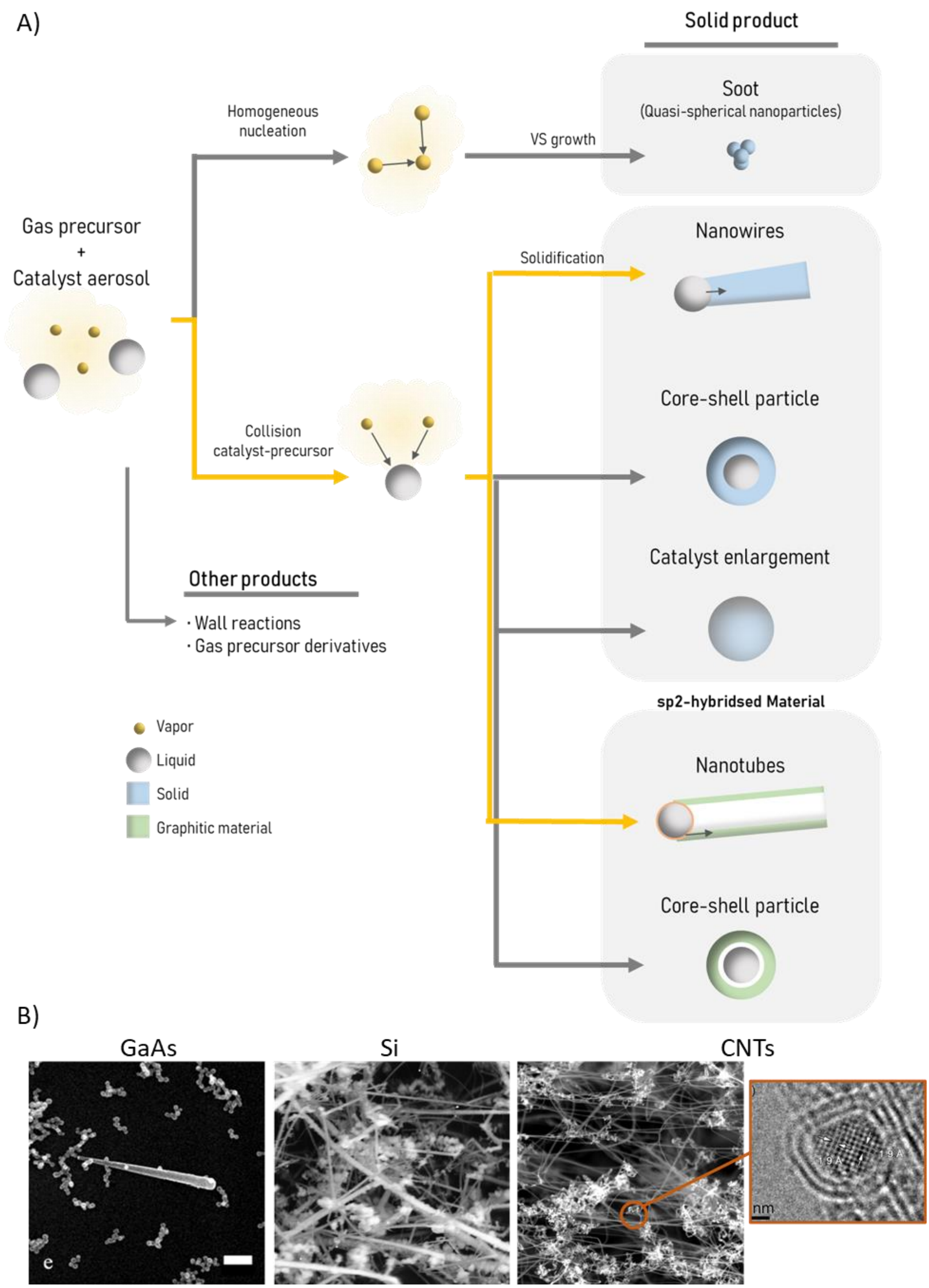

Figure 1.11 A) Reaction routes in FCCVD and main products and B) Examples of Soot in the synthesis of different materials by FCCVD. Both figures adapted form [27]

Then, together with a simple understanding of the decomposition route for SiH_4, they were able to describe the role of hydrogen in controlling reaction selectivity for SiNWs. As illustrated in Figure 1.12, hydrogen plays a crucial role in inhibiting the decomposition of silane into derivatives that would otherwise polymerise into amorphous Si nanoparticles. For the first time, the experimental data for conversion and selectivity, combined with literature kinetics on non-catalysed Si formation, were incorporated into an expression for FCCVD growth velocity of nanowires based on the reaction mechanism of the silylene radical with gold.

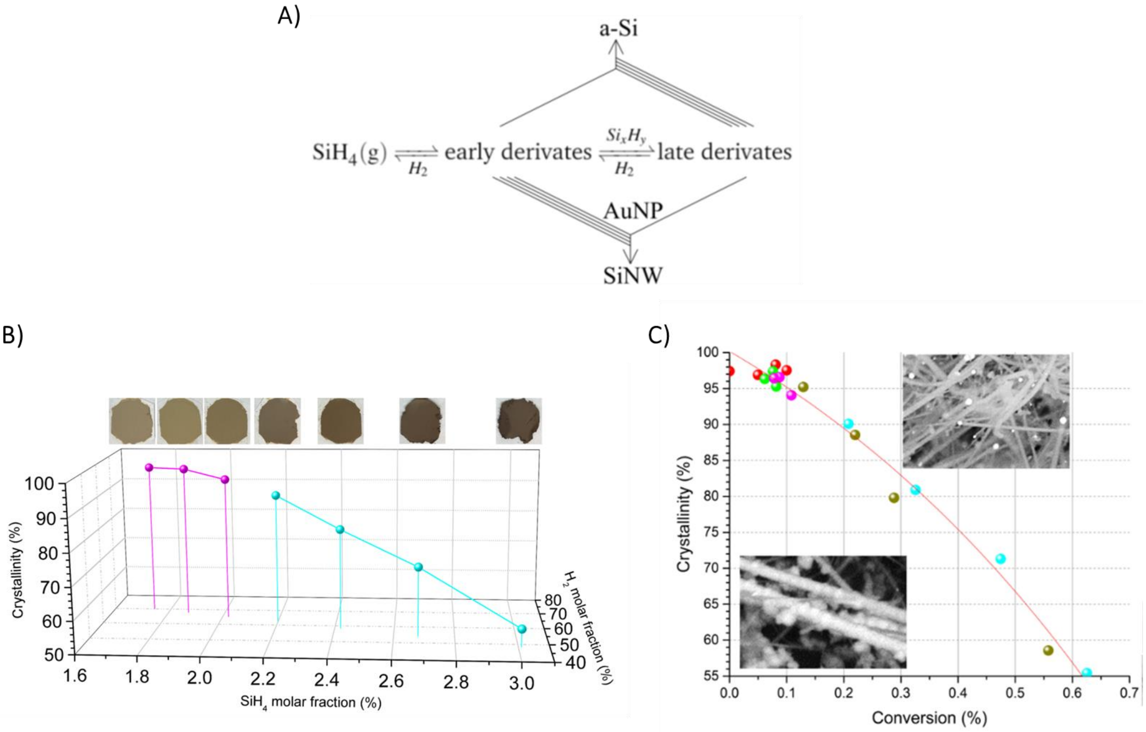

Figure 1.12 Role of Hydrogen in the prevention of Si soot formation. [64] A) Proposed model where an H_2 atmosphere inhibits the decomposition of silene into soot-forming derivatives. B) Decrease of crystallinity (e.g. nanowire formation) at low H_2 content and high precursor concentration. C) High crystallinity (almost 100% of nanowires) obtained at very low precursor conversion.

The synthesis parameters to control selectivity towards CNTs in FCCVD have been more extensively studied; different precursors, catalysts and promoters have been tested.[65] Although the experimental setup plays a significant role[14], certain findings are present across different configurations. At very low concentrations of the carbon source, soot formation is suppressed. Shorter residence time has also been shown to favour CNT formation over soot, likely due to the different hydrocarbon pyrolysis products involved in the reaction. To preserve the controlled breakdown of the carbon source, H_2 has been used in at least some percentages of the carrier gas. H_2 also plays a role in delaying catalyst precursor (ferrocene) decomposition and etching the solid carbon already formed.[66]

Unwanted products involving the catalyst, such as core-shell particles, catalyst poisoning, or enlargement, can also arise. In CNT synthesis, for instance, a graphitic shell will likely grow around the catalyst, leading to encapsulation and prevention of CNT growth. This phenomenon is attributed to the growth of sp^2-hybridized crystals in the absence of a substrate interface.

This encapsulation has been attributed to low temperatures, where the graphitic layers on the catalyst lack sufficient kinetic energy to lift off from the particle surface and promote CNT wall growth.[67] Other studies have focused on the solubility of carbon in the metal catalyst; they suggest that higher adhesion energy, due to increased wettability in low-carbon-containing catalysts, also contributes to encapsulation.[68]

Smaller catalyst particles may not gather enough carbon to form a complete encapsulating layer and tend to produce CNTs more efficiently. Moreover, promoters, such as sulphur, used in CNT growth by FCCVD are believed to form biphasic catalyst particles,[61,69] potentially reducing encapsulation probability.

The ternary phase diagram of Fe-S-C (Figure 1.13 A) provides a valuable tool for understanding this phenomenon. It reveals that the catalyst can exist in two key states at synthesis temperature. The first is a Fe-rich liquid (L), from which CNTs can grow. The second state consists of two immiscible liquids, one rich in carbon (L1) and the other in sulphur (L2), the latter is detrimental to CNT growth because it reaches equilibrium with solid carbon and therefore promotes the formation of a graphitic shell around the catalyst particle[70]. Reguero *et al*. proposed that most Fe particles quickly saturate with C during their trajectory through the reactor. Consequently, by the time they encounter S, their concentration of C is already very high, overshadowing the optimal compositional range for CNT growth (represented by the L phase in the diagram). Conversely, the very small proportion of active particles would be those in which S diffusion occurred at lower concentrations, where the liquid is not in equilibrium with C. Therefore, upon saturation of the catalyst particle, the incoming carbon would be extruded to form a CNT.

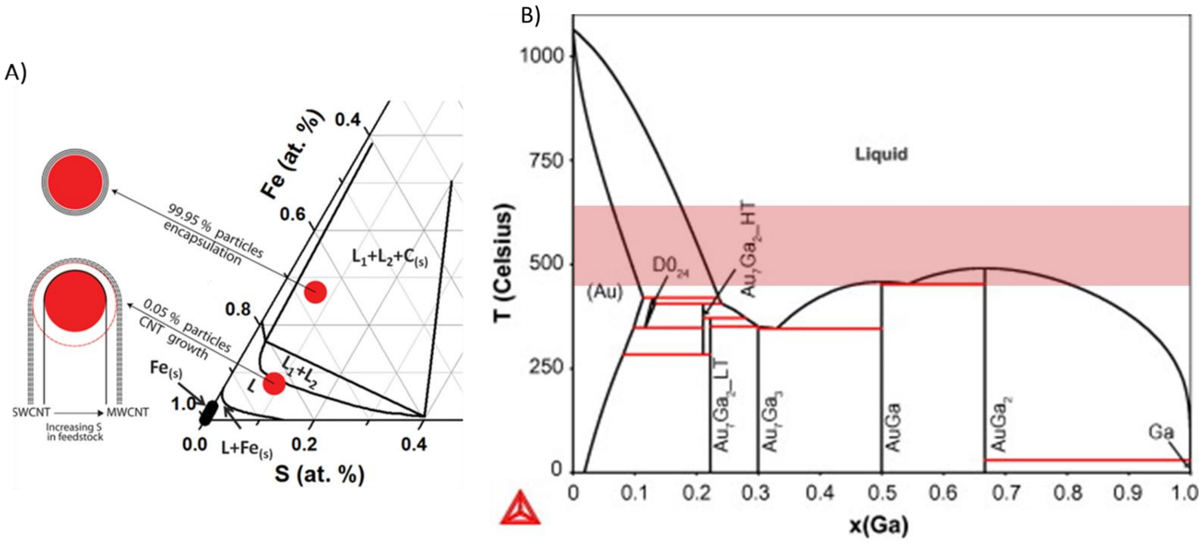

Figure 1.13 Thermodynamic tools A) Fe-S-C ternary phase diagram from [70] B) Ga-Au phase diagram presenting full solubility of Ga at synthesis conditions, from[71]

During nanowire growth, uncontrolled interactions between the precursor and the catalyst can lead to the formation of undesired structures, such as core-shell particles or catalyst enlargement.[72,73] This phenomenon often occurs when the precursor material exhibits high solubility in the catalyst at the synthesis temperature.

High precursor solubility, such as Ga (Figure 1.13 B), can lead to excessive incorporation of the precursor material into the catalyst particle. This can trigger uncontrolled growth of the catalyst alloy, exceeding its optimal size for promoting nanowire growth. However, this enlargement can occur without reaching a state of supersaturation. Instead, the enlarged catalyst particle may lose its ideal surface area to volume ratio, hindering its catalytic activity and limiting its ability to efficiently capture precursor material for nanowire growth.[74]

In addition, when the highly soluble precursor material has a low surface energy, it may preferentially occupy the outer surface of the catalyst particle rather than dissolve into it.[75] This can lead to the formation of a core-shell structure, where the catalyst forms the core and the precursor material forms a shell that hinders the catalytic activity of the core.

In the case of binary nanowires with one element being responsible for layer formation (poor solubility), to allow the nanowire growth, this element should be added to the reaction after the liquid alloy is formed and should be controlled during the reaction because a large amount of the insoluble component, can result in the total coverage of the catalyst, e.g. solid oxide, impeding further flake movement and precipitation.[45]

2. Materials and methods

The objective of this research is to delve deeper into the mechanisms involved in the growth of nanowires by FCCVD, especially those involving more than one element. The results presented in the following sections are organised in three chronological stages:

In the first stage, the focus was on SiC nanowires. Our research group has extensive experience in the synthesis and optimisation of carbon nanotubes (CNTs) and silicon (Si) nanowires, utilising floating catalyst. By studying SiC nanowires, we aim to gain valuable insights into the interactions between carbon and silicon species with the catalyst and develop a versatile experimental platform that can be adapted for the growth of metal oxide nanowires.

As a second stage, the insights gained from SiC nanowire research were applied to the design and construction of a new FCCVD reactor, with particular emphasis on precursor injection stability and process control. To accelerate the synthesis of new nanowires, a new sampling method for high-throughput screening was designed, including online monitoring and in-situ measurements.

The third and final stage involved the synthesis and growth of SnO nanowires in the newly developed FCCVD reactor. The reaction selectivity was studied through improved measurements of catalyst evolution and precursor decomposition. The experimental setup enabled the isolation of distinct growth stages, thereby providing a deeper understanding of the underlying mechanisms.

This section provides methodological information that applies to all stages. Specific details are provided where necessary.

2.1. FCCVD Reactor

A FCCVD reactor consists mainly of 1) a tubular furnace with continuous flow from the feed to the vent. 2) A feeding system to introduce the precursor, catalyst and carrier gas 3) A sampling system to gather information on the reaction products and their evolution.

One crucial aspect to consider in floating catalyst CVD reactors is their inherently dynamic nature given by the steep gradient of temperature along the flow path; it can create unwanted turbulence and buoyancy, impacting the evolution of the catalyst and precursor; that's why the flow should be kept laminar.

During the first stage of the thesis, for the synthesis of SiC nanowires, a vertical flow reactor was used, avoiding the thermal asymmetry of horizontal furnaces[14]. It consisted of a 3-zone resistive heating furnace with a ceramic tube (mullite 660, Øint = 7 cm) operating at atmospheric pressure. Figure 2.1 shows a schematic representation of the experimental set-up and collection systems.

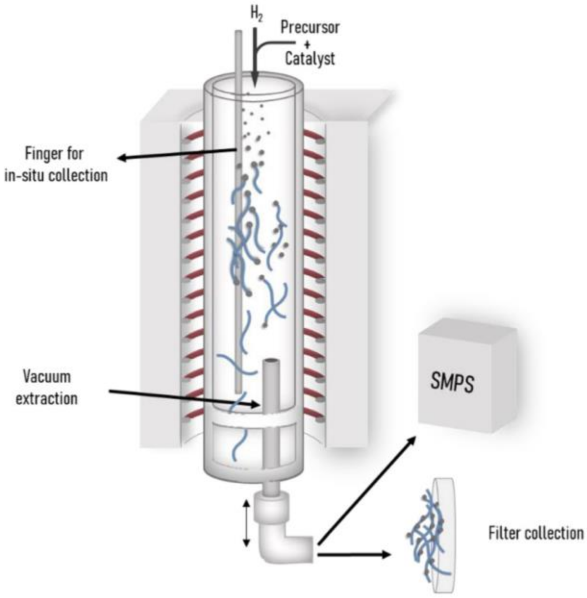

Figure 2.1 Schematic of the reactor for the synthesis of SiCNWs through floating catalyst CVD. It includes a ceramic finger for the in-situ collection of nanomaterials and a system for vacuum extraction of floating nanowires or catalyst aerosol nanoparticles.

As neither SiC nor SnO_x nanowires had been previously synthesised via FCCVD, the range of conditions was selected taking into account previous work on synthesis via SCVD and the conditions used in other FCCVD processes (Table 1.2): The temperature should be higher than that of the eutectic point of the target(s) material-catalyst phase diagram, the precursor concentration should be low to avoid homogenous nucleation (soot) and specifically for SiC, a

H_2 atmosphere could be beneficial as it is in the synthesis of CNTs and Si nanowires. All experiments conditions and solid products obtained are available in a data table (Annex 2 for SiC and Annex 3 for SnO)

The conditions selected as optimal in the synthesis of SiC nanowires in terms of observed conversion were found in the limits of the system used, making it difficult to explore further. The reactor system used for results described in Section 5 (SnO nanowires) was built to improve these limitations and add new features; all details are described in Section 4.

2.2. Precursor Selection and Injection

For experiments in Section 3, hexamethyldisilane (HMDS, $Si_2C_6H_{18}$) was selected as the SiC precursor because it is only composed of Si atoms and methyl groups (Me_6Si_2), minimising contamination from other species. Also, it is liquid at room temperature and has low viscosity, facilitating its injection. Literature about the thermal decomposition of HMDS suggests that it decomposes at a high temperature (950 °C) but is lower than the reaction temperature used in the experiments (1300 °C). Cai *et al.* [76] already used this precursor to grow SiC NW with no metal catalyst in a one-step batch process.

The precursor was fed through an injector placed at the upper part of the reactor. The injector consists of a syringe pump that feeds a capillary tube (1/16” OD and 0.010” ID) with a surrounding flow to aid the atomisation of the liquid. The high-velocity gas stream shears the liquid at the nozzle exit, breaking it into droplets. The size and distribution of the droplets depend on factors like the liquid flow rate, gas flow rate, nozzle geometry, and the properties of the liquid itself (viscosity, surface tension).[30]

The home-built atomiser presents stability problems if not optimised. Mainly, the catalyst precursor crystals may block the end of the capillary if the precursor is vaporised before its injection into the reactor vessel. If the carrier flow rate is not regulated according to the pumping rate of the liquid, it can either form pulses instead of a steady injection or, conversely, let a complete droplet pass through the reactor.

A good equilibrium between a steady injection and a correct temperature injection was found by positioning the injector end at 13 cm below the top flange, corresponding to a temperature of 485 °C).

In the case of SnO nanowire growth discussed in Section 5, the selected precursor was Tin (II) 2-ethylhexanoate ($C_{16}H_{30}O_4Sn$, $Sn(oct)_2$), a widely available commercial liquid, often used in polymerisation reaction. It is fed via an improved injector system described in Section 4.2; because of its high viscosity at room temperature, the liquid was kept at 50°C to favour its atomisation.

2.3. Catalyst generation

Catalyst selection is a crucial step before the synthesis, as on it depends the feasibility of nanowire growth. Iron was selected as SiC nanowires seed because it has shown excellent catalytic performance in the growth of CNTs, allowing high growth rates, and it has also been used for the growth of silicon nanowires.[77,78] The eutectic point of Fe-Si alloy is 1207 °C, relatively close to the eutectic point of Fe-C alloy (1147 °C). Thus, for SiC nanowires synthesis, a minimum temperature of 1200°C is likely to allow the insertion of both C and Si in the Fe droplet.

For the experiments detailed in this thesis, the catalyst aerosol was generated using three established methods: Spark discharge, Joule heating or in-situ formation.

For experiments in Section 3, SiC nanowires were synthesised using Fe as the catalyst. The Fe seeds were formed predominantly by in-situ formation from the decomposition of Ferrocene $Fe(C_5H_5)_2$. As a standard case, ferrocene was dissolved in liquid hexamethyldisilane (HMDS, C and Si precursor) until saturation (≈16 mg/ml) and then injected into the reactor by vaporisation aided by a carrier gas (H_2). Alternatively, Fe nanoparticles were formed with a high-voltage spark generator (SG) using iron electrodes (98.5 % purity) and carried to the reactor with an H_2 flow.

The SDG system was designed and built by Miguel Vazquez-Pufleau. The standard circuit (Figure 2.2) consists of a resistor (3.3 kΩ), a capacitor (32 nF), an inductor (1 µH) system and an electrode gap of 5 mm. The high-voltage source or power supply charges the capacitor, which then releases the energy as a spark. The resistance was added to protect the power supply from reverse discharge current.[79]

The average particle concentration generated by the decomposition of ferrocene was calculated to be 4.2 x 108 particles/cm3, considering the size distribution of the nanowires produced, as it is expected to coincide with the catalyst diameter distribution and the amount of ferrocene dissolved in the precursor. The concentration with SDG, measured directly from the reaction zone, is about one order of magnitude lower, of about 1.5×10^7 particles/cm^3.

For experiments in Section 5, Joule Heating, which relies on a direct current (180 A) passed through a resistive element, was preferred to generate the Au aerosol. The resistive element was a boat made of tungsten due to its high melting point. However, due to undesirable interaction (alloying) between Au and W, a thin plate (1.5 mm) of graphite was placed between the gold source and the boat.

Due to the high current passing through the circuit, contacts with the resistive boat need to be excellent; otherwise, extreme heating in a small area produces evaporation of the boat material, poisoning the catalyst production.

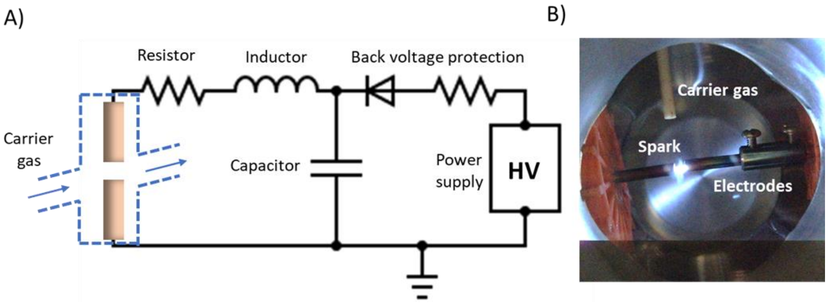

Figure 2.2 External catalyst generator systems A) Spark Discharge Generator (SDG) equivalent circuit and digital picture (B) of a spark

2.4. Sampling method

Two main systems were used to collect solid products from the gas phase. The first one consists of a thin mullite rod (6 mm diameter) inserted through the whole length of the reactor and kept there during the reaction. It has no form of cooling and can thus be assumed to have the same temperature profile as the reactor tube.

The second consists of a vacuum extraction system with a polyethersulfone (PES) filter to collect the solid products of the reaction. In the case of SiC synthesis experiments performed in an open-end reactor, a controllable position probe was used to suck material from different parts of the reactor chamber. The system consisted in a 1-m-long ceramic tube (1/4" diameter) extracting 0.5 lpm of the gas inside the reactor by means of a Venturi pump-critical orifice[80] and filtered at the end. The reaction gas could also be directed to a scanning mobility particle sizer (SMPS) for size distribution characterisation.

The ceramic rod and vacuum filter provide separate means to sample and then analyse the morphology and composition of solid products, the premise is that the material collected at different positions along the reactor tube reflects the progression of the reaction through it.

However, these collection systems are probably size selective: Nanowires, particularly those of high aspect ratio can aggregate, entangle in the gas phase and attach to the surface of the ceramic rod and/or the reactor tube walls. Soot particles are less prone to aggregation and more likely to be collected by the vacuum system. Save for recent work on the formation of carbon nanotube aerogels,[56,81] the dynamics of high aspect ratio nanoparticles floating in a gas stream is a largely unresolved problem.

In the new reactor design described in Section 4, the same features were conserved, while fixed sampling ports were added at the end of the reactor to improve reliability in the collection and reproducibility between experiments.

2.5. Characterisation Methods

After extraction, samples were characterised by optical imaging and scanning electron microscopy (SEM, FEI Helios NanoLab 600i). Micrographs were used to obtain the diameter and length distribution by image analysis. The distributions of diameter and length in Figure Figure 3.9 were obtained from inspection of 500 and 170 NWs, respectively. Raman spectroscopy (Raman Spectrometer RENISHAW MoD. Invia) was carried out with a laser wavelength of 532 nm (2.33 eV), using 50x objectives. High-resolution transmission electron microscopy (HRTEM, FEI Talos F200X) and wide-angle x-ray scattering (ALBA synchrotron, NCD-SWEET beamline and in-home SAXSpoint 5.0 SYSTEM) were performed to assess the crystallinity and phase composition of the nanowires.

The catalyst and solid products were analysed on-line with a scanning mobility particle sizer (SMPS, GRIMM model 5705) which selects particle size based on a differential mobility analyser (DMA, GRIMM model 5706) to obtain data of the concentration and size distribution.

A DMA works with two concentric cylindrical electrodes with a small gap between them. A high voltage is applied between these electrodes, creating a strong electric field. As the aerosol flows through the gap, the previously charged particles experience a force resulting from the combination of the electrical force and the drag force from the carrier gas. Only particles with a specific electrical mobility will travel through the centre of the gap and exit the DMA to be counted, in this case by a Faraday cup electrometer (model 5705). By varying the voltage applied to the DMA electrodes, the SMPS can effectively scan a range of electrical mobilities.

2.5.1. Length measurement

Determining the length of high aspect ratio nanomaterials is established as a long-standing challenge. Despite extensive research on CNTs produced by FCCVD, the only reported estimates of length are a calculation based on the number of ends found in a sample,[69] and indirect measurements using polarised IR spectroscopy.[82] Due to the exceptionally high aspect ratio of the SiCNWs in this study, TEM is not suitable for direct length measurements because it would require a highly dispersed state for the material, preferably individual nanowires. This translates to complete dispersion in solvents followed by deposition on TEM grids, a process that often results in unintentional shortening of the nanowires. Previous work on CNTs, SiNWs and now SiCNWs has proven this method unsuccessful.

Instead, taking advantage of the SiC and SnO nanowires' relatively large diameter, we image them directly using high-resolution SEM. However, in their pristine state, the nanowires exhibit a highly entangled structure, necessitating extensive observation to identify individual wires with their complete length exposed.

To determine the mean length, we employed samples collected directly from the reactor. The samples, consisting of nanowire webs, were subsequently introduced to isopropanol and subjected to mild sonication for three minutes. The sonication process aimed to disperse individual nanowires but mostly only relax the entangled network structure. However, the effectiveness of this procedure varied depending on the initial degree of entanglement within the web.

After sonication, a droplet of the resulting suspension was deposited on top of a flat substrate, typically a Si Wafer to favour conductivity. To construct a comprehensive map of the nanowire network, multiple high-resolution SEM images were captured and subsequently stitched together. Figure 2.3 exemplifies this process for SiCNWs. The resulting image was then meticulously examined to identify individual nanowires with their entire length clearly visible. These nanowires were typically located on top of the network or near its edges, where entanglement was less pronounced. Finally, the lengths of these identified nanowires were measured using ImageJ software.

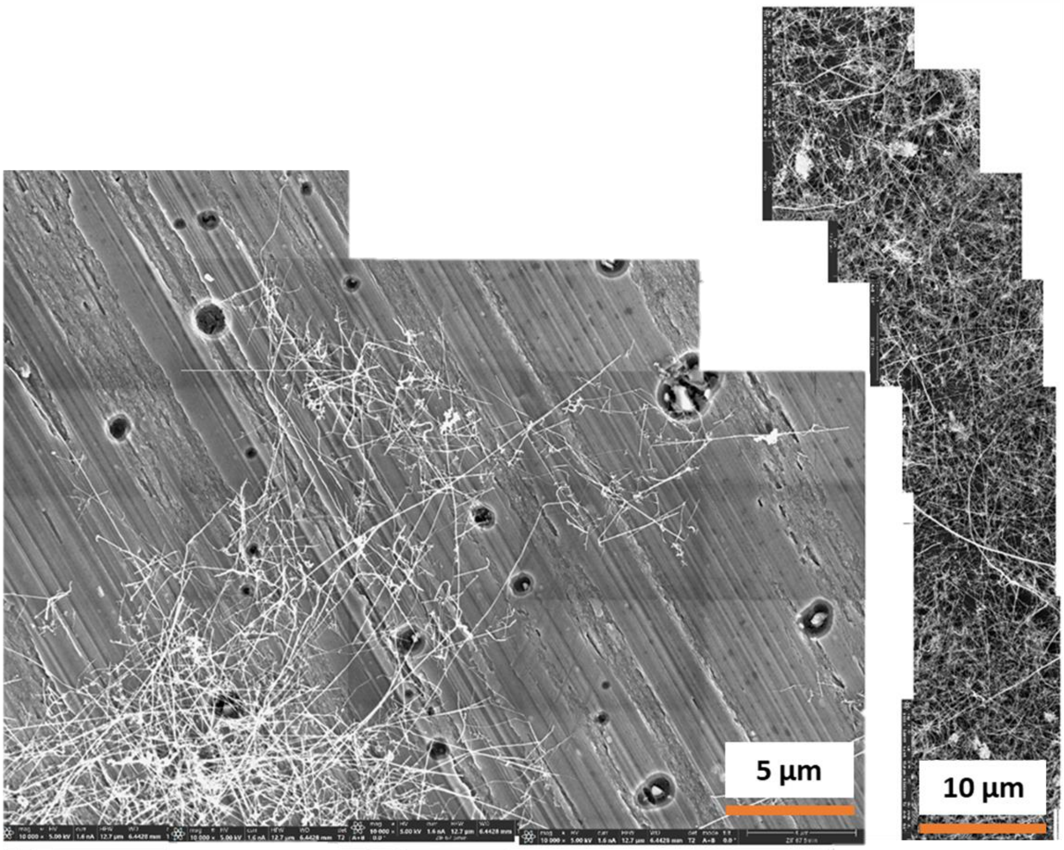

Figure 2.3 Examples of SEM micrograph map of a sonicated sample to recreate and measure a single nanowire length.

3. SiC Nanowire growth and self-assembly by FCCVD

This study represents the first successful synthesis of SiC nanowires by FCCVD, achieved using a vertical flow-through reactor without the need for external substrates and via the vapour-liquid-solid (VLS) mechanism. An iron (Fe) aerosol was used as the catalyst, while hexamethyldisilane (HMDS) acted as the silicon and carbon precursor.

The equipment details and experimental procedures are provided in Section 2: Materials and Methods. After exploration of various growth parameters, the following conditions were identified as optimal in terms of reaction selectivity for SiCNWs: the liquid HMDS was fed through an injector placed at the upper part of the reactor at a rate of 0.5 ml/h, previously ferrocene was dissolved in liquid HMDS until saturation (≈16 mg/ml). The temperature was set to a nominal temperature of 1300 °C, and an H_2 atmosphere was sustained by a 3 lpm H_2 flow.

Under these optimised conditions, samples containing webs of SiCNWs were directly collected from the reactor's growth zone using a ceramic rod positioned inside for the entire reaction duration. Figure 3.1 presents digital images of two such samples and an electronic micrograph showing the ultralong nanowires.

This chapter first describes the experimental efforts to identify conditions of high selectivity through adjustment of aerosol and precursor decomposition dynamics. A well-defined growth zone was established within the reactor, where SiC nanowires were directly collected. The gas-phase growth of SiC nanowires was confirmed, followed by an exploration of the parameter space (around 60 different experiments), resulting in increased selectivity towards nanowires. The nanowire growth, along with the undesired product formation, is rationalised through the precursor decomposition path and the thermodynamics of the Fe-Si-C ternary diagram. The network material was subsequently characterised in terms of its building block morphology and spatial organisation. Finally, the crystallinity and polytypism of the nanowires were assessed.

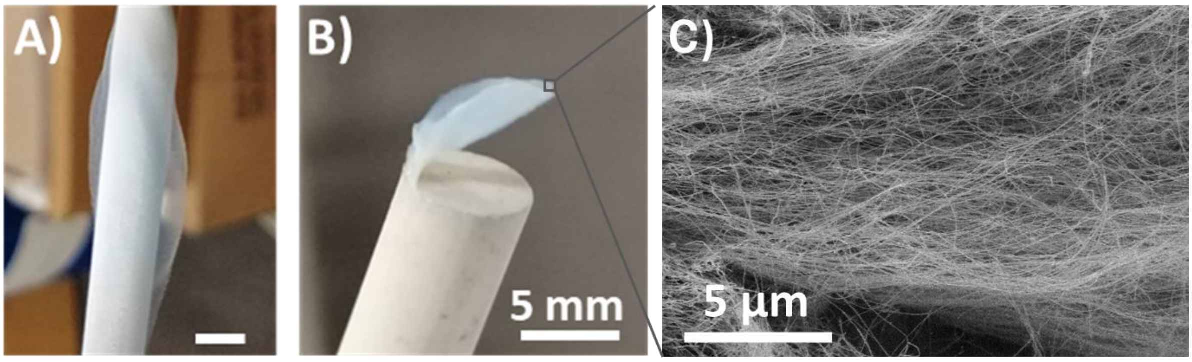

Figure 3.1 SiCNW materials produced by FCCVD and collected as solids. Left: SiC NWs aerogel attached to the rod lateral surface, collected for 2 hours. Right: free-standing SiC nanowires flake, collected on the top surface for 45 minutes. **C)** SEM micrograph showing the network structure of high-aspect ratio SiCNWs. Adapted from [83]

3.1. Defining the gas-phase growth of SiC nanowires

As previously discussed, the flow-through reactor is characterised by two main features. Firstly, both the catalyst and SiC precursor evolve as they travel through the hot tubular furnace. Second, the residence time within the reactor is very short, lasting less than 60 seconds. Consequently, the great variety of local conditions can lead to the production of not only SiC nanowires, but other reactions can also occur, and other products can be formed.

In a first approach collecting samples only downstream at the end of the reactor, spare NWs were found intermixed with undesired products; although it was possible to detect changes in the byproducts related to the experimental conditions (i.e. colour, nanoparticle size), it was hard to follow the effects on the SiC nanowires. Hence, the sampling system described in Section 2 was designed to gather insights into the nanowires growth mechanism by directly collecting solid reaction products from the reaction zone.

A ceramic rod inserted into the reaction zone facilitated the direct collection of solid products, which allowed us to correlate them with their reaction temperature. The relationship between the collected solids and the temperature profile is depicted in Figure 3.2. This analysis indicates that the growth of SiCNWs occurs only in a small region of ≈3 cm in the hot zone, where the temperature reaches 1120 - 1140 °C. The SiCNWs grown at this position form a clear bluish aerogel around the ceramic rod (Figure 3.1 A).

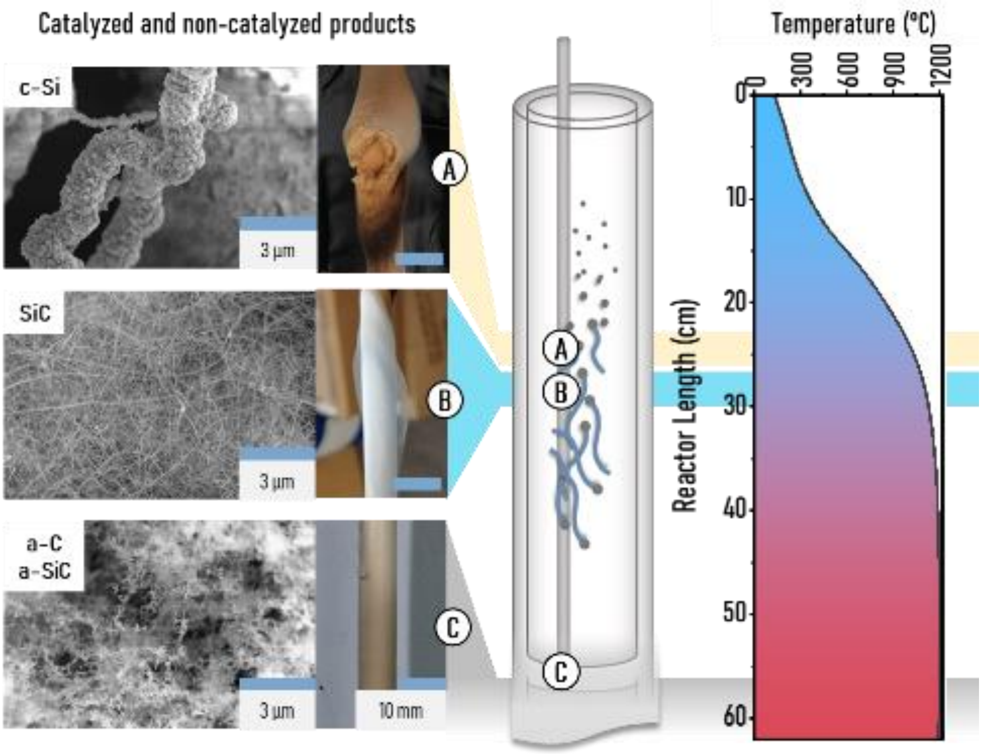

Figure 3.2 Reactions in the synthesis of SiCNW by FCCVD. Collected materials synthesised through the flow reactor and the corresponding temperature profile. Adapted from [83]

Silicon, Carbon and SiC particles were also found on the surface of the collecting rod; their formation and composition are further discussed in the next section as they give valuable information on the precursor decomposition throughout the reactor.

A direct outcome of these experiments is a well-defined growth rate. As nanowire growth is only observed over a region of 3 cm, the corresponding residence time is ≈2.3 s. Considering the nanowire length distribution, the average growth rate comes out as 8.5 µm/s and as high as 50 µm/s. For reference, this is more than three orders of magnitude faster than conventional substrate growth of SiC (Figure 3.3). It is also far above the highest rates observed using growth enhancing agents such as rare earths (1 nm/s)[84] and Ga (185 nm/s)[85].

These results are in line with previous studies on the growth of SiNW[9] and GaAsNW[19] and confirm that nanowire growth by FCCVD is inherently orders of magnitude faster than in substrate-based CVD. This is attributed to faster precursor transport because, in FCCVD growth, the catalyst is surrounded by excess of gas precursors, increasing the availability for precursor incorporation due to a higher collision rate between the catalyst and intermediate active species.

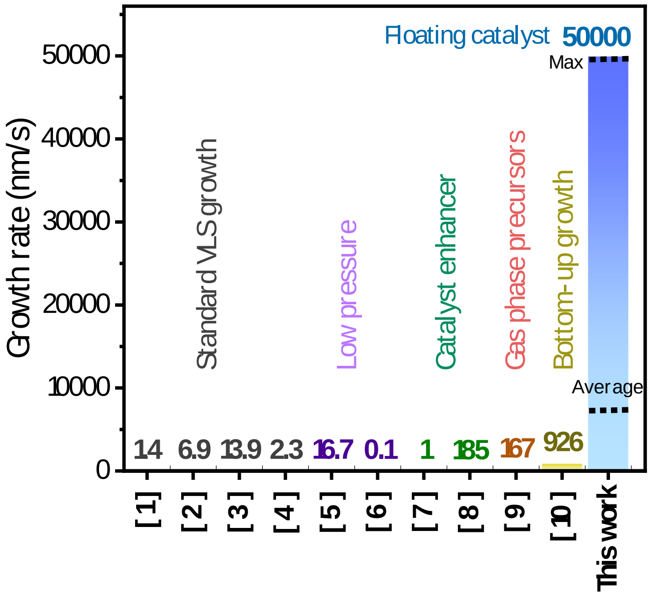

Figure 3.3 Comparison of SiCNW growth rates obtained experimentally. Values were calculated by dividing the average length of the nanowires by the experimental growth time. [1] Meng et al.[86] [2] Park et al.[87] [3] Panda et al.[88] [4] Wu et al.[89] [5] Zhang et al.[90] [6] Zhou et al.[91] [7] Rajesh et al.[84] [8] Kim et al.[85] [9] Attolini et al.[92] [10] Li et al.[93] Adapted from [83].

A set of control experiments were conducted to confirm that the sampled NWs grow through floating catalyst rather than on the ceramic sampling rod. First, the movable vacuum system was used to extract material at different heights inside the vertical reactor. Sparse SiCNWs were found covered in soot particles but only when the extraction probe was below the hottest zone of the reactor (Figure 3.4). Confirming their growth in the gas phase without any additional surface and the need for high temperatures for their formation.

In additional experiments, samples were collected using the ceramic rod inserted in the reaction zone for different lengths of time. All experiments showed almost identical length distributions for different dwell times (Figure 3.5) even for times as short as 10 s. These findings confirm that significant nanowire growth occurs within a short timeframe, suggesting that the growth of the nanowires once attached to a surface is negligible.

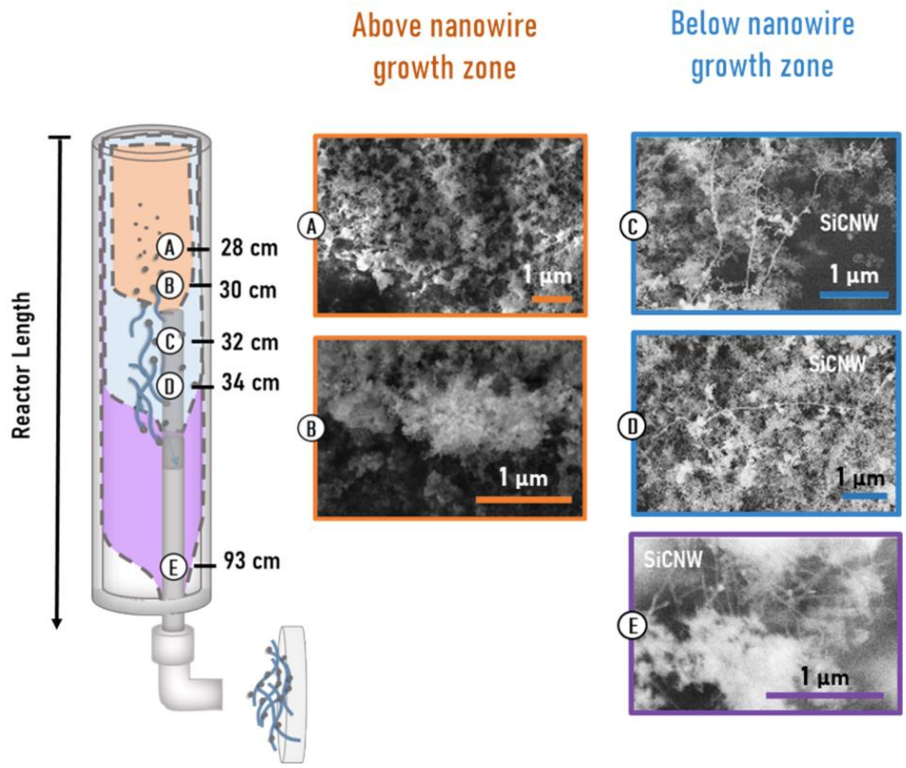

Figure 3.4 Samples extracted with vacuum collection system at different positions of the reactor, using catalyst produced by ferrocene decomposition. A-B) Samples taken above the nanowire formation zone do not present nanowires, only nanoparticles produced from pyrolysis. C-E) Samples collected in the growth zone or below present nanowires along with other by-products. Adapted from [83].

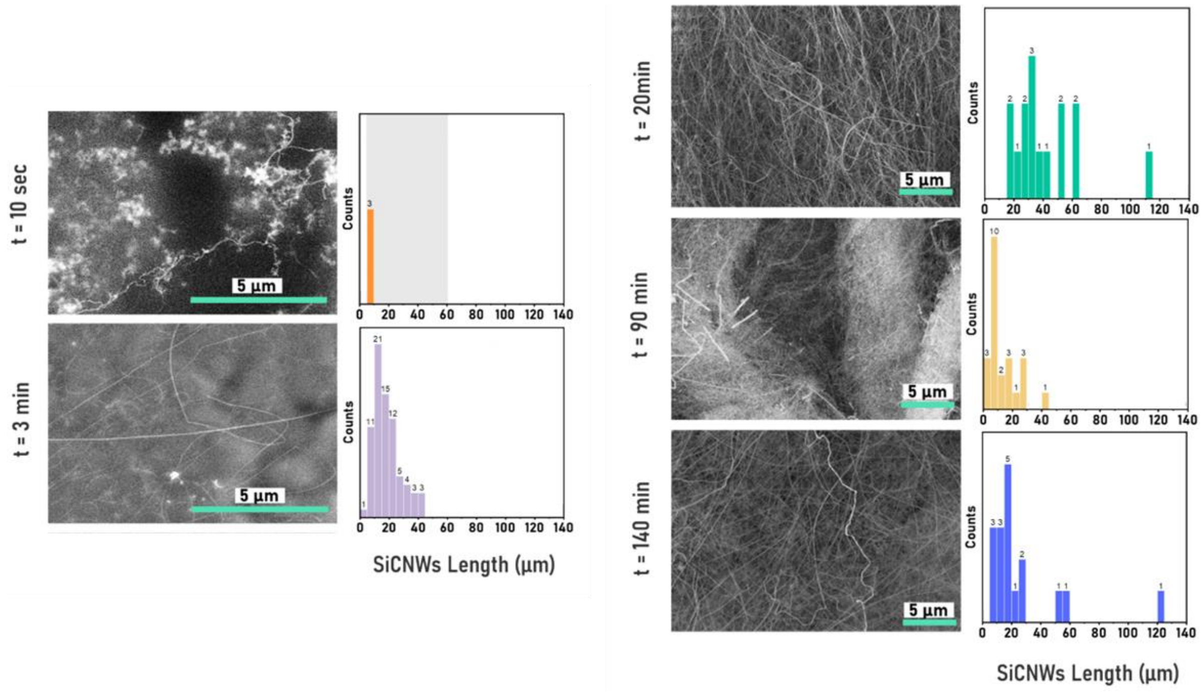

Figure 3.5 Length of NW collected by the ceramic rod at different experiment times. Standard synthesis conditions were used in all experiments shown. Adapted from [83].

3.2. Selectivity in FCCVD synthesis of SiC nanowires

In addition to SiCNWs, the sampling probes used show other nanostructured solid products of the reaction, as advanced in Figure 3.2. However, the Fe catalyst does not mediate their growth, and no traces of Fe were found in these solid products.

Microscopic aggregates of Si were found firmly attached to the ceramic rod in a region corresponding to a temperature of approximately 1050°C. They were highly crystalline and were only detected in the presence of the sampling probe. Previous studies[63] in CNTs synthesis found that the ceramic reactor tube has a crucial role in the decomposition of carbon precursors, with mullite demonstrating a more pronounced effect compared to alumina. Thus, the Si aggregates likely form through precursor decomposition and solid nucleation on the rough mullite surface.

Other soot particles are produced without mediation of the catalyst. They are found with both sampling probes, implying that they form through pyrolysis in the gas phase. These soot particles are mainly amorphous carbon and amorphous silicon carbide aggregates.

Figure 3.6 shows the Raman and HRTEM characterisation of the reaction products. The composition of the solid products is the same for the range of synthesis conditions studied in the search for high selectivity towards nanowires (Ferrocene or SG as catalyst source, 1300 °C or 1250 °C, and carrier gas with 10% nitrogen), although their concentrations relative to that of the SiCNWs varies across these synthesis conditions.

Aerogel formation around the ceramic rod was exclusively observed when using 100% hydrogen as the carrier gas. As the N_2/H_2 ratio in the synthesis gas mixture increased, the concentration of soot nanoparticles also rose, hindering nanowire growth. Similarly, higher precursor concentrations led to the rapid formation of nanoparticles.

The role of hydrogen in the growth of SiC nanowires is similar to that observed in FCCVD growth of CNTs[70] and SiNWs[9,64]. In both cases, hydrogen plays a crucial role in controlling selectivity towards 1D nanoparticles by suppressing the formation of carbon soot and amorphous silicon particles through the modulation of precursor decomposition kinetics. Further discussion on the conditions that lead to high selectivity across the synthesis of different materials via FCCVD is presented in Section 6. A first analysis of this phenomenon in the growth of SiC nanowires using HMDS is presented here.

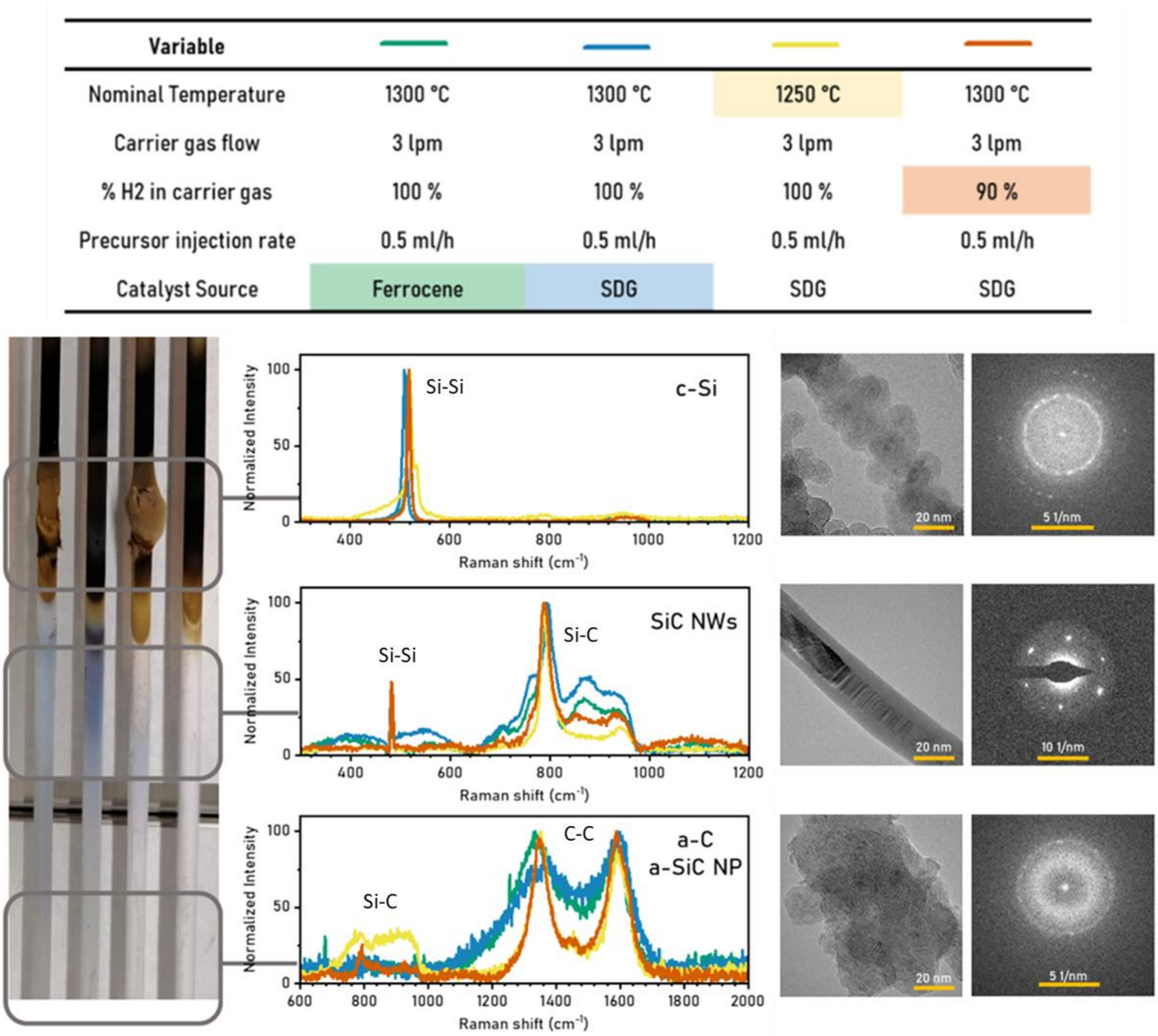

Variable	🟩	🟦	🟨	🟧
Nominal Temperature	1300 °C	1300 °C	1250 °C	1300 °C
Carrier gas flow	3 lpm	3 lpm	3 lpm	3 lpm
% H2 in carrier gas	100 %	100 %	100 %	90 %
Precursor injection rate	0.5 ml/h	0.5 ml/h	0.5 ml/h	0.5 ml/h
Catalyst Source	Ferrocene	SDG	SDG	SDG

Figure 3.6 Raman spectra and HRTEM micrographs of the different solids produced collected on a ceramic rod inserted in the reactor tube. Adapted from [83].

Reports on the pyrolytic decomposition of HDMS propose complex decomposition routes, with a large number of decomposition products and intermediates and multiple pathways.[94,95,96] Nevertheless, there is consensus about some initial routes for the decomposition of HMDS involving the production of methyl and silylene radicals and H_2:

$$Me_3Si - SiMe_3 \rightarrow 2Me_3Si^* \qquad \text{Equation 1}$$

$$Me_3Si^* \rightarrow Me_2Si + Me^* \qquad \text{Equation 2}$$

$$Me_2Si \rightarrow C_2H_4 + SiH_2 \qquad \text{Equation 3}$$

$$Me_2Si \rightarrow C_2H_2 + SiH_2 + H_2 \qquad \text{Equation 4}$$

The methyl and silylene radicals are precursors in Si and C nanoparticle formation (the competitive route to nanowire formation). The simplified reaction mechanism proposes that methyl and silylene radicals polymerise by insertion in their parent precursor until forming nanoparticles:

$$Me \ + C_xH_y \rightarrow C_{Nanoparticle} \qquad \text{Equation 5}$$

$$SiH_2 + Si_pH_q \rightarrow Si_{Nanoparticle} \qquad \text{Equation 6}$$

However, the methyl and silylene radicals can also react with hydrogen, getting neutralised as exemplified here:

$$Me + \frac{1}{2}H_2 \rightarrow CH_4 \qquad \text{Equation 7}$$

$$SiH_2 + H_2 \rightarrow SiH_4 \qquad \text{Equation 8}$$

Considering the reaction paths (Equation 7 and 8) a hydrogen atmosphere is, by Le Chatelier's principle, expected to reduce the effective decomposition rate of silylene and methyl radicals precursors, preventing the non-catalysed formation of Si, C and SiC nanoparticles. This allows the precursors to have a larger lifespan enhancing their chance of impinging into Fe catalysts to form SiC nanowires.

In summary, considering the decomposition of HMDS, selective growth of SiCNW requires the inhibition of soot nanoparticle formation, which is a side reaction that depletes the reagents for NW formation. This is achieved by utilising a hydrogen atmosphere, which reduces the reaction rate of the side reaction and allows catalysed growth before the onset of nanoparticle nucleation.

It is also important to consider that in the thermal decomposition of HDMS, all initial products, intermediates, and most secondary products are C-containing silanes and silylenes. This suggests that the species impinging on the catalyst could contain both Si and C.

Considering nanowire growth as a solidification process from the catalyst, we can qualitatively describe the nucleation of SiCNWs based on the thermodynamics of the Si-C-Fe system. The Fe-Si-C ternary phase diagram provides insights into the thermodynamically stable products obtainable from specific precursor species concentrations. For example, it reveals the favoured formation of SiCNWs as the only catalysed product, distinguishing them from CNTs or SiNWs that might otherwise form under similar conditions. Additionally, the phase diagram offers information regarding the minimum temperature required for nanowire growth.

The Fe-Si-C equilibrium ternary phase diagram at 1200 °C (Figure 3.7 B) and isopleth Fe-SiC section (Figure 3.7 A) were calculated by Jorge Valilla using CalPhaD methodology. These calculations show the equilibrium phases for a bulk system, neglecting interfacial energy contributions that are not usually negligible in nanosized systems. When accounted for, these contributions tend to shift the phase diagram toward lower temperatures.[97,98,99]

A clear example of this effect is reflected in the theoretical minimal growth temperature, which resulted in ≈1170˚C, higher than the one measured experimentally in the 3-cm zone at 1130 ˚C. However, even if calculations remain qualitative, they allow the identification of expected phases and a rationalisation of the reaction pathway.

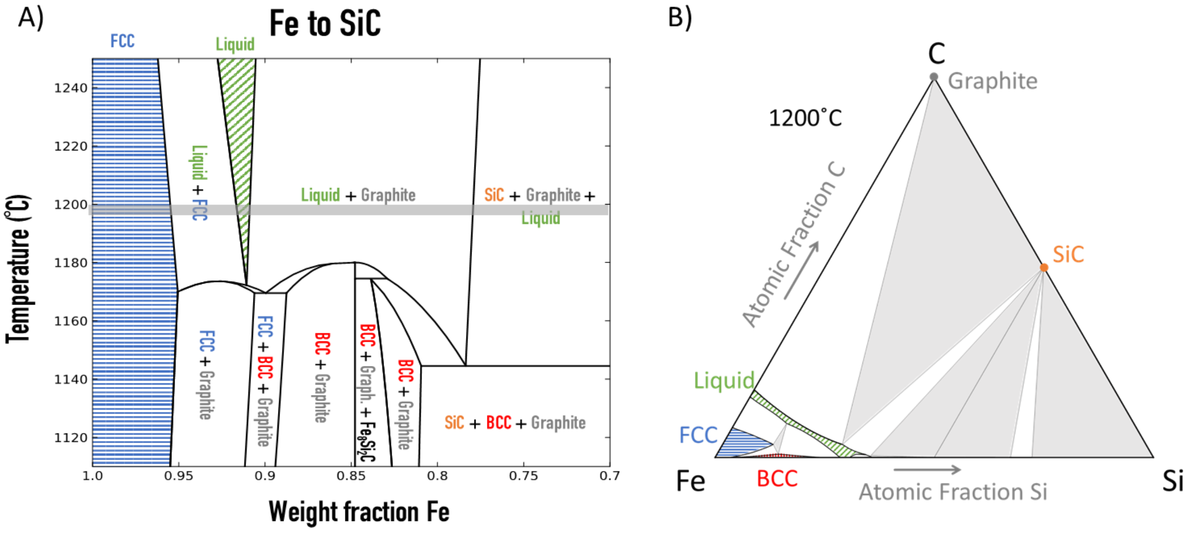

Figure 3.7 A) Isopleth section of the phase diagram through pure Fe and SiC. B) Ternary isothermal phase diagram at 1200˚C. Grey triangles show three-phase invariant equilibria; hatched regions show single-phase regions; for clarity, tie-lines are not shown (hence two-phase regions appear white). Adapted from [83].

Figure 3.8 A illustrates the compositional path starting from a Fe-rich particle (labelled a) with a constant influx of Si and C; the C:Si influx ratio is set to 1:3 as in HMDS. First, both Si and C enter in solution within the FCC Fe phase. When their limit of solubility (b) is reached, a liquid phase forms (c), which will also get enriched in C and Si until the limit of solubility within the liquid is reached (d). Then, the excess C in the liquid leads to the formation of graphite, and upon further addition of Si and C, the liquid composition follows the Liquid-Graphite solvus line until reaching the nucleation point of SiC compound (e).

The ternary diagram shows that SiC will form irrespectively of the initial compositions of the Si-C species impinging on the Fe catalyst since the liquid phase exhibits only equilibria with graphite and SiC phases along its Fe-lean solvus line. The initial ratio of Si to C in the liquid will simply shift the fraction of SiC to $C_{(solid)}$ in the final product. In addition, we note that this phase evolution appears to be the same for all temperatures above the eutectic, as shown in the Fe-SiC isopleth (Figure 3.7 A). This indicates that the thermodynamic product of a Fe catalyst nanoparticle supersaturated with C and Si, is a SiC nanowire.

Finally, the phase atomic fraction of the points (a) through (e) in the proposed reaction path are listed in Figure 3.8 B. Point (c) is calculated from the thermodynamic equilibrium of the liquid with the FCC phase at composition (b), while compositions (b) and (d) are calculated by addition of C and Si from points (a) and (c), respectively, with a C:Si ratio of 1:3 corresponding to HMDS.

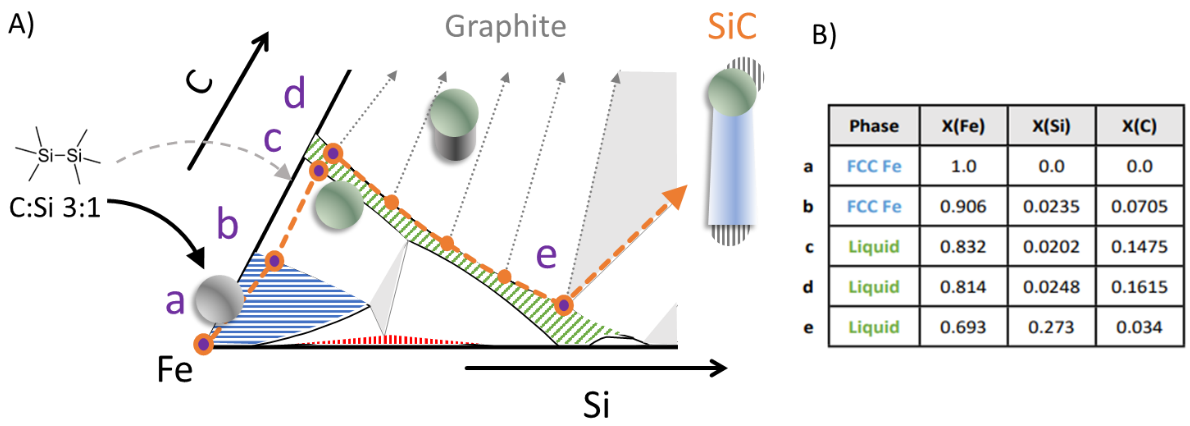

	Phase	X(Fe)	X(Si)	X(C)
a	FCC Fe	1.0	0.0	0.0
b	FCC Fe	0.906	0.0235	0.0705
c	Liquid	0.832	0.0202	0.1475
d	Liquid	0.814	0.0248	0.1615
e	Liquid	0.693	0.273	0.034

Figure 3.8 A) Compositional path from pure Fe (a) to SiC formation (e) following continuous addition of Si and C. B) Calculated atomic composition at each growth point. Adapted from [83].

3.3. SiC nanowires morphological characterisation

Figure 3.9 shows the results obtained from SEM image analysis of sparse networks. The diameter distribution exhibits a lognormal distribution, ranging from 2 to 100 nm, with a mean value of 25.4 nm and a geometric standard deviation (GSD) of 1.78. It was obtained from image analysis of 500 nanowires, including from different samples at same conditions. The diameter distribution's logarithmic nature reflects the catalyst's aerosol evolution. Metal particle aerosols inherently exhibit greater polydispersity (GSD > 1.36) compared to metal particles produced on a substrate (GSD < 1.34).[100] These findings corroborate the hypothesis that SiCNWs grow from freely suspended catalyst particles.

The measurement of length was performed as described in Section 2.5.1, the mean NW length was found to be around 20 µm with a maximum value of 123 µm. Interestingly, the length distribution also presents a lognormal trend.

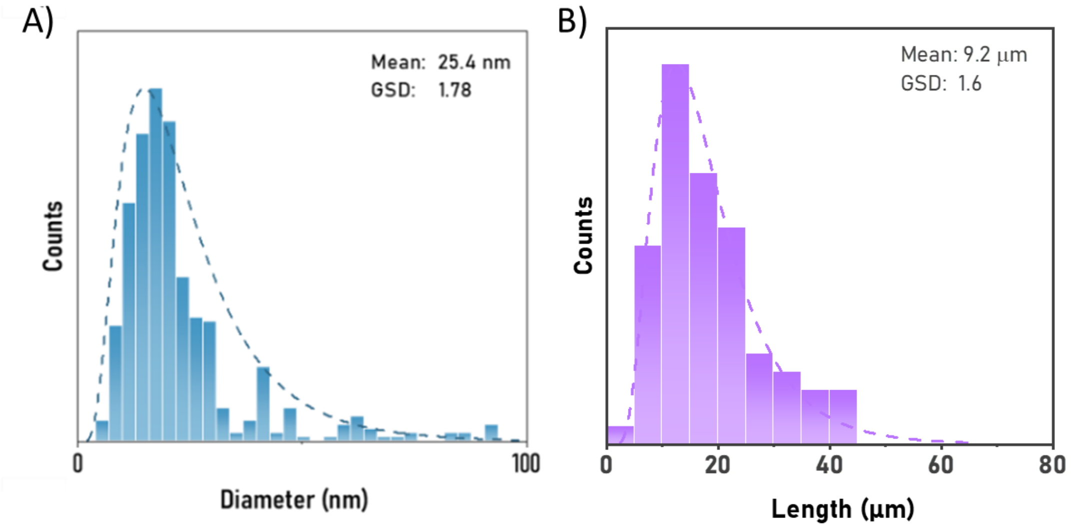

Figure 3.9 A) Diameter distribution measured by SEM image analysis of different samples synthesised at standard conditions. Adapted from [83]. B) Example of length distribution of one sample collected on the rod surface.

In experiments with SDG as the Fe catalyst source, the diameter distribution of the nanowires produced coincides almost perfectly with the catalyst size at the growth zone (measured with the movable sampling tube and directly scanned with the SMPS), as Figure 3.10 A shows. The generated catalyst and nanowires have an average of 10 nm, smaller than the one obtained with ferrocene decomposition. Figure 3.10 B shows a comparison in the diameter distribution of the nanowires using both catalyst sources.

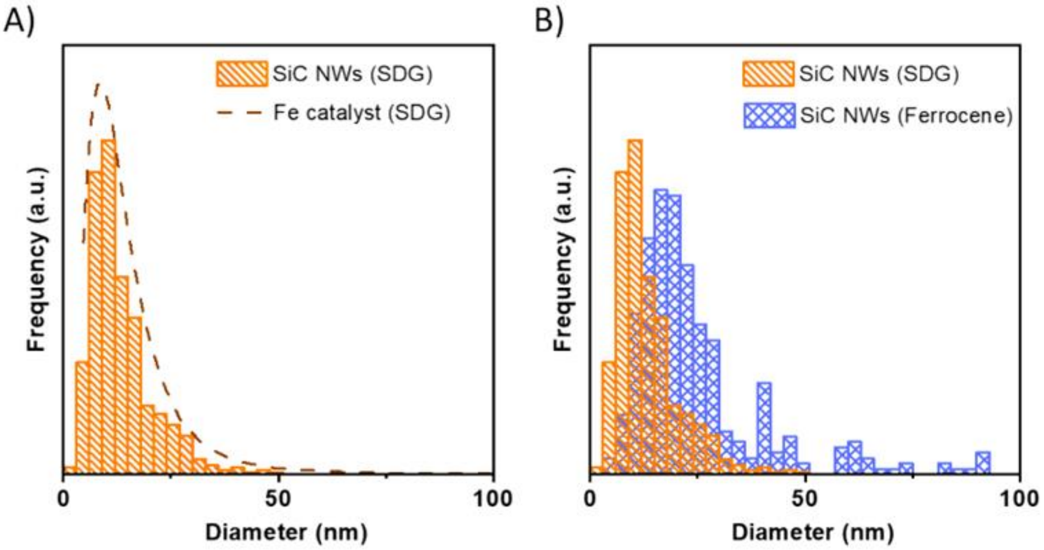

Figure 3.10 A) Comparison of the diameter distribution of the Fe catalyst produced with SDG (dashed line) and that of the nanowires grown with this catalyst source (histogram). B) Diameter distribution of NWs grown with SDG (orange) and Ferrocene (blue). C) Samples collected from experiments under the same conditions but from different catalyst sources, namely, ferrocene and SG. Adapted from [83].

Furthermore, regardless of the chosen Fe catalyst source (spark discharge generator (SDG) or ferrocene decomposition) and the difference in size and concentration they delivered, SiCNW growth is concentrated in the same 3-cm zone. This observation is noteworthy because it deviates from the phenomenon occurring with CNTs, where the growth is mediated by catalyst size, occurring where the catalyst is still nucleating. In this case, the 3-cm growth zone is independent of the catalyst evolution, while *in situ* formed catalyst particles typically require nucleation and growth to reach a size suitable for nanowire catalysis, the SDG particles maintain a size appropriate for SiCNW growth throughout their entire journey within the reaction tube, from entry to exit. Precursor availability and temperature, rather than catalyst size, are considered to have more impact on the growth of SiC nanowires, as the precursor starts its thermal decomposition around 950 °C.[94]

A self-standing sample of SiCNW was analysed with small angle x-ray scattering (SAXS) to explore the nanowires and their network structure. Although a definitive model for describing one-dimensional nanoparticle assemblies remains under debate, suitable approximations have been explored using SAXS and SANS spectra.[101] This is particularly interesting in this case, with the objective of obtaining descriptors of the nanowire population and their ensemble that can complement electron micrographs.

The network material presented strong features in the radial intensity profile. The intensity profile, shown in Figure 3.11 A, presents clear Bragg diffraction peaks at mid values of scattering vector (q), with a particularly intense one at a d-spacing of 19 nm. We attribute these features to the form factor of the SiCNWs and is similar to the average nanowire diameter. Their prominence over the Porod slope (q^{-4}) suggests smaller diameter polydispersity.

Meshot et al. [68] proposed a model to extract morphological information of ordered CNT networks from their SAXS scattering intensity profile (*I(q)*). *I(q)* is comprised of two primary components: the intraparticle form factor (*F(q)*), which relates to the particles size distribution, and the interparticle form factor (*S(q)*), derived from particle-particle scattering observed at lower q values.

$$I(q) = C\,F(q)\,S(q) \qquad \text{Equation 9}$$

For the purposes of this analysis, S(q) is assumed to be equal to 1, which is reasonable given the random orientation of SiC nanowires in the samples collected. Consequently, the factor scattering intensity profile would be represented by the cross-sectional scattering function of a solid cylinder:

$$I_c(q) = \frac{\int_0^\infty P(r)\ f^2(q,r)\ dr}{\int_0^\infty P(r)\ dr} \qquad \text{Equation 10}$$

Where P(R) is the probability distribution function of cylinder radii (r). From the experimental results presented before, the distribution has a lognormal line shape:

$$P(r) = \frac{1}{r\ \sigma\sqrt{2\,\pi}}\ \exp\left(\frac{-(ln(r)-\mu)^2}{2\,\sigma^2}\right) \qquad \text{Equation 11}$$

f (q,R) is the form factor of a long cylinder in a dilute system, where Δρ is the difference in scattering density distribution between the nanowires and the surrounding medium, and J_1 is the spherical Bessel function of the first kind

$$f(r,q) = \Delta\rho\ r\ \frac{2\ J_1(q\,r)}{qr} \qquad \text{Equation 12}$$

P(r) can be found simply by minimising the error in the calculated $I_c(q)$ with respect of the obtained experimentally, optimising the values of μ and σ in the lognormal distribution. The result is presented in Figure 3.11 B, along with the diameter distribution of the same free-standing network obtained by SEM and TEM analysis.

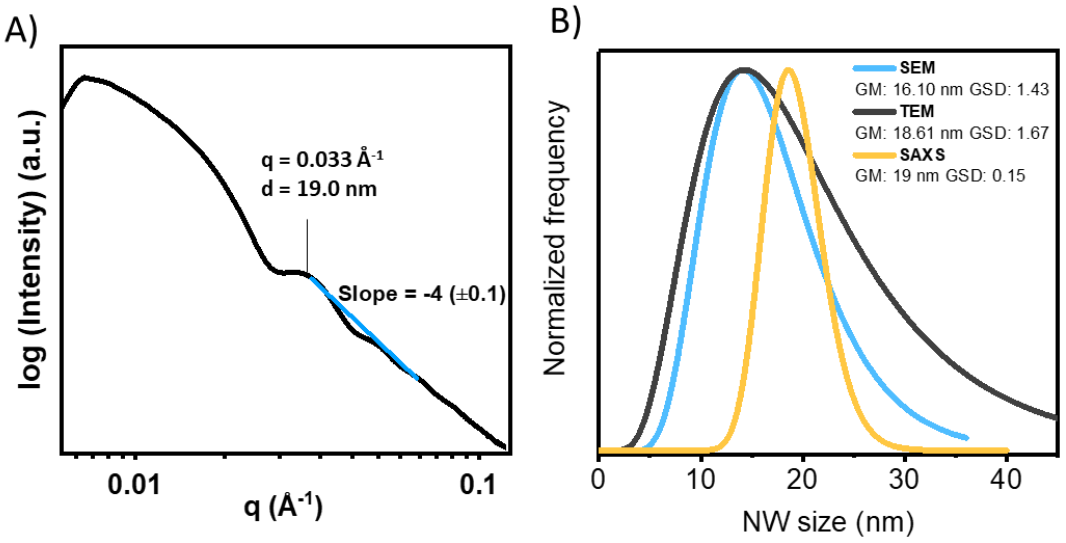

Figure 3.11 A) SAXS intensity profile showing low polydispersity in a single self-standing sample B) Diameter distribution of a sample collected at standard conditions measured with SEM, TEM and the pair distribution function (PDF) obtained from SAXS analysis.

While the diameter values obtained from the three size distribution techniques (SAXS, SEM, and TEM) were relatively consistent, the SAXS analysis revealed a narrower size distribution (GSD = 0.15) compared to the imaging techniques (GSD = 1.4-1.67). This discrepancy could be attributed to several factors, including a lack of uniformity in the network, sample preparation, and human bias during image processing, but most likely, oversimplification of the SAXS model used to extract diameter distribution from the radial profile.

To address potential network non-uniformity, the experimental procedure was carefully designed to ensure the sample's representativeness. As the SAXS patterns were acquired from a 130 µm x 130 µm region equivalent to the beam size, to match this broad region, SEM analysis was performed by analysing multiple images from different positions of the same sample. Similarly, for TEM analysis, random nanowires were selected by dispersing the sample and drop-casting it onto a TEM grid. High-contrast SEM micrographs were analysed with careful consideration of potential size distribution biases.

Apart from experimental issues, the model proposed by Meshot et al., used here to analyse the SAXS scattering pattern, assumes a dilute regime in a two-phase system. In this context, the two phases would be infinitely-long SiC and air. Contributions from soot and catalyst particles are therefore ignored. And while soot and catalyst particles have a low volume fraction in the sample (< 5%), they may have a larger surface area by virtue of their small size and, in the case of the catalyst, its electronic density is 2-3 times higher than that of SiC. These two effects could make their contribution to scattering intensity significant, but their analysis is beyond the scope of this work.

However, a highly dilute system implies that particles are far enough apart that their scattering is largely independent. This assumption may not be entirely valid for a network of interconnected nanowires, where interference could become significant, in fact, the scattering profile presents a downturn (Figure 3.11) at very-low q suggesting interparticle interaction.[102]

3.4. Macroscopic networks of SiC nanowires

The formation of a freestanding solid is possible due to the high aspect ratio of the SiCNWs (up to 2200 with an average of 773), which favours their entanglement in the gas phase, as also observed for other inorganic nanomaterials.[9,70] For reference, the high aspect ratio of nanowires grown by FCCVD reported is 214 for SiNW[9] and 12.5 for GaAs[19] (see Table 1.3).

As a first approximation and as stated in the introduction, our research group proposed to assess the likelihood of aerogelation by percolation of monodisperse systems, that is, with the aerogelation parameter ($v \cdot s$).

Using that model, the volume concentration was estimated assuming complete catalyst conversion into nanowires, thus using the product of catalyst number concentration with the volume of an average nanowire.

$$v \cdot s = C[\#/cm^3] * \overline{V_{nw}}[cm^3] \cdot s \qquad \text{Equation 13}$$

Assuming conversion of all the fed ferrocene into catalyst of nanowires with average length and diameter. The maximum volume concentration of the nanowires would be 4.3 x 10^{-6}. Thus, the aerogelation parameter value is 3.35 x 10^{-3}. This value lies between those typically required for fibres and in-situ aerogel formation within the reactor (i.e. CNT and BNNT), and the value associated with sheet formation by filtration (SiNW) as seen in Table 1.3. This observation aligns with the sampled aerogel which was confined in space.

While the high aspect ratio of the SiCNWs promotes entanglement, the overall concentration of nanowires remains relatively low. The insertion of the ceramic rod into the reaction zone might disrupt the flow pattern, potentially leading to localised areas with increased nanowire concentration. This localised concentration enhancement could be a contributing factor enabling the formation of the observed macroscopic SiCNW aggregate, that otherwise would not form.

Up until now, we have understood the aerogelation of 1D nanoparticles considering the evolution of an aerosol of individual nanowires and uniformly distributed in the reactor volume. However, recent experimental data obtained by Nabil Abomailek suggest that 1D nanoparticle aggregation occurs rapidly and that aerogelation occurs through aggregate-to-aggregate dynamics.[103]

His analysis of a typical FCCVD run for SiNWs, considering factors such as size distribution and concentration, indicates that the binary collision time between two individual Si nanowires is less than 1 second. This value is notably faster than the residence time for agglomeration, which is the time the nanowires travel before being collected as agglomerates after their individual growth, calculated to be around 50 seconds. This suggests that the aerosol of nanowires quickly transitions into an aerosol of agglomerates, which exhibit slower collision kinetics.

Moreover, agglomerate collisions will still occur faster for 1D nanoparticles than for spheres, due to their increased agglomerate size. Similarly, it will occur faster for long 1D nanoparticles than for those with low aspect ratios. Further analysis of the agglomeration of SiC nanowires and other systems is discussed in Section 6.4.

3.5. SiC nanowires crystalline structure

Figure 3.12 A, B and C present electron micrographs of dispersed SiCNW networks at different magnifications. The nanowires are highly crystalline and present an oxide shell layer, probably grown during reactor cooling. As shown in the HRTEM image and the FFT in the insert (D), the interplanar spacing of the crystalline SiC is d = 0.25 nm, coinciding with the (111) plane of 3C-SiC cubic structure (JCPDS Card no. 73-1665). The FTT also shows elongated lines coming from stacking faults (SF) that are a few nanometres long and are observed parallel to the growth axis. These SF, coming from dislocation in the atomic lattice, are commonly observed in nano-SiC and produce nanosegments of different SiC polytypes.[104] The catalyst particle showed a lattice spacing of 0.198 nm (220) and 0.144 nm (400), corresponding to the intermetallic Fe_3Si phase (Figure 3.12 E).[105]

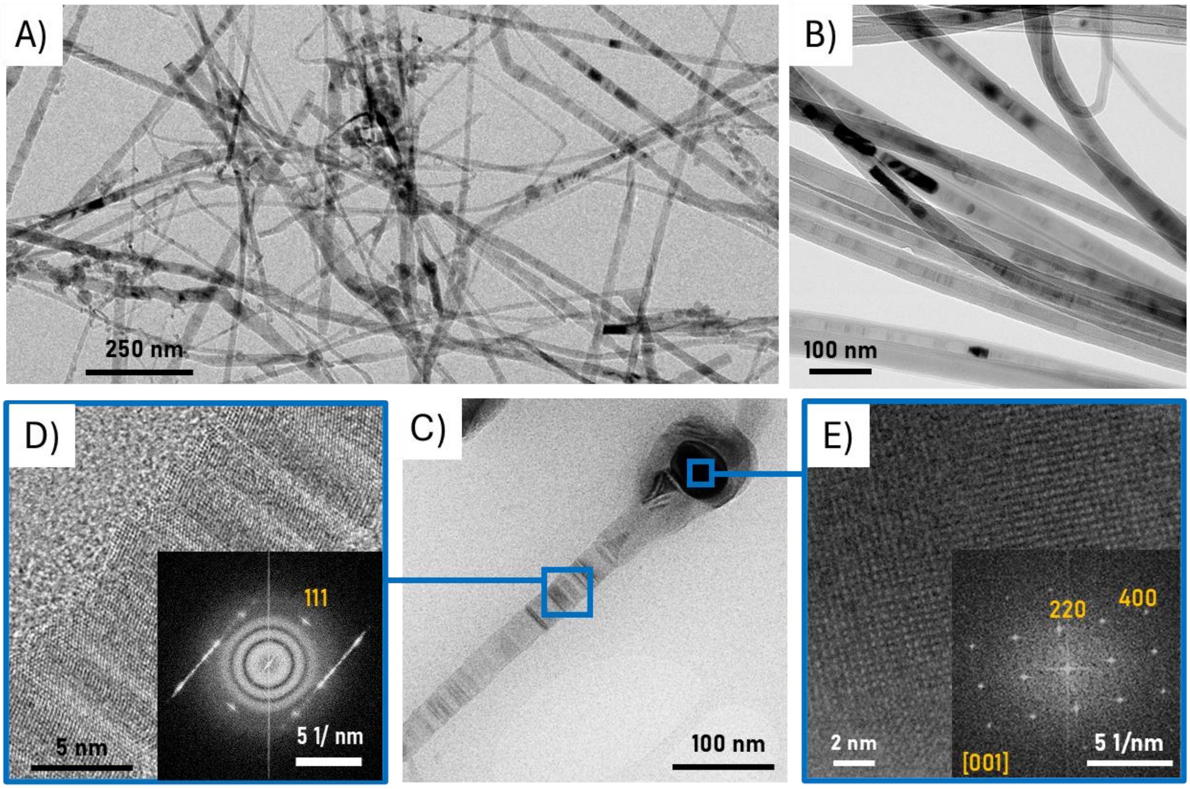

Figure 3.12. A) TEM micrograph of a dispersed SiCNW network B) SiC nanowires with oxide shell C) Sigle nanowire with the typical VLS growth tip and stacking faults. C) HRTEM micrograph showing the nanowire 3C crystal structure and D) Fe_3Si nanowire tip. Indexed FFTs are shown in the insert.

Stacking faults and twinning are common in compound semiconductors, including III-V[106], as the common polytypes have similar free energy only differenced by the plain stacking[107], being ABCABC for cubic 3C, and ABAB, ABCB, ABCACB, for hexagonal 2H, 4H and 6H, respectively. The exact driving force for which this shift occurs is still under debate,[108,109,110] but it has been attributed to shifts in the supersaturation of the catalyst and its effect on the surface tension[111]. Therefore, controlling the reaction temperature, concentration, and atmosphere is crucial to ensure steady growth.

Raman spectroscopy was performed to verify the composition of the sample; the spectra in Figure 3.13 A shows the characteristic peaks at 790 and 940 cm-1 corresponding to the transverse optic (TO) and longitudinal optic (LO) modes of SiC. The peak at 940 cm^{-1} is shifted from the bulk peak (972 cm^{-1}) due to the nanometre dimensions of the SiCNWs.[112] Other peaks found at 870 and 760 cm^{-1} are associated with the SF in the material.[113]

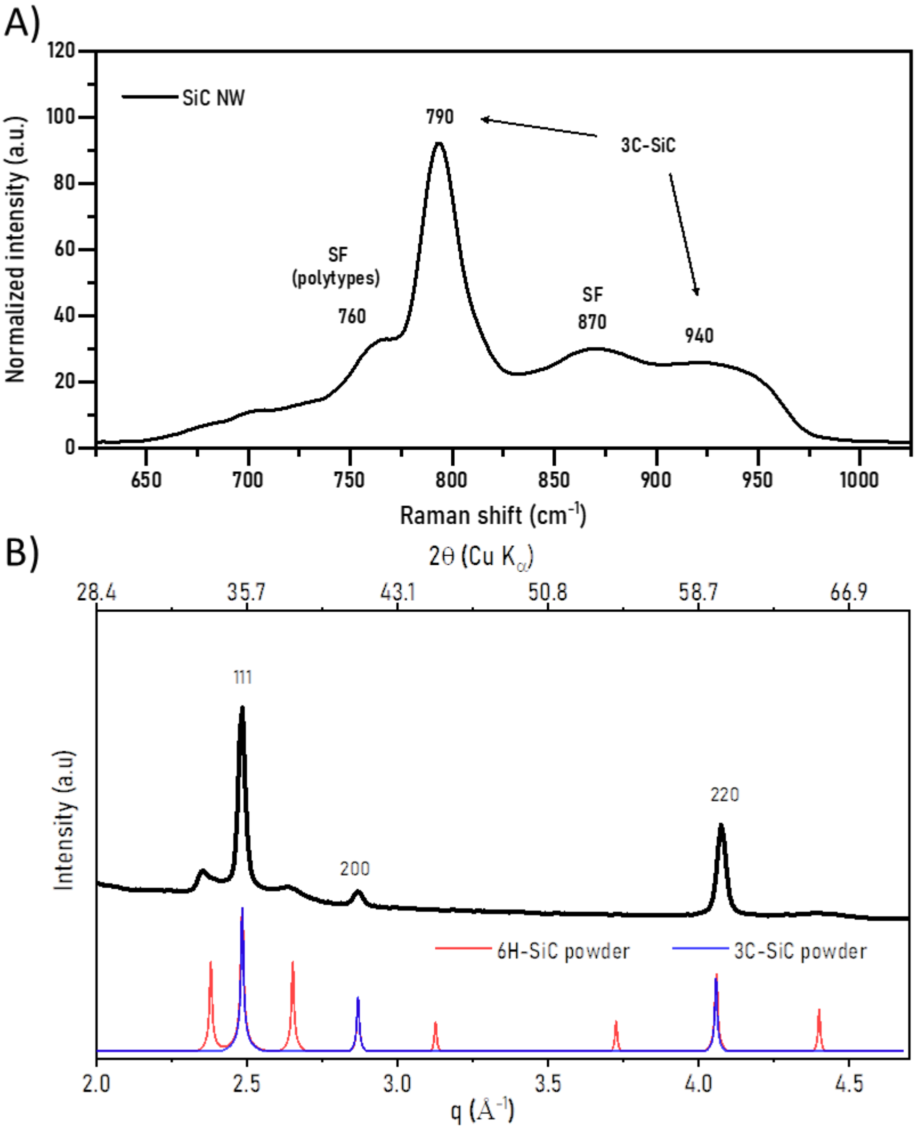

Figure 3.13 A) Raman shift of SiC nanowires presenting anomalies caused by nanosegments of different polytypes produced during growth because of stacking faults (SF) B) Synchrotron X-ray diffraction pattern. Sample compared with the powder pattern of 6H-SiC (red) and 3C-SiC (blue) phase. Adapted from [83].

The crystallinity of the SiC NWs over large sample volumes was confirmed with synchrotron X-ray diffraction (see Figure 3.13 B). The spectra confirmed that the sample was mainly composed of 3C phase SiC with stronger signal on the peaks at 35.7°, 41.5°, 60.1° and 71.8°, corresponding to the planes (111), (200), (220) and (311) of 3C-SiC, respectively. Week signal was found in 34.2° and 38.2° peaks, corresponding to the hexagonal nanosegments generated by the stacking faults; other authors have attributed these peaks to the 6H-[114] or 2H-SiC[115].

The exact stacking sequence to elucidate the polytype in the analysed sample requires further crystal analysis. Application of the Scherrer equation in the three main peaks of the 3C-SiC phase results in an average crystallite size of 19.6 nm. In this case, the crystallite size coincides fairly with the diameter. Nevertheless, it could also be attributed to other crystalline phases without interference, for instance, segments without defects on the length of the nanowire.

Summary of Chapter 3:

This chapter presented the first successful synthesis of long SiC nanowires by FCCVD, with iron as the catalyst and hexamethyldisilane (HMDS) as the precursor. The sampling mechanism of the vertical reactor was adapted to enable position-resolved analysis of the reaction products. Optimal growth conditions were established, resulting in the direct collection of SiC nanowire webs from the 3-cm reaction zone, exhibiting exceptionally high growth rates reaching up to 50 µm/s.

The selectivity towards SiC nanowires was investigated through precursor decomposition and thermodynamic analysis of the Si-C-Fe system. Hydrogen played a crucial role in suppressing competing reactions and promoting the formation of SiC nanowires. A solidification pathway was proposed, explaining the formation of SiC nanowires as the main catalysed product at synthesis conditions. The formation of macroscopic nanowire networks was attributed to the high aspect ratio of the nanowires and localised concentration enhancements.

Finally, the morphology and structure of the synthesised SiC nanowires were characterised. The nanowires exhibited a lognormal distribution of both diameter and length. They were found to have a crystalline structure with a dominant 3C-SiC phase with stacking faults. The crystalline structure was predominantly 3C-SiC with the presence of stacking faults.

Chapter 4 will delve into the development of a new FCCVD reactor designed to enhance reproducibility and expand its applicability to the synthesis of various 1D materials. The chapter will provide a detailed description of the reactor's design, including the catalyst generator, precursor injection system, and in-line monitoring system.

4. Development of a New FCCVD Reactor System

Careful control over synthesis parameters is the only way to ensure the reproducibility and stability of the reactions. After the experience in SiC nanowires synthesis and the attempt to adapt a classical horizontal tubular furnace for following up reactions, the need to design and build a new reactor was found, where all parameters affecting the FCCVD method specifics were considered and optimised. These parameters include flow patterns, wall reactions, precursor and catalyst feeding stability.

Furthermore, high reproducibility is needed to achieve high-throughput experimental methods that help advance understanding of rather unexplored reactions. At the beginning of this thesis, the rate of experiments on reaction conditions was rather low, mainly due to the time consumed in batch characterisation and the problems faced with reproducibility. That is why it is crucial to incorporate advances in in-line characterisation and automation to achieve high-throughput experimentation.

To achieve uniformity within the nanowire ensemble, stable gas flow is essential. Therefore, turbulence must be minimised. Laminar flow offers a predictable velocity distribution, translating to consistent residence time for the nanowires within the reactor. While recirculation vortices and buoyancy-driven flow are unavoidable in any tubular reactor design, a vertical configuration offers advantages. Vertical reactors exhibit improved radial symmetry[14], translating into uniform growth conditions for the nanowires. Additionally, they allow easier collection of reaction products, particularly in the case of large agglomerate formation, where gravity plays a significant role in sedimentation.

The vertical reactor (Figure 4.1) include a ceramic mullite tube with O-ring-sealed flanges at both ends working as the reaction chamber. Although ceramic tubes are susceptible to fractures due to mechanical stress and thermal shock, they offer greater versatility in reaching higher temperatures than metallic tubes. The selected furnace can reach temperatures up to 1600 °C. Before each reaction, a leak check is performed to ensure proper sealing between the flanges and the ceramic tube.

The feeding system ensures that nitrogen and hydrogen gas flows are precisely regulated using mass flow controllers (MFCs). The system allows for the independent control of the nitrogen-to-hydrogen ratio via separate MFCs. The feedstock enters from the top through a modifiable flange (depicted in detail in Figure 4.4) consisting of a main central port and 6 surrounding ports. The middle inlet can be coupled to a concentric injector where the catalyst and reaction precursor make their way into the reactor at adjustable positions. The outermost inlets are designed to feed the sheath flow system.

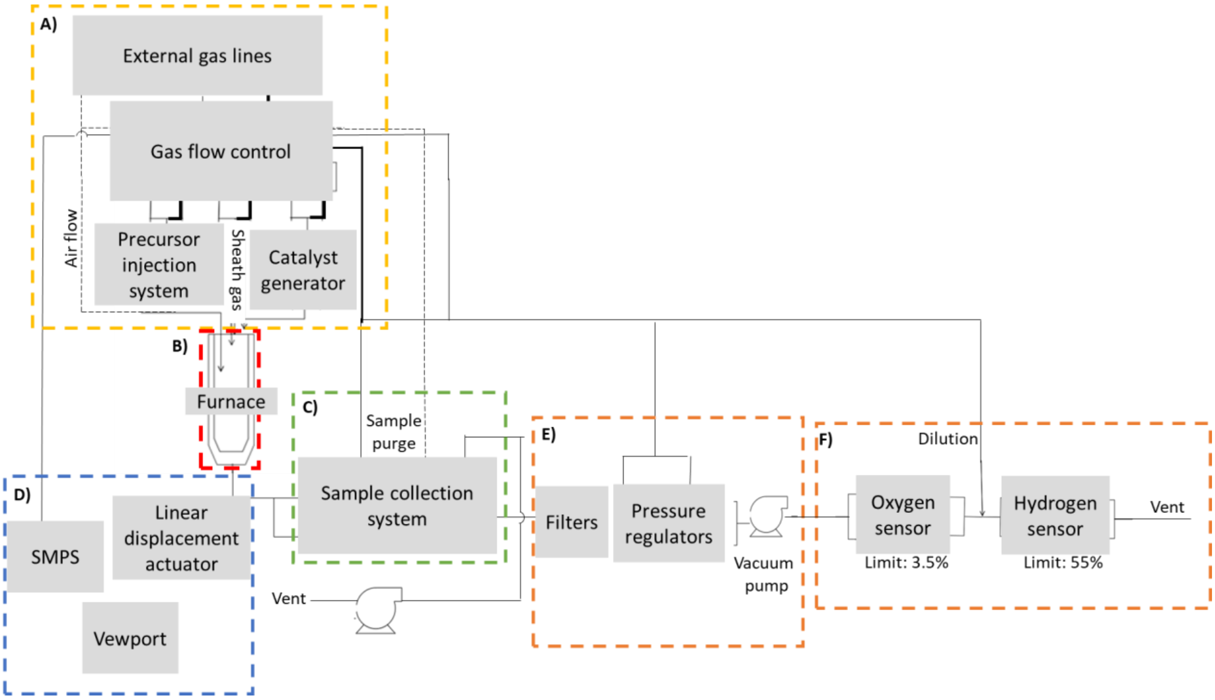

Figure 4.1 New FCCVD reactor piping and instrumentation diagram: A) Feeding system B) Reaction Chamber C) Sampling system D) Monitoring system E) Pressure control F) Sensors

A constant pressure within the reaction chamber is maintained by a semi-automated system comprising a vacuum pump, a back pressure regulator, and a piezoelectric pressure meter, all controlled by a LabVIEW program.

The sampling system consists of the simple filtration of the reaction stream to collect the solid products. The diameter of the outlet piping was kept as wide as possible to avoid losses of agglomerates to the walls before sampling. It incorporates a pneumatic valve and a purge system to guarantee the safety of the process. The purge system prevents the release of reaction gases into the surrounding environment while impeding air from entering the reactor.

Furthermore, the system incorporates an automated movable probe to extract solid products from various locations within the reactor. This enables the investigation of potential spatial variations in the product characteristics. An extra outlet port was incorporated at the end of the reaction chamber to facilitate in-line monitoring using a scanning mobility particle sizer (SMPS), which is further discussed later in Section 4.3. This allows for qualitative observation of reaction stability and potential changes. The port can be further utilised to combine morphological characterisation of the solid product with gas chromatography and mass spectroscopy for gas characterisation.

Further development of the in-line measurements should be focused on the simultaneous analysis of all reaction products, namely, gas products, aerosols of small catalyst particles, aerosols of large 1D particles and macroscopic networks.

Lastly, safety considerations are paramount when working with explosive gas mixtures like hydrogen and oxygen at elevated temperatures and potentially pressurised conditions. Following safety protocols, although the reactor was operated at atmospheric pressure, a warning alarm was implemented in case of overpressure. Additionally, sensors were strategically placed at the reactor outlets to continuously monitor gas concentrations and ensure they remained below the explosive limit. The hydrogen flow was diluted before venting, and a normally closed electrovalve was installed to automatically cut off the hydrogen supply in case of an alarm.

4.1. Catalyst Generation: Thermal Evaporator Design

The home-built thermal evaporator was designed to replace the SDG due to increased electromagnetic noise interference with the digital communications controlling the reactor. The design is relatively simple: A power supply is connected to two electrodes, and a Tungsten resistance closes the circuit. A piece of gold is placed on top of the resistance to get heated. A graphite plate is placed in between to prevent gold losses to the tungsten resistance. The gas flow passes perpendicular to the resistance to carry the maximum amount of evaporated gold.

Due to the high current passing through the circuit, contacts with the resistive boat need to be excellent; otherwise, extreme heating in a small area produces evaporation of the boat material, poisoning the catalyst production.

A viewport was added at the top end of the evaporator case to enable the use of an infrared pyrometer, and a digital camera was used to monitor the temperature of the gold source and the state of the system, respectively. Figure 4.2 A shows the 3D design built using FreeCAD software.

The size and concentration of particles can be tuned with the current passing and the flow of the carrier gas. The size distribution of the particles measured right before entering the tubular reactor at different power conditions and carrier flows are presented in Figure 4.2 B.

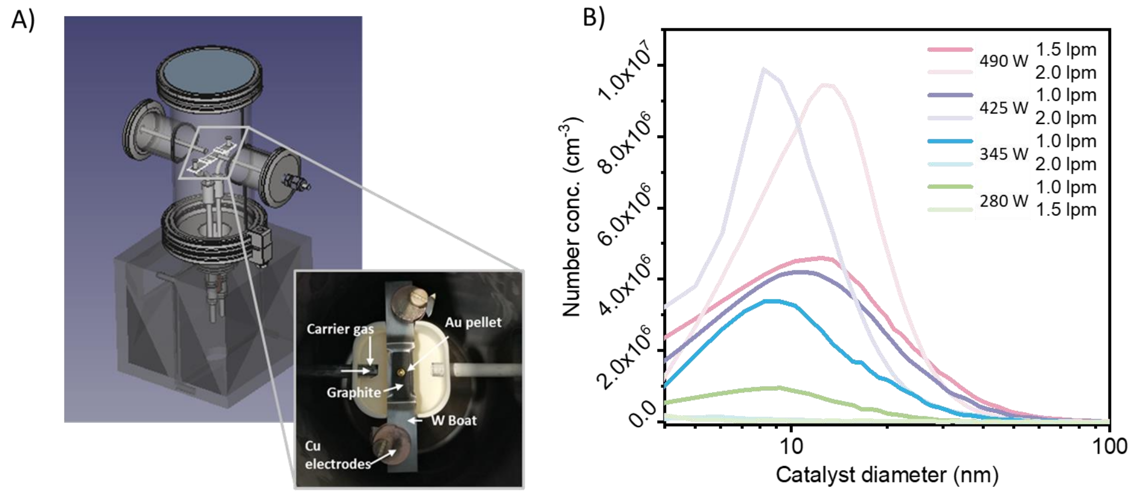

Figure 4.2 Thermal evaporator A) 3D design and digital picture of the evaporator arrangement and B) Size distribution of gold aerosols produced at different powers and carrier gas flows, sampled right before the reactor inlet.

Further optimisation of the equipment is needed to achieve better stability over time. In addition, there are important discrepancies between catalyst size distribution when measuring before and after the vertical furnace; these differences are present throughout all the evaporator powers tested. The number concentration and geometric mean diameter extracted from the SMPS curves generated with 1 lpm and different evaporation powers are presented in Figure 4.3. The number concentration decreases one order of magnitude after passing through the reactor (Figure 4.3 A). And the mean diameter escalates more quickly with the evaporator power for the particle assessed downstream (Figure 4.3 B). This can be attributed to the aerosol coagulation process, where particles aggregate to form larger particles, and to thermophoretic losses promoted by the steep heating ramp. However, it represents a great challenge to identify the exact conditions delivered to the reaction zone, hence participating in the nanowire growth.

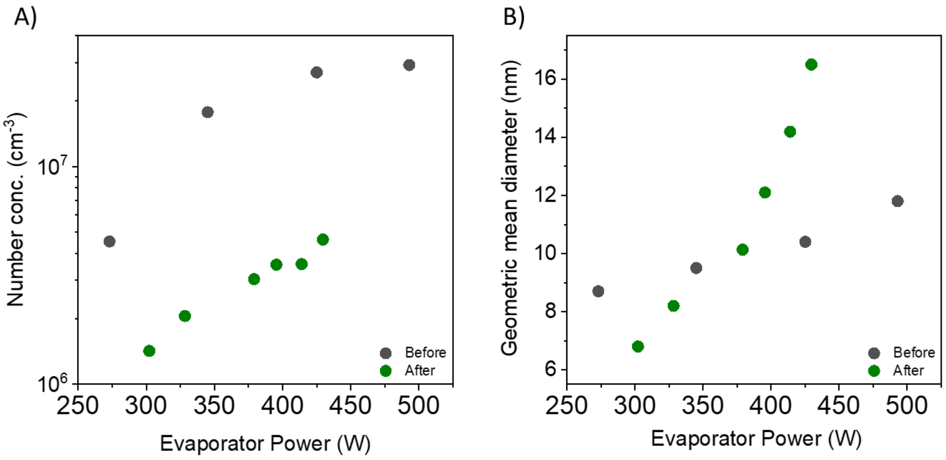

Figure 4.3 Number concentration and mean diameter of gold particles generated by thermal evaporation, using 1 lpm H_2 as carrier gas and mixing with 3 lpm, equivalent to other flows participating in the reaction (precursor carrier gas and sheath gas). The measurements were performed in ports located before and after the tubular furnace.

4.2. Precursor Injection: System Design

Metalorganic compounds are often used in CVD due to their versatility, as they can be synthesised according to the needs of the process.[34] Ideally, a significant gap between precursor evaporation and thermal decomposition is desirable. However, practical constraints, such as toxicity and availability, often derive in the use less-than-ideal precursors, as it is the case of Tin (II) 2-ethylhexanoate, the precursor chosen in this work for tin oxide nanowire growth. Hence, the need to design an injection system that prevents the early decomposition of the liquid precursors.

The system (Figure 4.4) incorporates a concentric nebuliser with a venturi nozzle to atomise the liquid into a heated chamber. For a detailed understanding of nebuliser operation and principles, readers are referred to [116,117]. In essence, the nebuliser features two inlets: one for the carrier gas, which accelerates as it passes through the narrowing nozzle, and another, conducting to the inner tube, for the liquid precursor. The high-velocity gas stream atomises the liquid at the nozzle tip. In the designed system, a constant carrier gas flow is sustained while the liquid injection rate is modulated using a syringe pump. The precursor temperature in the syringe is controlled to adjust its viscosity.

The atomisation process generates a droplet size distribution, including both fine and larger droplets. Under conditions of high liquid injection rates, droplet formation can be disrupted, leading to liquid accumulation and potential dripping from the nozzle. To mitigate these issues and ensure a stable vapour phase, a heated antechamber is positioned downstream of the nebuliser. This chamber is maintained at a temperature below the precursor boiling point. Because of their small size, the atomised droplets get vaporised[118] while the dripping liquid is captured, ensuring a stable vapour phase and preventing pulsations within the reactor.

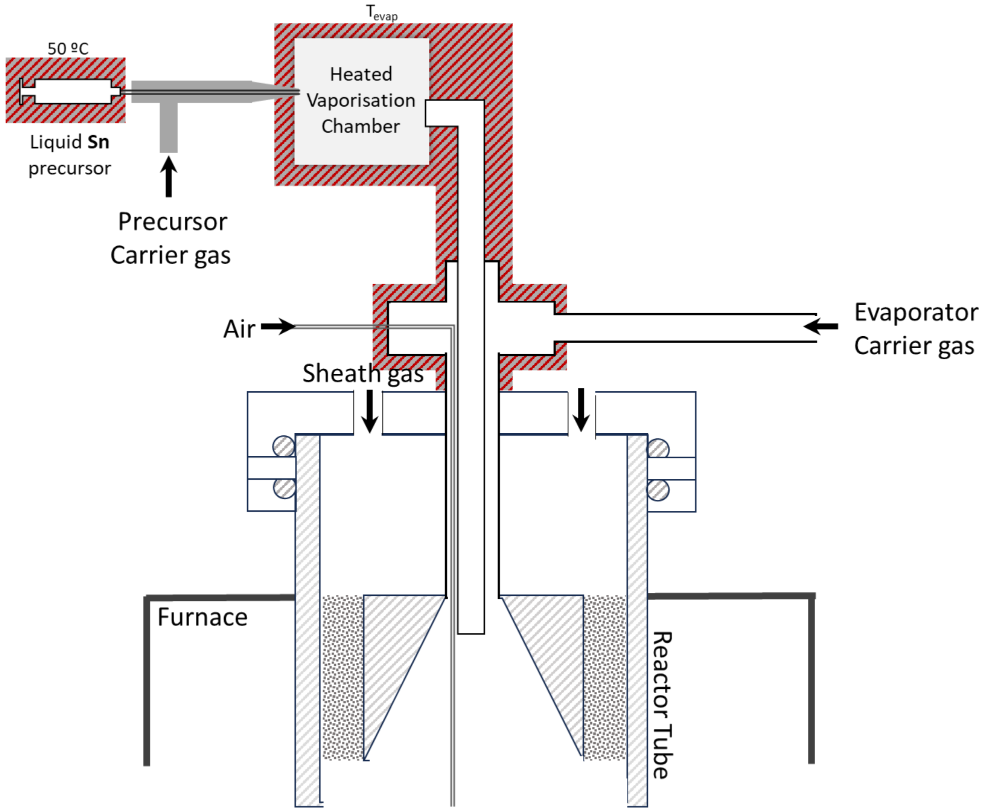

Figure 4.4 Scheme of the liquid precursor injector design coupled to the reactor feeding system through the innermost inlet. The liquid injection system consisting of a Syringe pump, a nebuliser and a heated vaporisation chamber.

Because of the complex mechanism involved in the precursor injection, the precursor feed rate was calculated empirically and described here as a tool for similar quantification problems. The study was divided into two stages, one looking into the effects of the temperature in the antechamber and the other related to the injection rate given by the pump.

In the first stage, thermal gravimetric analysis (TGA) isotherms were obtained to evaluate the impact of temperature on precursor evaporation.[119] A linear relationship between weight loss and time was observed, indicating pure evaporation without decomposition up to approximately 120 °C (Figure 4.5 A). Above this temperature, a deviation from linearity suggested the onset of decomposition in N_2 atmosphere. Plotting the evaporation molar rate against the inverse temperature yielded a linear trend consistent with the Antoine equation (Figure 4.5 B). It is hypothesised that in a hydrogen atmosphere, this linear behaviour would persist at higher temperatures due to suppressed particle formation.

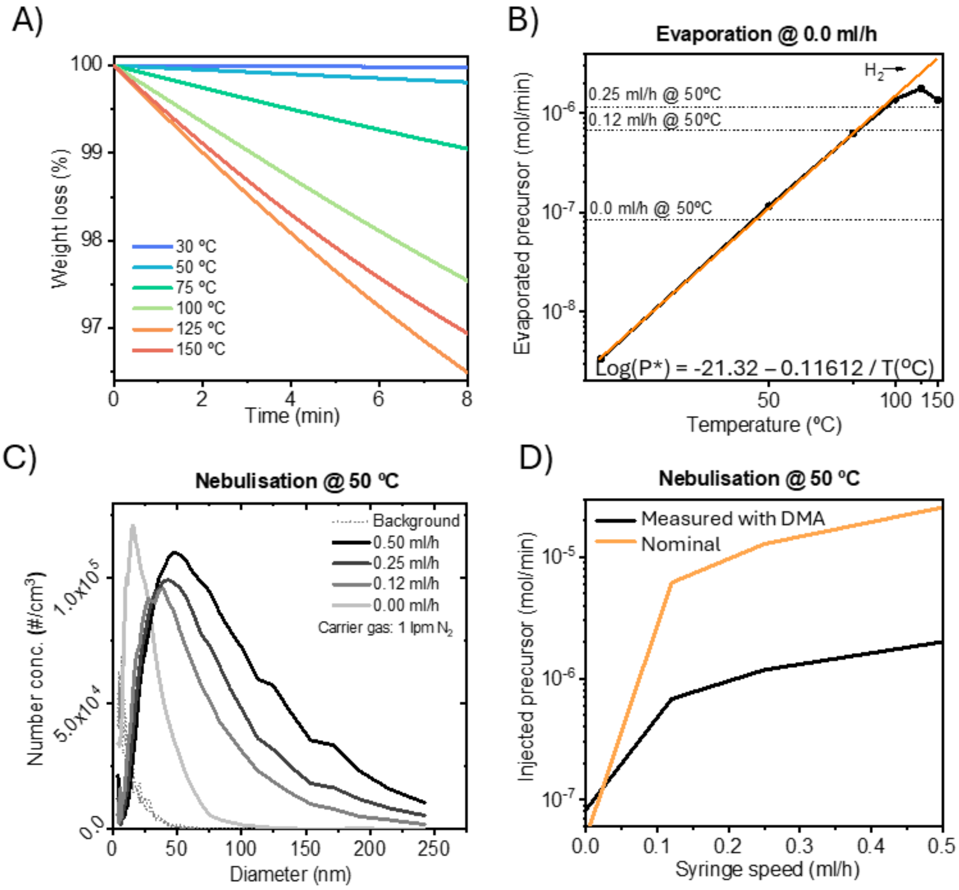

Figure 4.5 Precursor evaporation and injection efficiency. A) TGA isotherms of the precursor at different temperatures (with 90 sccm N_2 flow). B) Arrhenius plot of the evaporation rate compared with experimentally measured at different injection rates. C) Particle size distribution obtained by SMPS for different injection rates. D) Correlation between nominal and experimentally measured at different injection rates at a constant carrier flow (1000 sccm).

To assess the influence of injection rate, the system was operated at a constant temperature (50 °C) and gas flow rate (1000 sccm) while systematically varying the pump liquid injection rate. To quantify the actual amount of precursor reaching the reactor, a Scanning Mobility

Particle Sizer (SMPS) was employed at the reactor outlet. The reactor was set to 700 °C, and an oxygen-rich environment was established to ensure complete conversion of the precursor into SnO_2 particles. The resulting DMA curves, presented in Figure 4.5 C), provided data on particle size distribution. The particle concentration was converted into molar flow rate by assuming a spherical particle shape and considering the total gas flow rate. This analysis revealed that only approximately 10% of the nominally injected precursor was effectively transformed into particles, as illustrated in Figure 4.5 D. It is noteworthy that the evaporation rate at 50ºC coincides fairly with the particle concentration detected at an injection rate of 0.0 ml/h where the sole precursor source was the heated precursor, confirming that the mass calculated from the DMA measurements is in good agreement with the actual amount of precursor entering the reactor.

The overall precursor feed rate was then calculated using the calculated evaporation rate and the corrected injection rate as follows:

$$\dot{n}_{prec,sn} = (\eta_{inj} * \dot{n}_{prec,inj} + \dot{n}_{prec,evap}) \qquad \text{Equation 14}$$

$$\dot{n}_{Sn\,fed}\left[\frac{mol}{min}\right] = 0.1 * \dot{n}_{prec,inj}\left[\frac{mol}{min}\right] + 10^{\frac{-112.5}{T\,[°C]}-4.83} \qquad \text{Equation 15}$$

Where $\dot{n}_{prec,evap}$ is the evaporation rate at a certain temperature obtained by the TGA isotherms analysis. $\dot{n}_{prec,inj}$ is the injection rate equivalent to the nominal rate selected in the syringe pump and η_{inj} is the injection efficiency, calculated as the ratio of DMA measured mass after conversion of the precursor gas to SnO_2 particles and $\dot{n}_{prec,inj}$. With this modified empirical expression, it is then possible to estimate the effective Sn feed ($\dot{n}_{prec,sn}$) considering injection and temperature.

A significant factor contributing to the relatively low injection efficiency ($\eta_{inj} \approx 0.1$) is the formation of spherical microparticles arising from the incomplete vaporisation of larger droplets generated during the atomisation process (Figure 4.6). As they travel inside the reaction chamber, these precursor droplets decompose directly to SnO_2 and get partially reduced to SnO. Due to their larger size (0.4-2 µm), the microparticles remain undetected by the SMPS. Thus, the precursor used for their formation is already accounted for in the injection rate efficiency value.

Previous studies by J.H. Kim *et al.*[120] already reported the production of SnO_x spheres using a similar spray pyrolysis approach. They observed the formation of smooth-surface SnO_2 microspheres or microporous SnO-SnO_2 composites depending on the reactor atmosphere, inert or reductive, respectively. The microspheres produced in our experiments exhibit similar characteristics.

Any result of sample characterisation described in Chapter 5 corresponds to the referred nanomaterial, requiring a previous step to separate it from the microspheres.

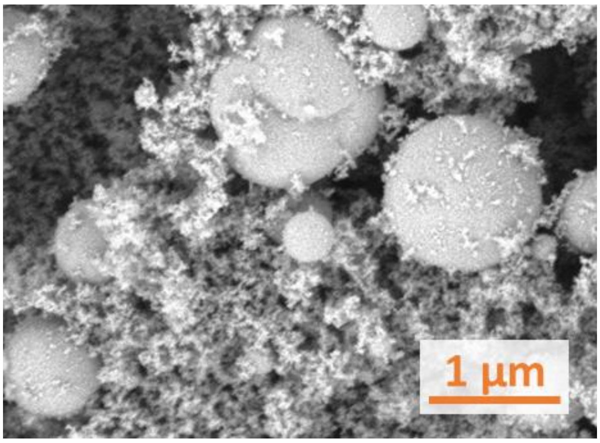

Figure 4.6 Spherical micro-particles as a by-product of atomisation. A) Sample taken in a O_2 rich environment. The nanosized particles were used to determine the injection rate efficiency, while the microspheres remained undetected.

4.3. In-situ sampling and online monitoring

For the synthesis of SiC nanowires (Section 3) in-situ sampling and in-line measurements of the solid products were key for the optimisation and understanding of the reaction. In this second stage, the growth of SnO nanowires and other solid by-products was monitored in-line with a scanning mobility particle sizer (SMPS). To facilitate these measurements, the FCCVD reactor was equipped with an outlet port at the end of the heated zone, from which a fraction of the gas stream was passed through the DMA. This configuration enabled the continuous acquisition of size distribution curves that integrated the contributions of all solid products.

Real-time analysis of the size distribution curves provided valuable insights at different stages of the experimental procedure. Firstly, the catalyst insertion and stability were monitored to ensure consistent nanoparticle concentration and size after the replacement of the tungsten boat or gold pellet. As mentioned in the catalyst generation section of this chapter, factors such as the contact between copper electrodes and the resistive element, as well as the position of the carrier gas inlet and outlet, can influence the power required to maintain a constant temperature and consequently affect the catalyst size distribution.

Analogously, the online monitoring system was used to confirm the successful injection and stabilisation of the precursor over time. This was evidenced by the consistent appearance and steady behaviour of the size distribution curves on the SMPS software. The specific size and shape of these curves were influenced by the injection rate, temperature, and N_2/H_2 ratio employed (see Section 5.2 for a detailed discussion of their impact on SnO nanowire synthesis).

Furthermore, by using the online monitoring system during the preparation of every experimental run, we were able to observe the interaction of the catalyst with the precursor vapour. In the optimal expected case, the precursor SPMS curve would exhibit a decrease in counts as the catalyst curve increased proportionally with the evaporator power. Simultaneously, the catalyst curve would shift towards larger diameters, indicating the incorporation of precursor species into the nanoparticles. Figure 4.7Figure 4.7 SMPS curves used to confirm precursor and catalyst injection. The contributions from both species are labelled accordingly. shows this trend, the injection of an arbitrary precursor concentration in a 50% H_2 environment produces a prominent peak centred around 7 nm (blue). As the catalyst evaporator source power increases from 0 to 500 W, this peak gradually disappears while the catalyst curve, located at values > 10 nm, emerges and subsequently shifts towards larger sizes.

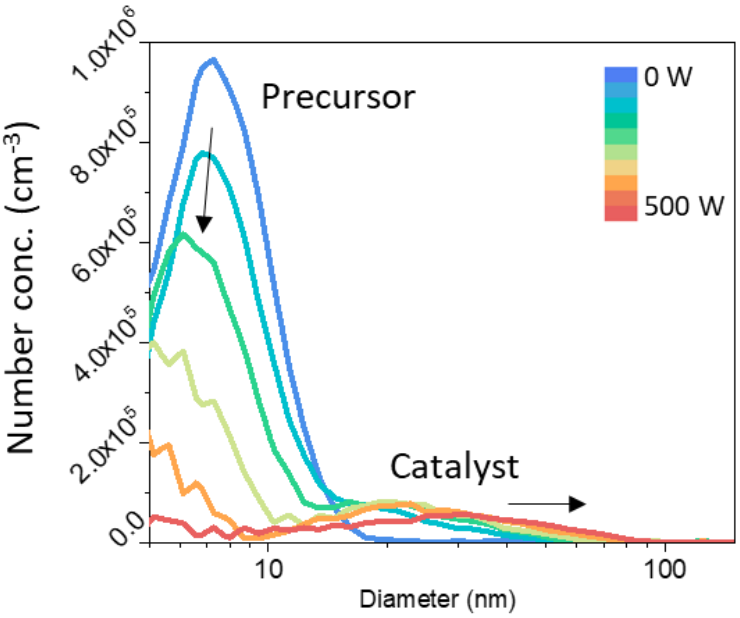

Figure 4.7 SMPS curves used to confirm precursor and catalyst injection. The contributions from both species are labelled accordingly.

This technique was also helpful during synthesis parameter exploration. Examples of SMPS curves obtained in different experiments are provided in Figure 4.8. Each curve represents one experiment where Sn precursor, gold catalyst and air were fed, but they differ in concentration, temperature and N_2/H_2 ratio. By analysing the shape of the SMPS curves, the primary solid product could be inferred prior to filtration sampling and characterisation. Bimodal trends were indicative of the presence of nanowires within the sampled gas (A) along with fine soot-like particles. Conversely, narrow, unimodal curves are more likely to correspond to inactive spherical catalyst particles (B), while broader peaks suggest the presence of larger soot-like particles (C).

Identifying the main products by their size distribution curves, allowed tuning the reaction condition (i.e. precursor injection rate) to minimise soot formation. The online monitoring system served as a valuable tool for observing the transition from conditions favouring homogeneous nucleation to those where the interaction with the catalyst became prevalent.

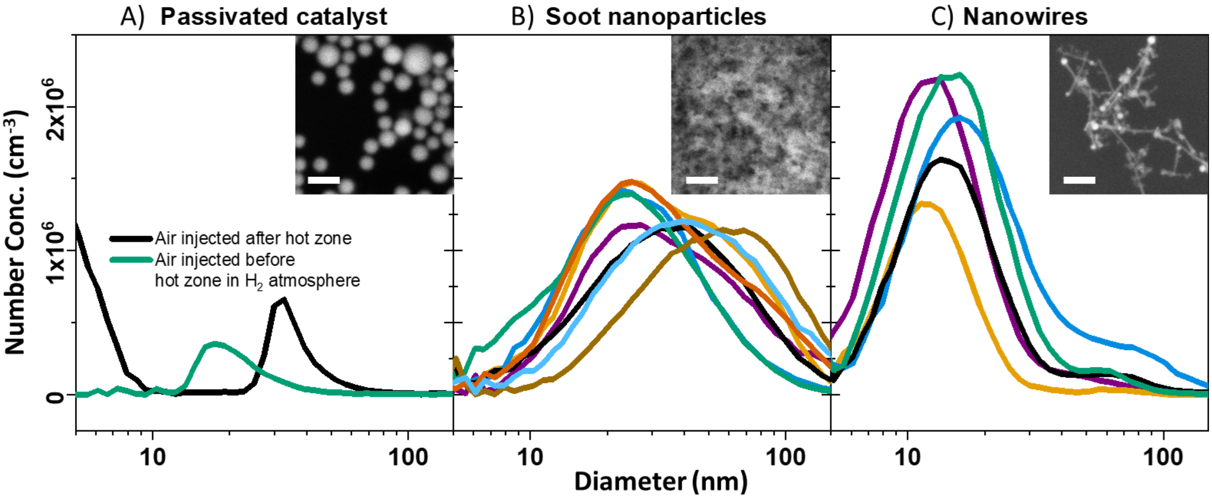

Figure 4.8 SMPS curves of different products, namely passivated catalyst, soot nanoparticles and nanowires (micrographs of each product in the insert, scale bar = 100 nm. Each curve was obtained under different conditions. Note that all plots have the same scale.

Figure 4.9 illustrates the use of the online monitoring system to minimise soot formation during a systematic increase in precursor concentration. For this experiment, synthesis parameters were maintained at the optimal conditions for SnO nanowire growth, except for the temperature in the precursor vaporisation chamber, which was increased from 100 to 180 °C, resulting in a gradually higher effective Sn precursor concentration. The SMPS measured the solid product in real-time from the port at the end of the reaction chamber as the temperature increased.

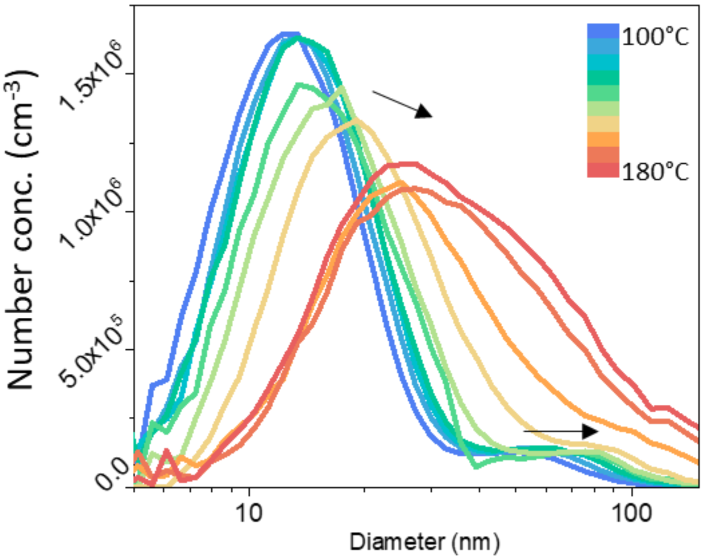

Figure 4.9 Observed shift in the selectivity of the reaction from nanowires towards soot. Blue to green plots correspond to nanowire growth conditions, as the concentration increases, the bimodal curves are lost and broader distributions emerge, corresponding to the formation of particles by homogenous nucleation, in red.

One can appreciate that at 100 °C, the SMPS curve (in blue) exhibited a bimodal trend similar to those presented in Figure 4.8 A, indicating the presence of nanowires. As the temperature increased, the curves (in green) slightly shifted towards larger values while maintaining a relatively constant number concentration ratio, probably suggesting an increase in the length of the nanowires. Upon further increase of the temperature, the bimodal trend was lost, and broader curves (in red) like those presented in Figure 4.8 C emerged, indicating the dominance of homogeneous nucleation and hindering nanowire growth. The observation was confirmed with SEM imaging of filtered samples.

The online monitoring system facilitated not only a fine-tuning of the reaction conditions to balance nanowire growth and homogeneous nucleation but also the real-time observation of other changes within the system. This enabled rapid responses to any deviations from optimal conditions, helping to prevent potential problems and minimise losses or safety hazards.

Although the information gathered from the SMPS curves provided valuable insights into product formation and interaction, it's important to acknowledge their limitations. This method does not represent a quantitative analysis, nor should it be used as the sole source of information about the FCCVD system.

The accuracy of size distribution curves of non-spherical particles is compromised by the working principle of the DMA, because nanoparticles of varying sizes, shapes, and densities can exhibit identical mobility diameters. Consequently, while the SMPS can detect interactions between catalyst and precursor, it may not be able to differentiate between particles with similar characteristics, such as long nanowires and enlarged catalyst particles, or accurately determine their actual dimensions.

To address these limitations, tandem characterisation techniques, which involve measuring mobility, mass, aerodynamic diameter, and other properties of the same 1D nanoparticle aerosol, have been employed in previous studies.[121,122] However, such techniques are complex and were not available for this thesis.

It is also important to note that the particle dimensions (for spherical and 1D particles) delivered by the SMPS may deviate from their actual sizes due to aggregation phenomena. Additionally, the experimental setup can introduce measurement errors, particularly related to the distance travelled between the collection site and the measurement equipment.

For instance, during monitoring of the precursor injection, the SMPS curves might indicate the presence of small nanoparticles (< 10 nm); however, samples collected by filtration under the same conditions may not reveal any solid products. This discrepancy can be attributed to the nucleation of precursor vapours within the sampling piping.

Similarly to online measurements, *In situ* measurements within the reactor offer valuable insights into the synthesis process by generating data directly linked to position-resolved experimental conditions. When coupled with automation, these measurements can yield large amounts of significant information.

The new FCCVD reactor was equipped with a digitally controlled linear displacement actuator designed and built by Miguel Vazquez-Pufleau. It could be coupled to a vacuum sampling probe or thermocouple. This system facilitated *in situ* measurements at various positions within the reactor (Figure 4.10 Movable sampling probe for *in situ* measurements with a reactor temperature of 700 °C. A) Set-up scheme, the linear displacement actuator moves a probe inside the reactor B) Catalyst evolution map A), enabling the visualisation of dynamic reaction behaviour.

To monitor catalyst evolution throughout the reactor, the linear displacement actuator was coupled to a thin ceramic tube (⌀ = 6mm) inserted inside the reaction chamber in the radial central position. A portion of the reactor gas (700 sccm) was extracted from various positions within the reactor and passed through the SMPS after dilution with 10 lpm of N_2. An independent size distribution was obtained for every centimetre from the top to the centre of the reactor.

Figure 4.10 B presents a catalyst evolution map from the reactor's top to the hot zone (0 - 42 cm). This plot was obtained using 1 lpm H_2 as the carrier gas in the evaporator and a power of 450 W, without the introduction of precursor. Each pixel line in the plot corresponds to the size distribution at a specific centimetre position, with the colour code representing the number concentration. Size distributions measured at the DMA fixed port at the end of the reactor are plotted below for comparison.

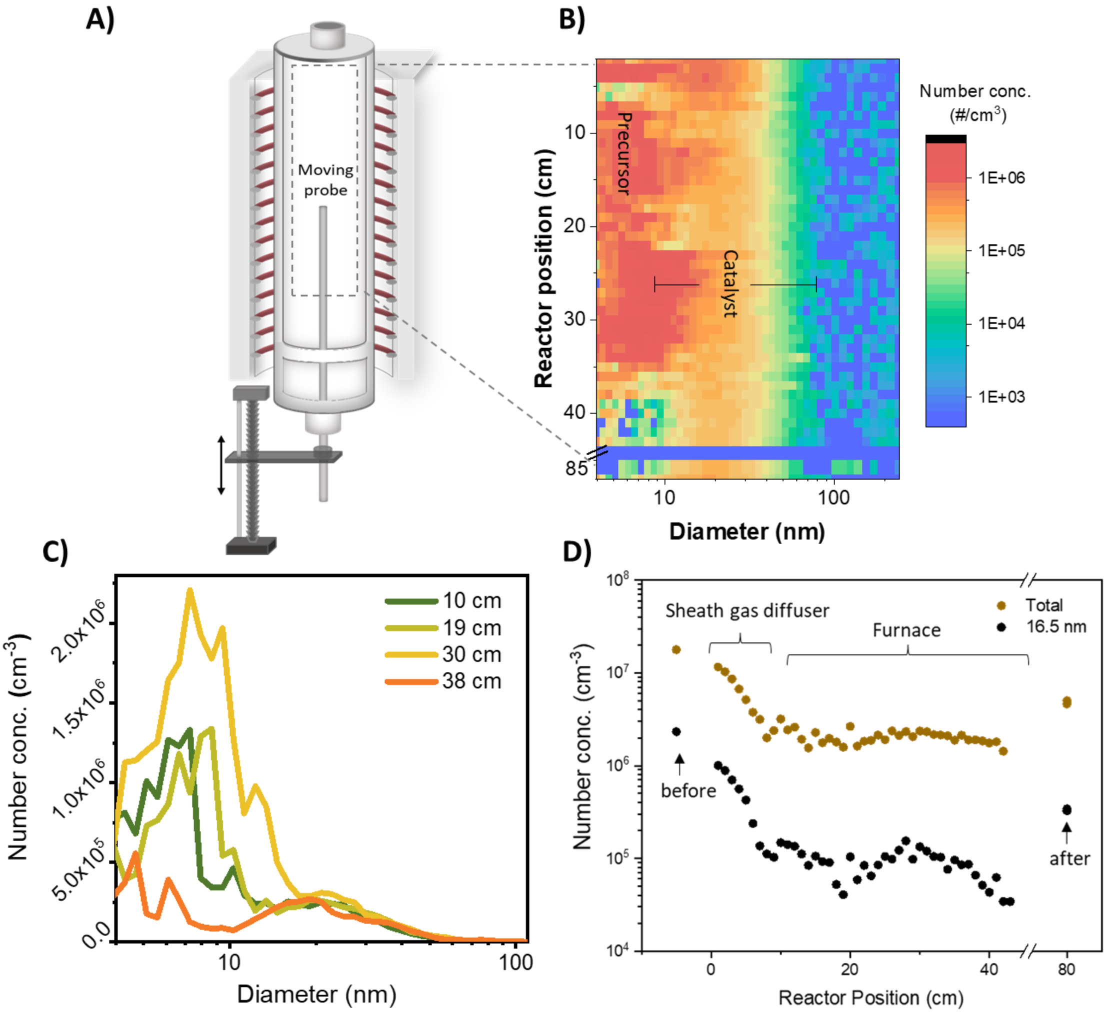

Figure 4.10 Movable sampling probe for *in situ* measurements with a reactor temperature of 700 °C. A) Set-up scheme, the linear displacement actuator moves a probe inside the reactor B) Catalyst evolution map C) Catalyst size distribution curves at different positions in the reactor, equivalent to a pixel line in the evolution map, and D) Evolution of the catalyst total number concentration and that of particles with 16.5 nm of equivalent diameter. The corresponding points measured before and after the vertical furnace are also plotted.

The examples of size distribution curves at different positions, plotted in Figure 4.10 C, reveal two main contributions, one from small particles (<10 nm) with high number concentration (red) and the other one, centred around 20 nm with lower concentration (orange). Their bimodal distribution resembles the curves presented in Figure 4.7, thus likely corresponding to the presence of precursor vapour and catalyst. Although no precursor was intentionally injected, residual precursor from previous experiments may have been present and nucleated within the sampling probe piping. The small particles were detected in the initial stages of the reactor but disappeared upon reaching the hottest region, suggesting the introduction of the precursor vapour into the catalyst. Additionally, the mode catalyst size (16.5 nm) is larger than that measured before entering the reaction chamber, closer to 10 nm (see Figure 4.2 B), evidence of the incorporation of Sn from the residual precursor.

Focusing on the catalyst contribution within the mid-range diameter range in Figure 4.10 B, and with the aid of the corresponding number concentration evolution plots (total particles and particles with 16.5 nm diameter) in Figure 4.10 D, we can extract information about the main loss mechanisms and estimate the catalyst concentration involved in later nanowire growth.

Firstly, we observe an initial difference in equivalent delivered number concentration between the ex-situ port located before the vertical furnace and the initial point inside the reactor. This loss most likely occurs in the piping and represents, along with the losses inside the evaporation chamber, the major challenge to overcome to increase the efficiency of catalyst delivery through thermal evaporation.

Then, the initial zone inside the reactor (0-8 cm) decays with a linear trend. This zone corresponds to the section of the reactor preceding the interaction with the sheath gas flow, which has a conical shape. The decrease in flow velocity due to the increase in the transverse section area, may induce error in the measured concentration, which should be considered and corrected.

Beyond this zone, the catalyst distribution maintains a relatively constant concentration and mode size of approximately 20 nm throughout the remaining length. However, the concentration appears to be lower than the one measured in the designated SMPS monitoring port after the reaction chamber. This illustrates the limitations of the moving probe, which can induce errors due to long piping and non-consistent radial position.

While a significant portion of the catalyst is lost in the initial part of the reactor, the remaining catalyst demonstrates steady behaviour throughout the reactor, unaffected by the temperature profile. This positive characteristic indicates the catalyst's readiness to interact with the other reactant species. Understanding the factors influencing catalyst loss and aerosol measurements remains crucial for optimising the FCCVD process and increasing productivity.

The movable probe system was not limited to particle analysis. A thermocouple was also attached to the probe to measure temperature profiles within the reactor. To determine the optimal scanning speed for accurate temperature measurements, a study was conducted on a vertical reactor at a set temperature of 570 °C. Figure 4.11 A presents the temperature profiles obtained at different scanning rates.

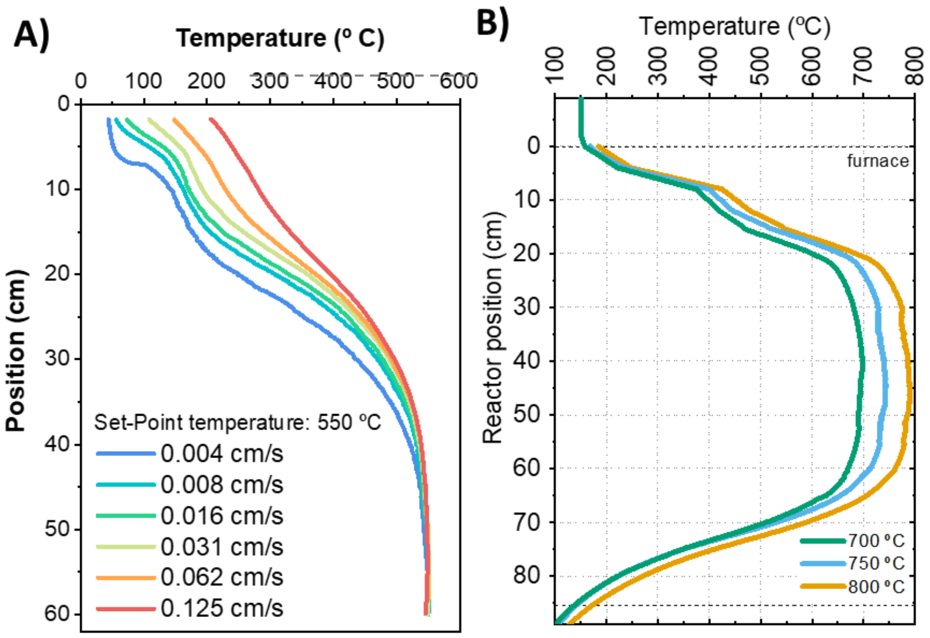

Figure 4.11 A) Effect of scanning rate on temperature profile measurements. B) Reactor temperature profile for various temperatures

The results indicated that faster scanning rates could lead to overestimated temperatures and missed variations, while slow rates would extend the experimental time. To minimise errors associated with the thermocouple's long response time, a scanning rate of approximately 0.01 cm/s was employed to obtain the temperature profile at synthesis conditions for SiC (presented in the last chapter, Figure 3.2) and SnO nanowires (Figure 4.11 B).

As a final note, it is crucial to consider the operational limitations of the instruments used for automated measurements. Each instrument has a specific range of conditions within which it can reliably acquire data. Signal biases, such as noise, drift, and delay, must be carefully evaluated. Additionally, the scanning rate should not exceed the intrinsic response time of the detector to ensure accurate measurements of the process.

Summary of Chapter 4:

This chapter discussed the critical aspects of a new reactor aimed to achieve reproducible and efficient nanowire synthesis via FCCVD. The new vertical reactor was constructed to optimise gas flow patterns, minimise wall reactions, and ensure safety.

To improve catalyst and precursor feeding, a thermal evaporator was developed to replace the existing system, offering improved control over catalyst particle size and concentration. Additionally, a nebulizer-based system was designed to deliver the precursor into the reactor while preventing premature decomposition. The precursor injection efficiency was quantified through empirical analysis.

Furthermore, to increase the experimental efficiency, an in-line monitoring system utilizing a scanning mobility particle sizer (SMPS) was implemented to track the reaction process in real-time. This enabled the observation of catalyst and precursor injection, as well as product formation. Additionally, a movable probe system allowed for in-situ measurements of temperature profiles and particle size distributions within the reactor. This provided insights into catalyst behaviour and temperature profiles.

The emphasis on reproducibility and in-line monitoring is paramount for achieving reliable and scalable nanowire production. The newly developed reactor will be utilised in the synthesis of SnO nanowires, discussed in Chapter 5.

5. SnO Nanowires growth by FCCVD

In the third stage of this thesis, the new inhouse reactor was used with the objective of growing, for the first time, tin oxide nanowires via FCCVD.

5.1. Set-up adapted to SnO nanowires growth mechanism.

SnO nanowires were grown using Tin(II) 2-ethylhexanoate ($Sn(oct)_2$) as tin precursor, gold aerosols as catalyst and air as oxidising agent. The new vertical FCCVD reactor was adapted with an injector consisting of concentric inlets (Figure 5.1 A). The innermost inlet is designated for the liquid precursor where the carrier gas serves the dual purpose of atomisation and transport from the vaporiser chamber. The second inlet delivers the catalyst, and the sheath flow (outer inlet) serves to prevent wall reactions and can also be used as a diluent of the reductive atmosphere. The air flow in charge of the oxidation of the nanowire is injected through a capillary with movable position inside the reactor. Real-time monitorisation of the solid products is performed with an SMPS (scanning mobility particle sizer), and they are collected by simple filtration of the gas stream with a polyethersulfone (PES) filer.

The concentric inlets in the continuous flow reactor allow the decoupling of the 3 stages involved in the VLS growth of the SnO nanowires (Figure 5.1 B). a) Precursor decomposition b) Au-Sn alloying c) growth mediated by oxidation. Each of these stages is initiated by the injection of the different species involved in the growth at a certain temperature in the profile of the furnace, and they are discussed one by one in this chapter.

More than 140 experiments were performed in order to find the optimal conditions (See Annex 3 for details). The set-up facilitated the observation of trends in every stage and an efficient sampling in those conditions that represented it better.

In all experiments, carried with a set-point temperature of 700 °C in the furnace, the precursor was maintained at 50 °C to decrease its viscosity, then vaporised using a concentric flow of 1 lpm of carrier gas (N_2 or H_2) into an antechamber kept at a temperature raging 50 – 200 °C. The precursor vapour was mixed with the gold aerosol at the entrance of the vertical tubular furnace. The catalyst seeds are generated via thermal evaporation with modulating power and carried with 1 lpm H_2.

Later, the carrier gas flow is accompanied by a 2 lpm sheath flow; the same linear velocity between the sheath and inner flows is sustained to minimise turbulence. Then, 20 sccm of air is injected with a movable capillary at different positions inside the rector. The reaction products, assessed systematically with SEM after each run, exhibited high reproducibility.

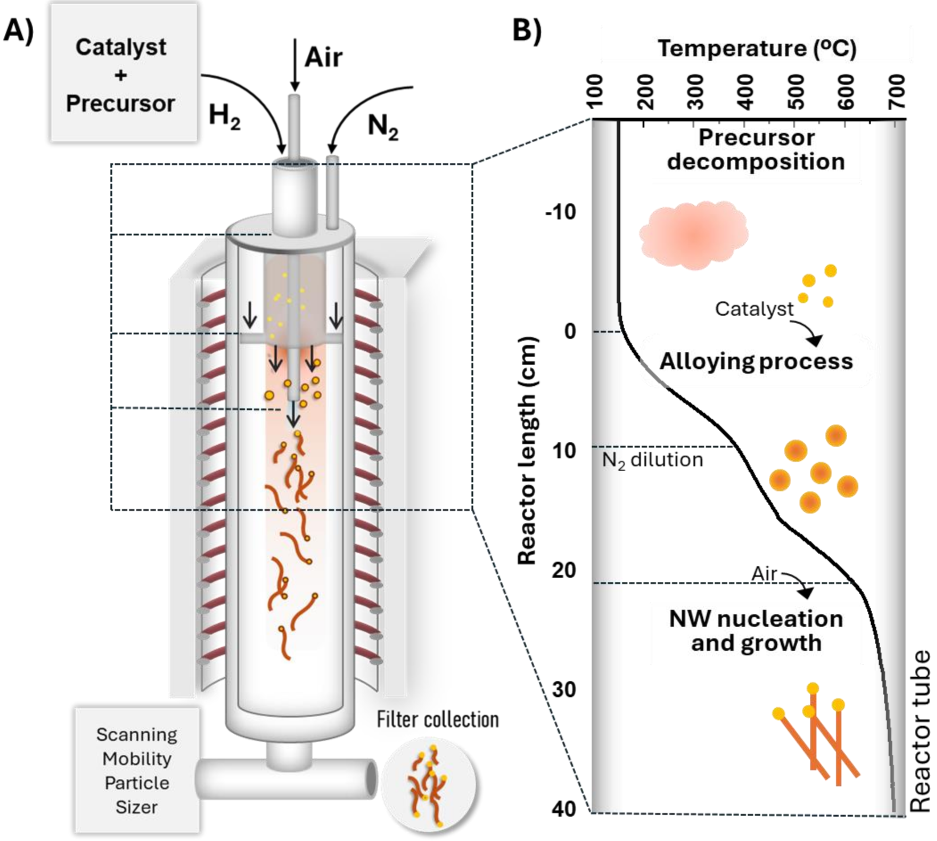

Figure 5.1 A) Reactor set-up for SnO nanowires and B) growth mechanism

5.2. Precursor decomposition stage

The initial stage of the synthesis process involves the vaporisation and decomposition of Tin(II) 2-ethylhexanoate (Sn(oct)$_2$). Precursor injection is detailed in Section 4.2. While Sn(oct)$_2$ is commonly used in polymerisation reactions, its thermal decomposition behaviour is relatively unexplored.

To achieve the desired nanowire growth, it is crucial to maintain the precursor in the vapour phase and prevent the formation of SnO$_x$ particles. Oxygen is expected to induce early particle formation directly from decomposition. Li et al.[123] reported obtaining high-quality SnO$_2$ particles through flame pyrolysis of Sn(oct)$_2$ in an oxygen-rich environment, proposing a direct conversion from precursor to oxide. Similarly, a study[124] on indium ethylhexanoate thermal decomposition proposed that the decomposition at inert conditions also leads to the formation of the oxide, while, In vacuum, they suggested a pathway to metallic indium. Although there is a lack of information in a reductive atmosphere, we expect it to prevent oxidation.

Taking into account the literature studies, we proposed the following possible reactions for the precursor selected:

$$C_{16}H_{30}O_4\mathrm{Sn}\ (\mathrm{l}) + O_2 \rightarrow \mathbf{SnO_2\ (np)} + CO_2 + H_2O + C_xH_yO_z \quad \text{Equation 16}$$

$$C_{16}H_{30}O_4\mathrm{Sn}\ (\mathrm{l}) \rightarrow \boldsymbol{Sn\ (g, l)} + CO_2 + C_xH_y \quad \text{Equation 17}$$

To elucidate the decomposition behaviour of the Sn precursor at the reaction temperature, an SMPS was coupled to the reactor to monitor particle formation. At a set-up temperature of 700 °C, Sn(oct)$_2$ was injected while systematically adjusting N$_2$, H$_2$, and O$_2$ flow rates to manipulate the atmosphere.

The experimental results, as depicted in Figure 5.2 A, demonstrate that SnO$_2$ particle formation is significantly influenced by the gas environment. While inert conditions (N$_2$) promote soot particle nucleation, the introduction of oxygen intensifies particle growth and abundance. The crystalline particles resulting from homogeneous nucleation present a strong signal in WAXS corresponding to the tetragonal SnO$_2$ phase. HRTEM confirmed the composition with a d-spacing of 0.26 nm corresponding to the (101) plane (Figure 5.2 B, C).

In contrast, the addition of hydrogen effectively suppresses particle formation. These findings strongly suggest that hydrogen plays a crucial role in preventing premature precursor decomposition and promoting the formation of Sn vapour, a prerequisite for subsequent nanowire growth.

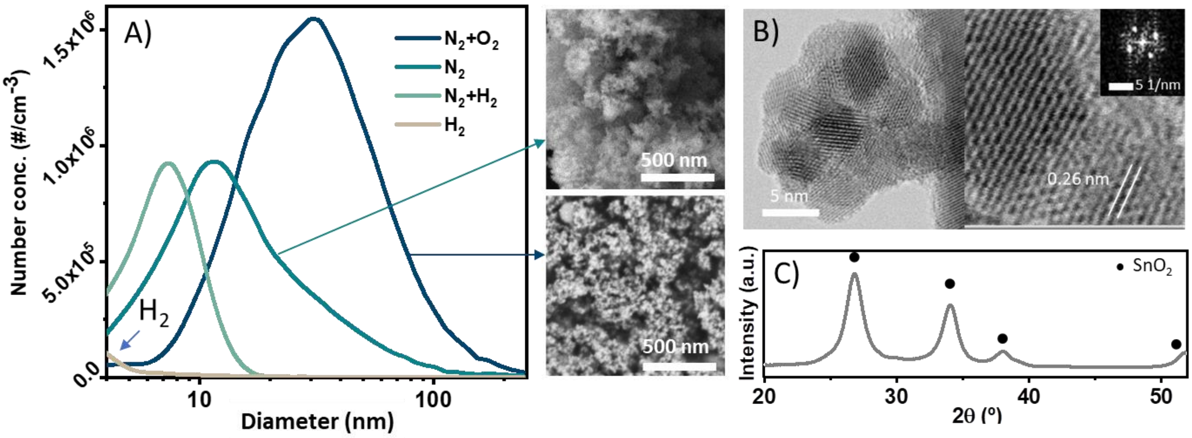

Figure 5.2 Particle formation from tin precursor injection at different atmospheres. A) Size distributions measured directly from the reaction stream B) HRTEM of soot particles from synthesis with 50% H_2. C) WAXS pattern of nanoparticles form in an oxygen-rich environment.

In conclusion, precursor decomposition must occur in a highly reductive atmosphere (100% H_2) to prevent soot formation and instead favour decomposition to gaseous Sn species, which can be later incorporated into the catalyst. The alloying process is discussed in the next section.

5.3. Au-Sn alloying process

The second stage of nanowire growth involves the interaction between the precursor and the catalyst. Previous studies on tin oxide nanowires synthesised via SCVD reported the conversion of the gold catalyst to stochiometric AuSn.[35,125] This study aims to investigate the in-situ formation of Au-Sn alloy particles before nanowire growth. It is important to note that the Au-Sn system (Figure 5.3) exhibits complete solubility at the experimental temperature of 700 °C.

To facilitate alloy formation, a reductive atmosphere was established in the reaction zone by employing only hydrogen without oxygen introduction. This suppressed soot nanoparticle nucleation and promoted the diffusion of Sn in Au, leading to the formation of AuSn alloy particles. Au-Sn alloy particles were collected downstream of the furnace for characterisation. The procedure was repeated at a progressively increasing precursor injection rate.

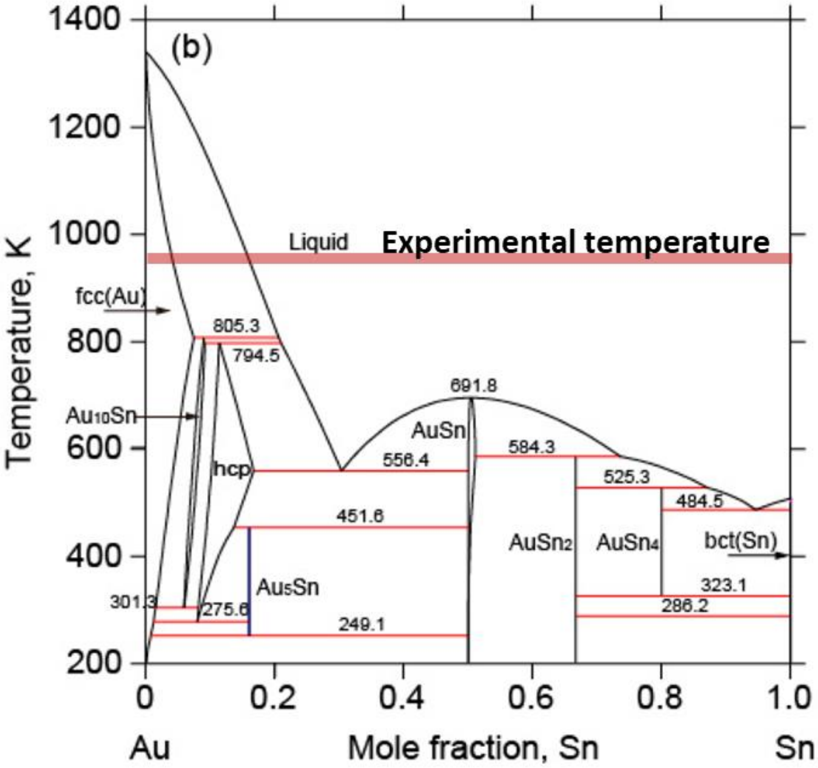

Figure 5.3 Au-Sn phase diagram, above 690K, the system presents full Sn solubility in Au Image from [126]

It was observed that the mean volume of the alloy particles increased proportionally with the precursor injection rate (as shown in Figure 5.4 A), indicating a consistent incorporation process. Furthermore, WAXS analysis of the particles (Figure 5.5 B) revealed a progressive increase in Sn content within the Au-Sn particles as the precursor injection rate increased. At low precursor concentrations, the particles exhibited a predominantly gold composition (Au peak at 38.5°). Upon increasing the precursor feed rate, characteristic AuSn alloy peaks emerged at 40.4° and 41.5° alongside prominent Sn peaks at 30.8, 32.2, 44.0 and 44.9°. Further elevating the injection rate resulted in the pronounced Sn peaks, from the Sn-rich alloy composition.

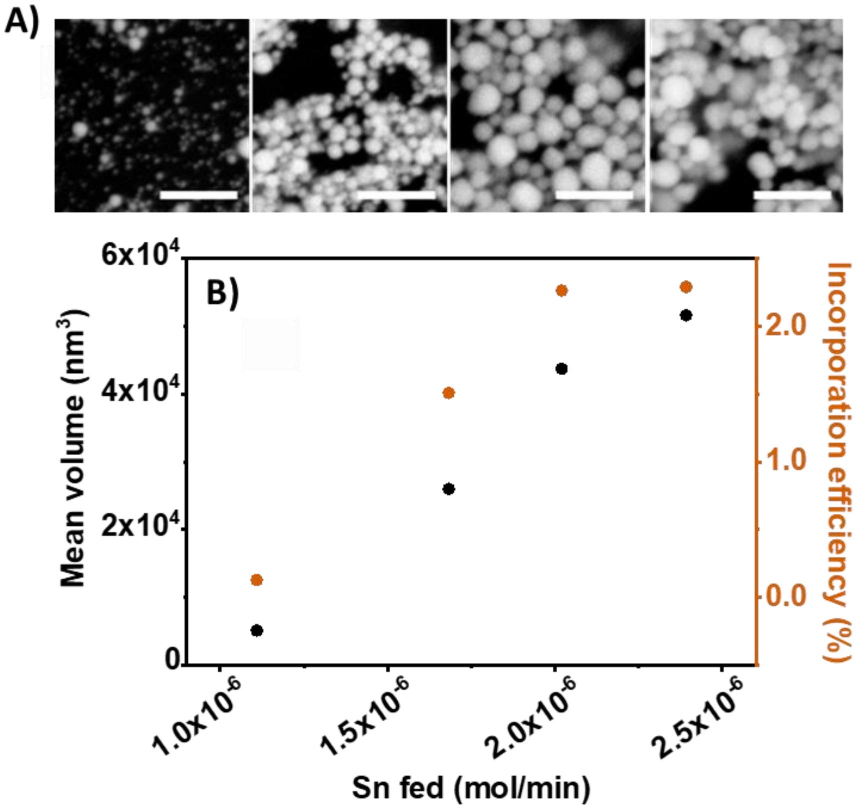

Figure 5.4 Particle size increases with increasing precursor feed A) SEM micrographs of the particles corresponding to each data point in B. B) Left axis: Mean particle volume as a function of Sn feed, calculated from the geometric mean diameter of particles obtained through image analysis. Right axis: Calculated incorporation efficiency.

The amount of Sn in each particle (Equation 18) was estimated from the volume increase with respect to the initial catalyst volume, assuming ideal mixing for the liquid Au-Sn system, and that the incorporation of Sn does not affect the size distribution of Au mixed with Sn. Then, the incorporation efficiency (Equation 19) was calculated as the ratio between Sn fed to the reactor and the total estimated amount of Sn in the particles. The results are presented in Figure 5.4 B. It was found that the incorporation process is more efficient as the concentration of Sn vapour rises within the reactor, with up to approximately 2.5% of the Sn feed into the reactor being incorporated into the alloy.

$$Sn\ incorparated\ [mol] = \frac{(\bar{V}_{particle}[cm^3] - \bar{V}_{catalyst}[cm^3]) * \rho_{Sn}[\frac{g}{cm^3}]}{M_{Sn}\ [\frac{g}{mol}]} \qquad \text{Equation 18}$$

$$\eta_{incorporation} = \frac{Sn\ incorparated\ [mol] * N_{Catalyst}\left[\frac{1}{cm^3}\right] * Q\left[\frac{cm^3}{min}\right]}{\dot{n}_{Sn\,fed}\left[\frac{mol}{min}\right]}\ x\ 100 \qquad \text{Equation 19}$$

These experiments were performed at the highest thermal evaporator power of the experimental setup, resulting in a relatively high Au catalyst concentration. Since incorporation efficiency is proportional to the number of catalyst particles, the values obtained under these conditions represent the maximum achievable in the system in its current configuration.

The low incorporation efficiency is similar to the low precursor conversion in CNT[65] and Si[64] FCCVD synthesis, that are under 10 and 1%, respectively. An important implication of this is that the catalytic Sn intake does not significantly reduce the overall Sn concentration, ensuring that sufficient Sn remains available for nanowire formation. For reference, at nanowire growth conditions, the volume increase of the catalyst particles would correspond to a nanowire length ranging from 37 to 1400 nm, for the lowest and highest feeding rates, respectively.

The composition of the particles, e.g. percentage of Au, Sn and AuSn, was calculated taking into account the amount of Sn incorporated (Equation 18) and under the assumption that only solid Au, AuSn, and Sn would form after cooling, as no other phases were observed in the WAXS patterns.

The composition, calculated from the volume change of the particle, is presented in Figure 5.5 A along with the WAXS patterns of the corresponding sample (Figure 5.5 A, each point in Figure (A) corresponds to the WAXS pattern at its right (B)). The calculations coincide reasonably well with the WAXS experimental data. At low feeding rates, the Sn content in the Au-Sn particles was calculated to be only 17%, meaning that only this proportion of AuSn would form after cooling, resulting in a WAXS pattern dominated by a pronounced gold peak. Increasing the Sn feed rate would surpass the amount of gold present in the particles, leading to the solidification of both AuSn and metallic Sn in progressively higher Sn/AuSn ratios. As a result, the WAXS patterns show increasing Sn peaks, while the AuSn peaks become less pronounced.

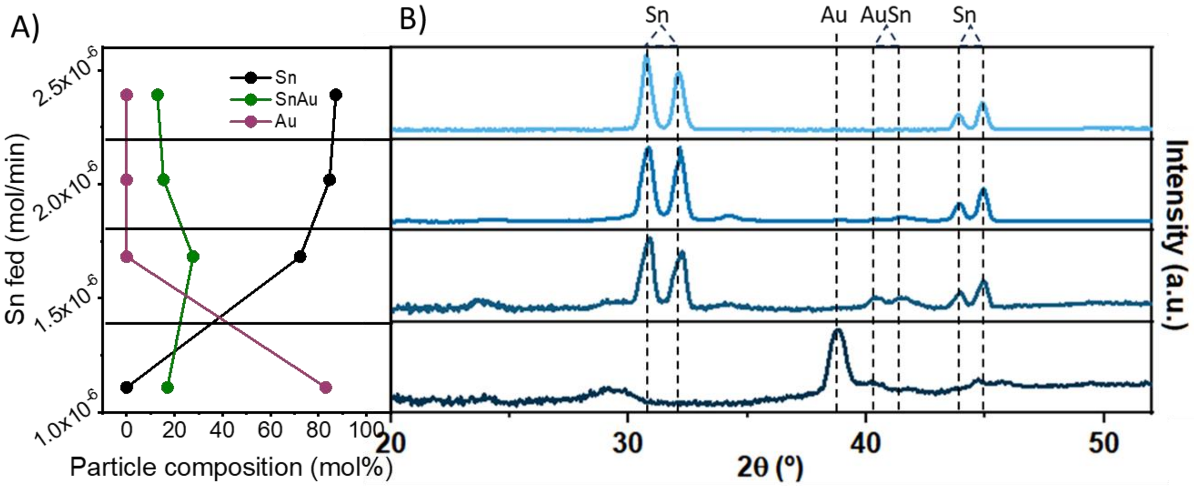

Figure 5.5 A) Alloy particle composition calculated through volume increase; note that the vertical axis corresponds to the Sn feeding rate. B) Corresponding WAXS pattern of the alloy particles.

Although the calculated alloying efficiency was relatively low, the Sn content within the particles increased rapidly as they travelled inside the reactor, reaching nearly 90%. Such high Sn concentration could interfere with the catalyst-driven nanowire formation, potentially hindering the unidirectional growth. This issue will be explored in greater detail in the next chapter, where nanowire nucleation is discussed.

5.4. SnO nanowire nucleation and length increase

To produce oxide nanowires, unidirectional growth should be favoured over full coverage of the particle. Bürger et al.,[45] in an extensive study of SnO_2 on substrates, emphasised the importance of controlling oxygen introduction to maintain the active catalyst surface. In the context of carbon nanotube (CNT) growth, it has been observed that catalyst encapsulation occurs at larger particle sizes where the amount of carbon required to form a graphitic layer represents a lower percentage of the particle total mass.[127]

To follow the evolution of the catalyst-precursor pair, we conducted experiments at synthesis conditions, e.g. 50 %vol H_2/N_2 and controlled catalyst and precursor injection. The air injection port was inserted progressively lower into the reactor. Solid product samples were collected at the outlet of the reactor for analysis.

When air was added in the initial segment of the reactor (approximately 10 cm), oxygen exposure led to the rapid formation of SnO_2 nanoparticles, hindering interaction with the catalyst, consistent with our previous observations on precursor decomposition. This happened before the dilution of the H_2 flow with N_2, hence in a highly reductive atmosphere.

Upon deepening the oxygen injection point, a mixture of SnO_2 soot and non-uniform nanowires was observed in the collecting filters. This suggests that the reductive atmosphere in the first 10 cm facilitated the Au-Sn alloying process, while the injected air promoted the nucleation and growth of nanowires from those particles. However, the excess precursor vapour that was not fully decomposed and incorporated into the catalyst also reacted with the injected oxygen, leading to the formation of SnO_2 soot. The highest selectivity toward SnO nanowires was found at an injection position of 22 cm, right before the hot zone of the reactor. Details on their morphology, crystallinity and composition are further discussed in section 5.6.

Beyond the optimal nanowire growth region, the injection of the oxidising agent resulted in the "freezing" of the alloy particle growth, presumably through surface oxidation. By systematically varying the oxygen injection position, we observed a correlation between particle size and residence time in the reactor, indicative of Sn incorporation (Figure 5.6 A and C). This suggests that Sn incorporation increases progressively as the catalyst travels within the reactor. Thus, the air injection can be located where the Sn/Au content of the particle is optimal.

WAXS patterns of the collected samples (Figure 5.6 B) were analysed to elucidate the core-shell particle composition. The main peaks corresponded to Sn (30.8, 32.2, 44.0 and 44.9°) and SnO (29.7, 33.2°). An increase in the Sn/SnO intensity was observed as the air injection point was moved further downstream, suggesting that the oxidation occurs primarily on the surface, while the incorporated Sn remains in the bulk.

Two main factors can be attributed to the inactivation of the catalyst in deep air injection positions. Firstly, the higher temperatures in these regions can lead to more rapid oxidation of the catalyst surface, hindering its catalytic activity. Secondly, and more likely, the excess of Sn in the Au-Sn alloy promotes radial oxidation instead of unidirectional growth.

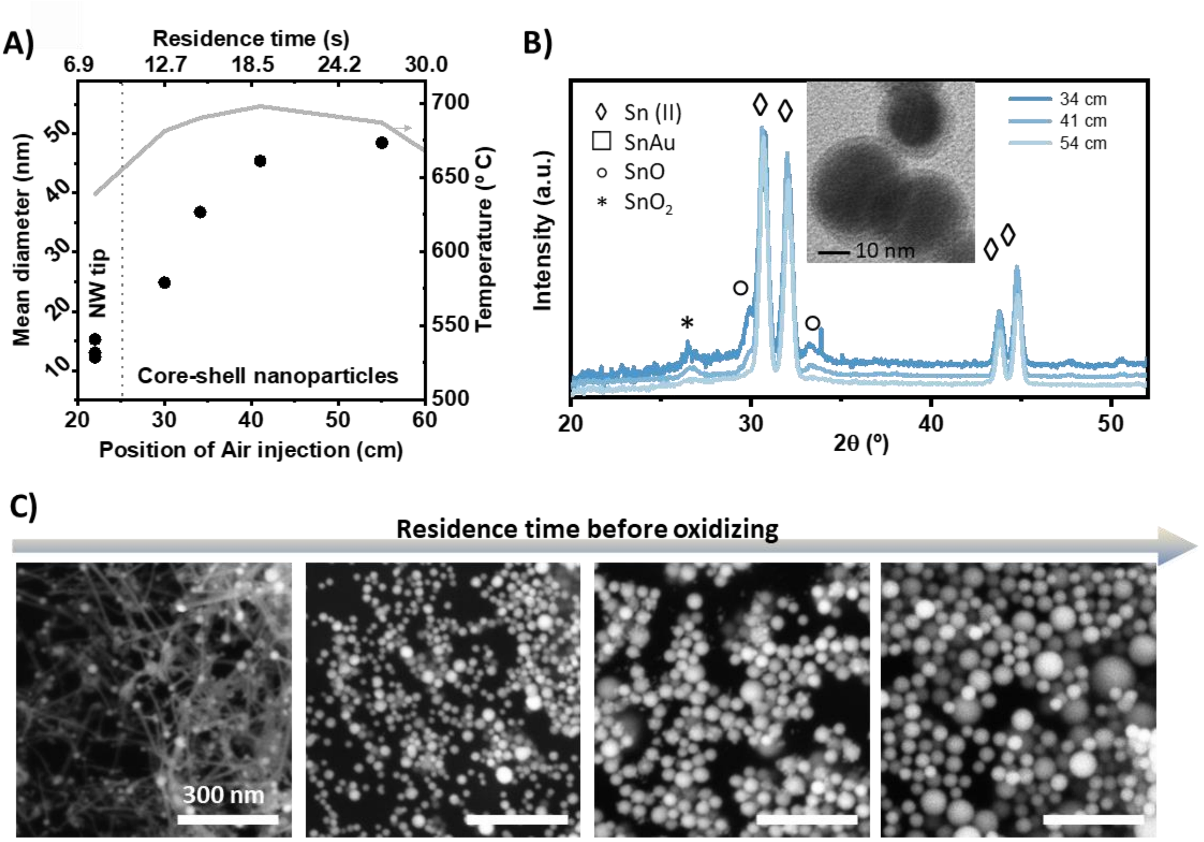

Figure 5.6 A) Core-shell particle volume increase with residence time. The data points at 22 cm correspond to nanowire tips grown from standard synthesis or particles obtained by suppressing nanowire growth with a 100% H_2 atmosphere B) WAXS pattern of Au-Sn particle at different air injection positions C) Electronic micrographs of samples with increasing residence time before air injection.

To further investigate it, nanowire growth was suppressed using a 100% H_2 atmosphere while the air was injected at the optimal point (22 cm). This resulted in small "frozen" particles resembling the nanowire tips. A comparison of the particle size distribution with that of nanowire tips (obtained at lower percentage of H_2 in the carrier gas) is presented in Figure 5.7 A. Although the distribution of the particles with passivated surface is slightly shifted to larger diameter, both present very similar sizes. Thus, we can assume that the composition of these particles would be similar to that of the catalyst before nucleation of the nanowire.

The WAXS pattern (Figure 5.7 B) shows similar Sn and SnO, but the AuSn alloy peaks (40.4 and 41.5°) are also resolved, suggesting lower amount of Sn (≈60 %), as described before in the alloying section.

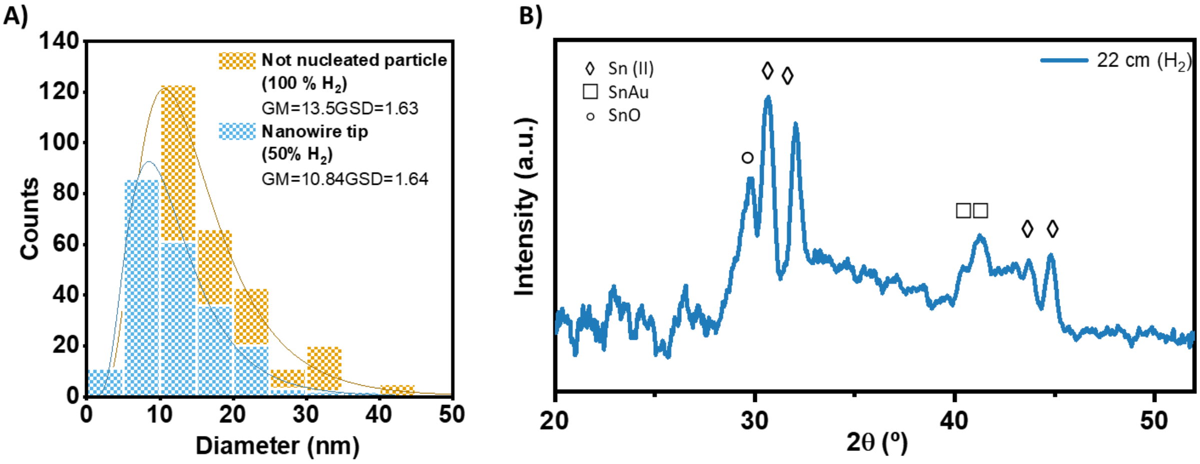

Figure 5.7 Size distribution comparison between inactive catalyst particles (orange) and those from which nanowires have grown (blue). Both produce with an air injection position of 22 cm.

The proposed growth initiation mechanism, then involves the formation of Sn-rich areas in the Au-Sn alloy. At low Sn atomic concentrations, both Sn and Au occupy part of the catalyst surface, creating small Sn-rich regions. These regions are believed to act as nucleation sites for unidirectional nanowire growth by enclosing the oxidation area.[45] However, as these regions expand at higher Sn atomic concentrations, the Sn species spread across the entire particle surface, making it susceptible to full oxidation and preventing further nanowire growth.

To gain further insights into the role of the Au/Sn ratio in the feeding once the nanowire growth was initiated, new experiments were conducted by systematically reducing the thermal evaporation power, thereby decreasing the concentration and diameter of Au particles. Subsequently, the temperature in the precursor vaporisation chamber was increased to enhance Sn availability. The air injection position was kept at 22 cm to determine if a higher Sn/Au concentration would lead to an increase in nanowire length.

The results shown in Figure 5.8 A, demonstrate a relationship between the Sn/Au ratio and the length of the nanowires. At low Sn/Au ratios, the catalyst was slightly enlarged and short nanowires were observed. Increasing the Sn/Au ratio promoted steady nanowire crystallisation, leading to longer nanowires. The sample with the longest nanowires, had a mean length of 257 ± 57 nm. However, increasing the Sn/Au ratio further induced homogeneous nucleation, compromising the final product purity.

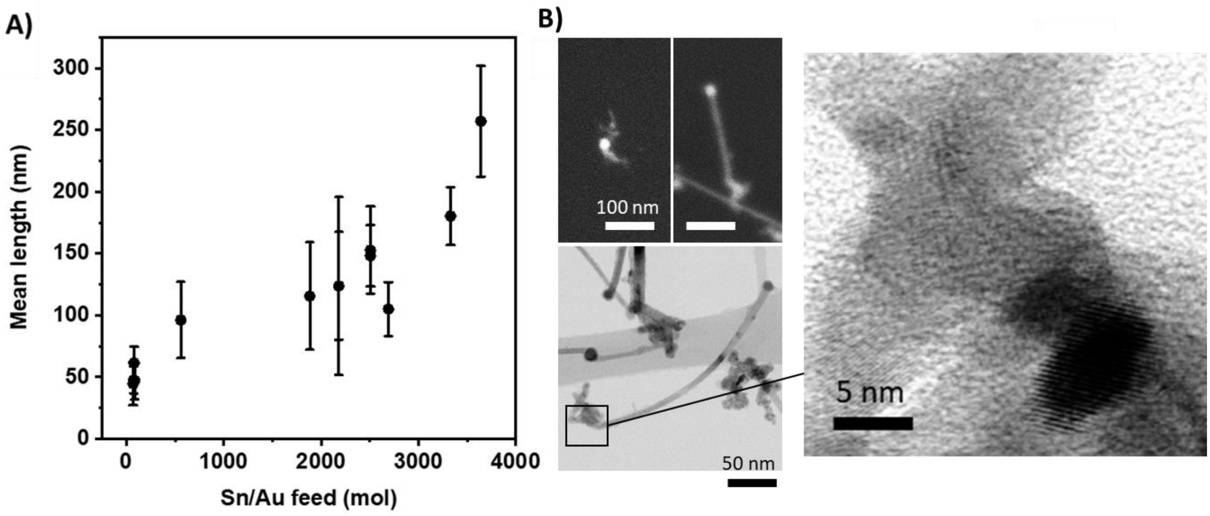

Figure 5.8 A) Nanowire length increase with Sn/Au feeding ratio. B) Polycrystalline initial nucleation present in nanowires of increasing length and HRTEM micrograph zoom showing their crystalline nature

Low concentrations of small Au catalysts allowed for the maintenance of a low precursor concentration, facilitating the achievement of the critical Sn concentration within the alloy particle without exceeding the threshold for homogeneous nucleation. Therefore, increasing reaction selectivity and NW length.

Interestingly, regardless of length, all nanowires exhibited a "tail" structure. HRTEM analysis confirmed this tail to be polycrystalline tin oxide. As shown in Figure 5.8 B, this tail appears to form during the initial stages of unidirectional growth. A similar phenomenon was observed in GaAs nanowires grown by aerotaxy.[128] This has been attributed to rapid initiation defects that occur before the growth finds the fast-growing direction. Muller et al.[35], in a study using another O-containing precursor ($[Sn(tBuO)_2]_2$) found similar inhomogeneous crystallisation at the catalyst/NW interface, attributing it to fluctuations in the "Sn−O(R)" flux during the decomposition-incorporation process.

To obtain the growth rate of the nanowires, we need to set a residence time as they grow inside a continuous flow; this is not an easy task. From what we know, nanowires do not start growing before air injection at the position of 22 cm, but the moment when they stop growing is unknown. As a reasonable estimate, we can take the middle part of the reactor, where the temperature profile starts to decrease. It would make 18 cm of nanowire growth. At a flow rate of 4 lpm, and considering the thermal volume expansion, it gives a time of 3.19 s and a growth rate of 80.5 nm/s.

This growth rate is at least 4 times faster than the values calculated from the times and lengths reported in SCVD.[125,129] However, it is significantly lower than expected for FCCVD, which has been proven to promote ultrafast growth (further discussed in Section 0). This suggests that the unusually low rate can be attributed to the growth of this specific material.

Bürger et al. already stated that high oxygen concentrations can hinder nanowire growth even after the growth process has been initiated.[45] In a more recent study[129], they reported that the length of their horizontally aligned nanowires reached a plateau after 8 min of synthesis due to the stabilisation of a high oxygen concentration. To address this issue, they employed pulsating oxygen injection, maintaining a transient state with oxygen concentrations consistently lower than the one in equilibrium, allowing a cyclic increase in length.

In our experimental setup, a section of the reactor chamber functions similarly to the transient state observed in Bürger experiments. This section lies between the air injection point and the area where the gas reaches a perfectly mixed state, creating an oxygen gradient that can promote nanowire growth. This suggests that the growth is confined to the brief mixing period, which occurs rapidly, especially at high temperatures.

There are two potential pathways for growth termination. In one scenario, growth occurs under low oxygen concentrations. A positive gradient in oxygen concentration along the catalyst path would lead to oxidation of the exposed catalyst surface, thereby terminating the growth process.

Alternatively, growth could occur in the region of locally high oxygen concentration, which later mixes with the hydrogen carrier gas, resulting in dilution. In this case, nanowire growth would be limited by the establishment of an equilibrium between oxide formation and reduction at the nanowire-catalyst interface, ultimately inhibiting further growth.

During the evolution of the reaction, reduction and oxidation processes occur. From the decomposition of the precursor (Equation 16 and 17) the system is supplied with Sn, SnO_2 and carbon-containing species. Therefore, at 700°C the reduction can be carbothermal[130] (Equation 20) or by hydrogen[131] (Equation 21):

$$SnO_x + xCO \rightarrow Sn + xCO_2 \qquad \text{Equation 20}$$

$$SnO_x + xH_2 \rightarrow Sn + xH_2O \qquad \text{Equation 21}$$

And the injection of Air promotes a competing oxidation process, from which nanowire (Equation 22) and catalyst encapsulation (Equation 23) results:

$$2Sn + O_2 \rightarrow 2SnO\ (s) \qquad \text{Equation 22}$$

$$AuSn + \frac{x}{2}O_2 \rightarrow \mathrm{Au} + SnO_x\ (s) \qquad \text{Equation 23}$$

Nanowire growth results only in those cases when the Sn oxidation reaction is favourable at the nanowire-catalyst interface but not on the exposed surface of the AuSn catalyst. A more detailed analysis of the role of oxygen needs to be performed to elucidate the termination of nanowire growth, especially considering reactivity and the importance of surface phenomena in nanoscale systems. A potential approach to control oxygen availability could involve the use of oxygen-containing gases with a breakdown temperature closer to the reaction temperature, such as N_2O. This would allow for a more gradual release of oxygen, potentially enabling better control over the oxidation process and prolonging nanowire growth.

These results highlight the complexity of the nucleation process, requiring further investigation of the catalyst thermodynamics to gain a full understanding. Moreover, they emphasise the delicate balance between oxygen exposure, alloy composition, and precursor concentration to achieve controlled nanowire growth. When this balance is not achieved, undesired products, such as particle surface oxidation, homogeneous nucleation, or suboptimal nanowire morphology, may result.

5.5. Selectivity control in the FCCVD synthesis of SnO nanowires

Up to here, the three main stages of SnO synthesis via FCCVD, namely, precursor decomposition, Sn incorporation to the catalyst, and nanowire growth, have been discussed with the aim of finding those conditions favouring nanowire formation. Based on the observations below, it is clear that achieving selectivity for metal oxide NW growth by FCCVD requires injection of the various gases at different points along the reactor to enable their sequential effects on the desired reaction path.

Regarding the carrier gas composition, there is a clear mismatch in the requirements for the different stages of the process. Precursor decomposition demands a 100% H_2 atmosphere to prevent the rapid formation of SnO_2 soot particles. However, the nucleation process requires a less reductive environment to enable oxide formation, as a fully reductive atmosphere would lead to catalyst passivation and hinder nanowire growth.

Thus, H_2 was used as the precursor carrier gas to facilitate its decomposition and was injected together with the catalyst into the reactor in a 100% H_2 atmosphere to allow further decomposition and alloying. The N_2 dilution inlet was located before the air injection point to allow nanowire formation.

Without this controlled environment, e.g. utilising solely hydrogen while suppressing the homogenous nucleation, nanowire nucleation would be inhibited. Conversely, a nitrogen-only environment would result in the formation of SnO_2 nanoparticles. Figure 5.9 illustrates the impact of differentiated process zones on product morphology at the same synthesis conditions but with different carrier gases.

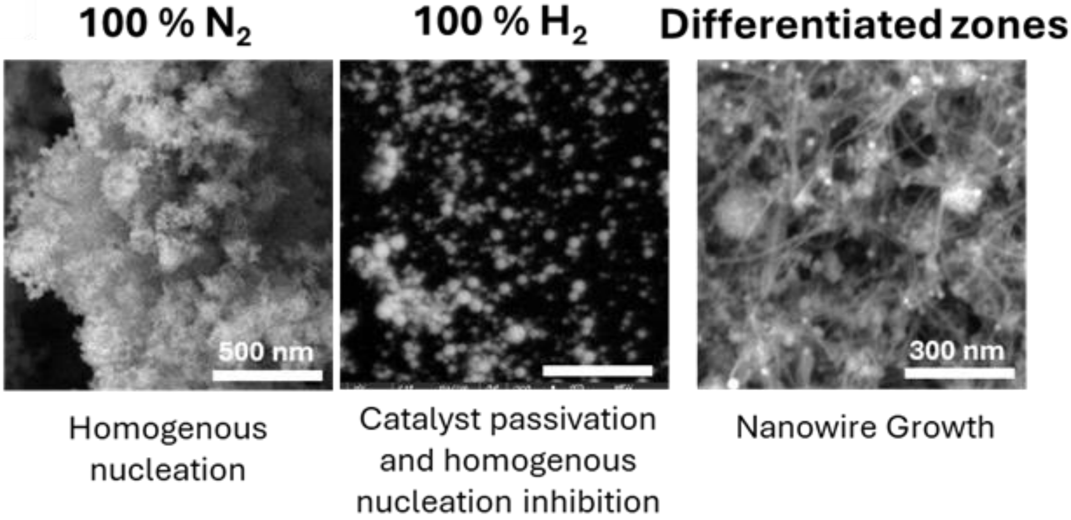

Figure 5.9 SEM micrographs of products obtained with and without differentiated zones.

Further exploration in the growth stage, including precursor, catalyst and oxygen concentrations, H_2/N_2 ratio, and temperature, revealed a complex interplay between nanowire growth, seed inactivation and nanoparticle formation.

Klamchuen et al.[132] proposed the concept of a "growth window," highlighting the critical balance between metal and oxygen concentrations for successful nanowire synthesis. In their SCVD experiments with laser ablation and low pressure (10 Pa), they found nanowire growth happens at concentrations sufficiently high to promote VLS nucleation but lower than that leading to VS nucleation (thin film formation). While our system differs in terms of process conditions, we identified a similarly narrow window.

The window for nanowire growth in our system was found to be strongly dependent on the Sn precursor concentration, with only concentrations between $4 - 8 \times 10^{-4}$ mol/m^3 resulting in nanowire formation. The high concentration end of the nanowire window, from which longer nanowires were grown, was achieved by increasing the H_2 concentration to minimise soot formation. Figure 5.10 A illustrates the percentage of solid products (estimated from SEM micrographs) at different Sn/H_2 molar percentages. It demonstrates a decrease in nanowire formation when homogenous nucleation starts to emerge.

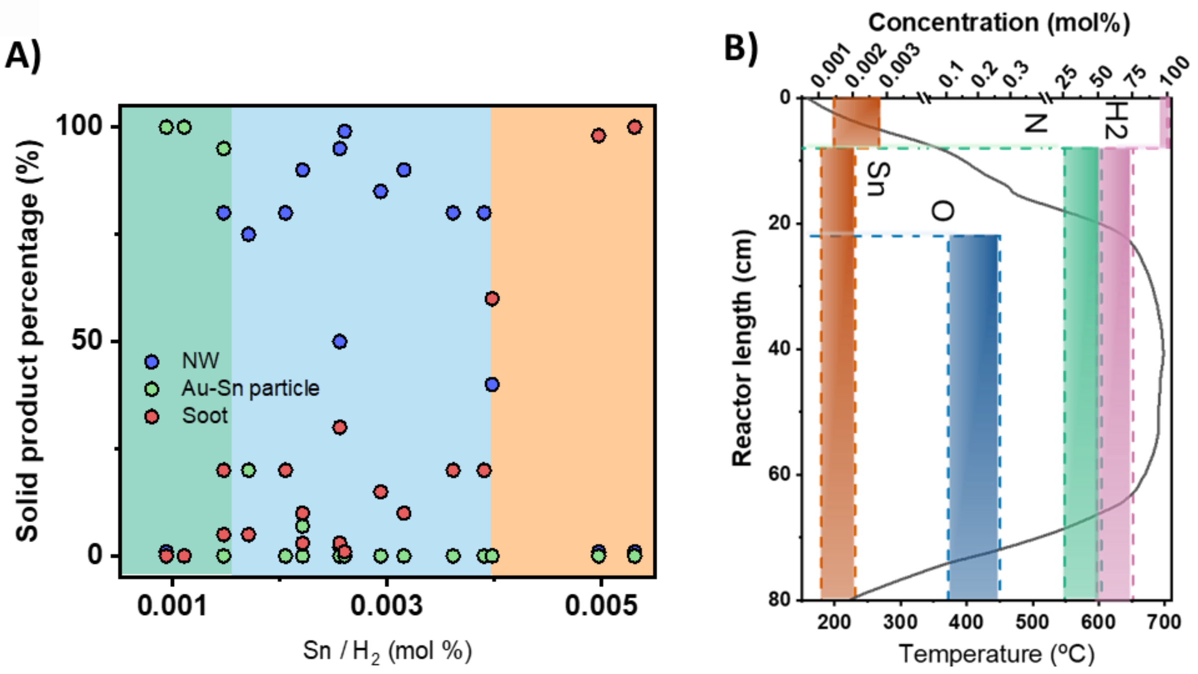

Figure 5.10 A) Effect of Sn/H2 molar percentage on product morphology. The blue region indicates the optimal range for nanowire growth, while regions outside this range result in increased homogeneous nucleation (orange) and catalyst passivation (green) B) molar concentration for high selectivity conditions

A study[133] following the presentation of the window concept, reported the influence of temperature, stating that the metal flux window becomes narrower and shifts toward higher metal concentrations as temperature increases. The same trend is expected for oxygen concentration. As a first approximation to observe the influence of temperature in the window in this work, experiments were conducted under the optimal synthesis conditions for 700 °C, with the temperature set 50 °C higher and lower to investigate the effects of temperature variation.

The growth window for SnO nanowires concerning Sn precursor concentration is narrow. Consequently, a temperature change of just 50 °C significantly influenced the morphology of the solid products (Figure 5.11). At 650 °C, soot was the predominant product, as the window shifted to lower Sn concentrations. The amount of Sn provided exceeded the threshold for homogeneous nucleation. Conversely, at 750 °C, the main product was passivated catalysts. These results resemble those obtained by varying the air injection position. In this case, while the injection position remains constant, the equivalent temperature changes. Although these results are not conclusive, they are indicative of the strong influence of the temperature on the growth mechanism and suggest the need to adapt the experimental setup to the changing window for further investigation.

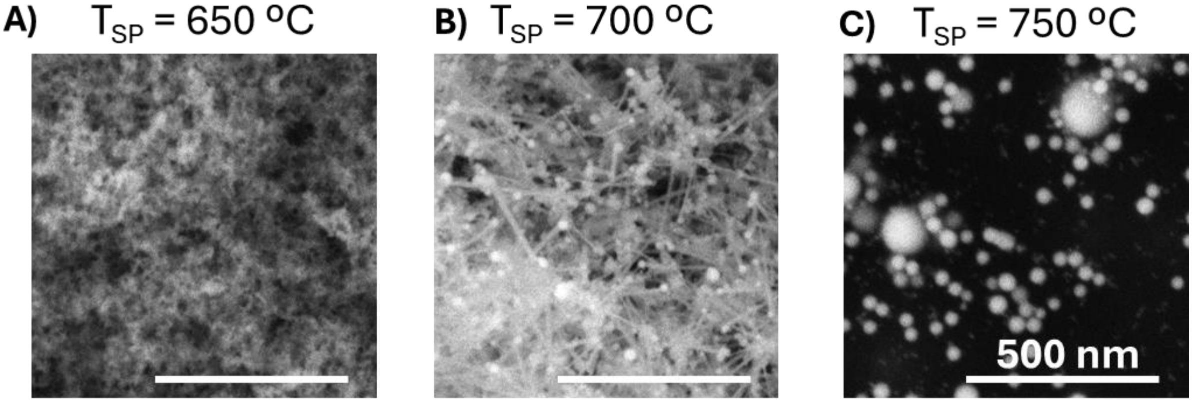

Figure 5.11 Effect of temperature on the product morphology (The same conditions were used except for temperature).

The experimental conditions optimised until the date of this thesis that led to the highest selectivity, and relatively long nanowires are presented here:

- The precursor was vaporised using pure hydrogen at 150 °C to ensure efficient transport without premature decomposition.
- A thermal evaporation power of 300 W (equivalent to 4.5 x 10^6 cm^{-3}, with a GM= 6.8 nm and GSD=1.6, measured before passing through the reactor) produced the desired Sn/Au ratio in the alloy particles. Excessive gold led to particle enlargement without nanowire growth, while lower power resulted in reduced selectivity by increasing soot formation.
- The dilution step was done with a nitrogen-rich (50-100%) flow after surpassing the Au-Sn eutectic point (280 °C).
- Air injection was implemented slightly before the reaction zone at 640 °C.
- The hot zone temperature was set to 700 °C

The molar concentration of each gas is plotted against the temperature profile in Figure 5.10 B. The profile denotes the three zones needed for nanowire growth. It is important to note that the molar concentrations of both oxygen and tin species within the reaction zone were extremely low. The use of dilute conditions to obtain high-quality materials is a common characteristic of FCCVD reactions. The common strategies to achieve selectivity in the synthesis of other materials using this technique and their implication are further discussed in Section 6.

As an estimate to calculate the nanowire conversion, the nanowire throughput can be estimated from the catalyst concentration (1.4 - 4.5 x 10^6 cm^{-3}, at 300 W) and the average nanowire volume. This yields a throughput of 0.03 - 0.1 mg/h, equal to a conversion of 0.1 - 0.3 % of the fed precursor into nanowires. The mass collected in the filter at standard conditions is around 0.6 mg/h. Given that the catalyst mass accounts for 30% of the nanowire weight, the mass of the soot and microparticles (further discussed in the following paragraphs) in a sample can comprise 70-90 % of the total mass. With a maximum of 3% of the fed precursor converting into a solid product.

Up until now, the discussion has focused on solid products produced by the interaction of catalyst and Sn vapour. Nevertheless, as mentioned in Section 4.2, the formation of microspheres during the nebulisation process is a parallel competing reaction that lowers the effective precursor availability.

While the formation of microspheres represents a significant byproduct of the atomisation process, their impact on the experimental results presented in this Chapter is considered minimal. Notably, the morphology of these microparticles remains relatively unaffected by varying process conditions, while the nanosized product is significantly influenced, as shown in Figure 5.12 A, B.

Their composition at nanowire synthesis conditions is, as expected[120], a mixture of SnO_2, SnO and metallic Sn, as shown in the WAXS spectra in Figure 5.12 C. Although they could contribute to the oxidation-reduction reaction occurring in the continuous flow of the reactor and to the liberation of reactant species. Their contribution is taken as negligible.

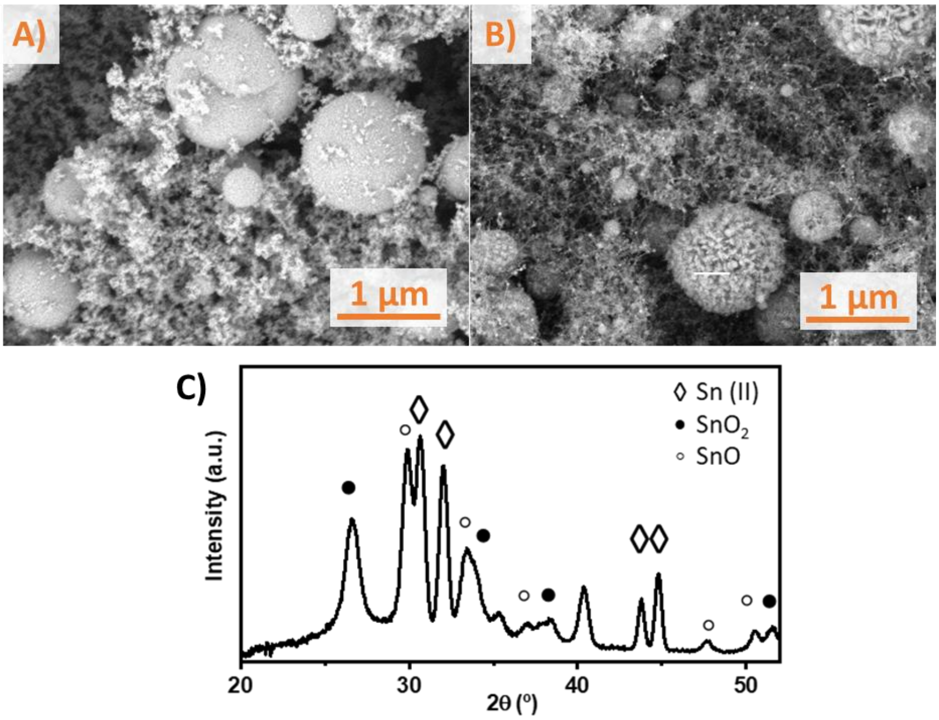

Figure 5.12 a) Sample taken at high oxygen concentration to enhance soot formation B) Sample taken at optimal conditions for nanowire growth. The microspheres only presented surface effects from the reductive environment. C) WAXS pattern of the isolated microspheres formed during nanowire synthesis.

5.6. SnO nanowires characterisation

Nanowires are collected continuously on PES or PC filters for as long as 6 hours, Figure 5.13 A, B, and C show images at different magnifications of a typical sample containing 4 mg of material; the samples show zones with high selectivity toward nanowires and others with higher soot content.

More than 200 nanowires obtained at optimised synthesis conditions were examined in SEM to obtain the length and diameter distribution. They have a mean diameter (Figure 5.13 D) of 8 ± 2 nm and a lognormal distribution with GSD = 1.46. Their length (Figure 5.13 F) ranges in a few hundred nanometres, with a mean of 257 ± 57 nm; the length also exhibits a lognormal distribution, similar to the result obtained of the ultra-long SiC nanowires.

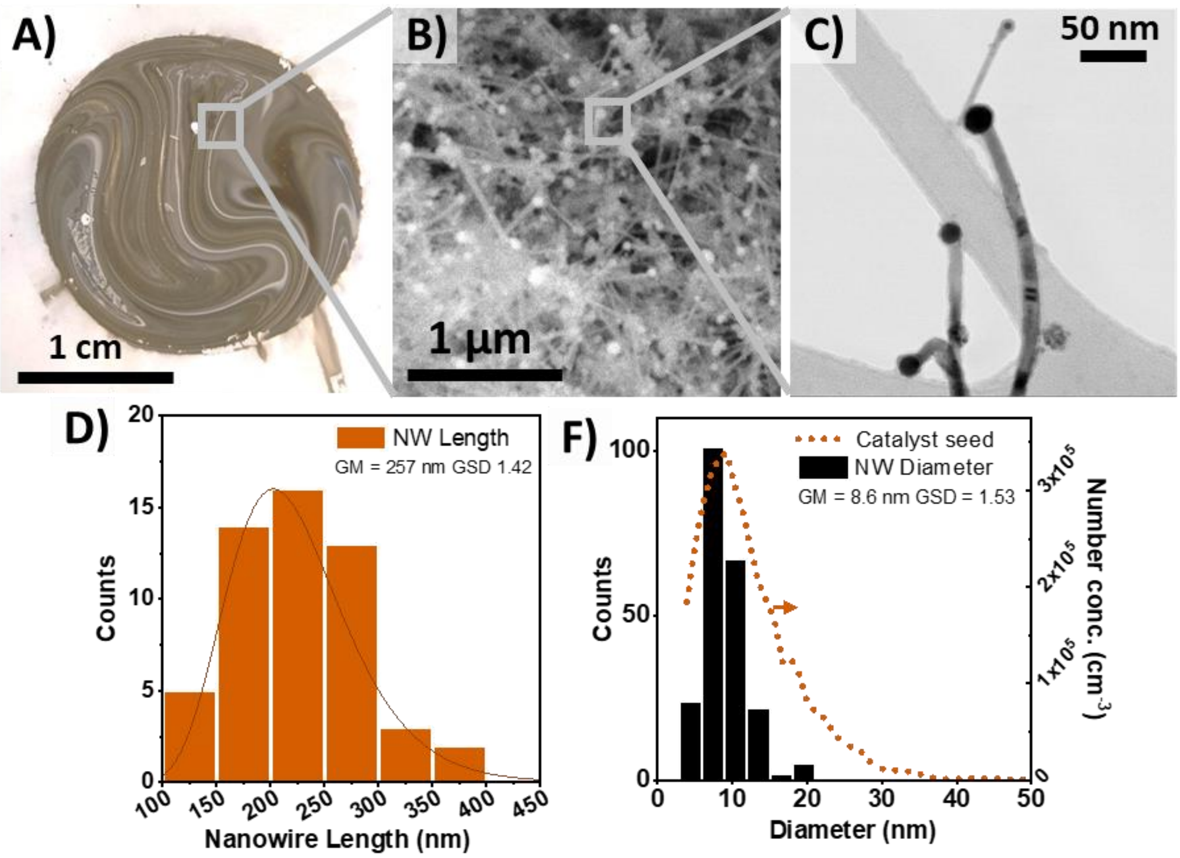

Figure 5.13 SnO nanowires via FCCVD A) typical sample obtained by simple filtration. B) SEM and C) TEM micrographs of SnO nanowires. D) Length and F) Diameter lognormal distributions.

The tip is slightly larger in diameter than the stem. Interestingly, the catalyst seed size and the nanowire coincide, suggesting that the increased size of the catalyst is due to the Sn intake. (Figure 5.13 C). In the case of samples obtained at higher H_2 concentrations (75 %), the tip diameter is even larger, and the nanowires present a needle shape with larger diameters near the catalyst. Suggesting the increase in diameter is due to an increase in the catalyst size.

The root diameter (opposite to the catalyst) shows the same diameter as the nanowires grown in a 50 % H_2 atmosphere, which suggests that at the beginning of the growth, the catalyst composition was the same, but as the catalyst travelled in the reactor, the catalyst accumulated more Sn, probably due to slower oxidation in the more reductive atmosphere. This coincides with the aforementioned inhibition of nanowire growth in a 100 % H_2 atmosphere. And with the hypothesis that nanowire growth terminates when the system reaches an equilibrium between oxidation and reduction after air injection.

The composition of the nanowires was confirmed with EDX (Figure 5.14 A) while the stem shows tin and oxygen content, the catalyst shows high tin and gold content and a shell of oxide. No significant difference was found between samples grown in different H_2 concentrations.

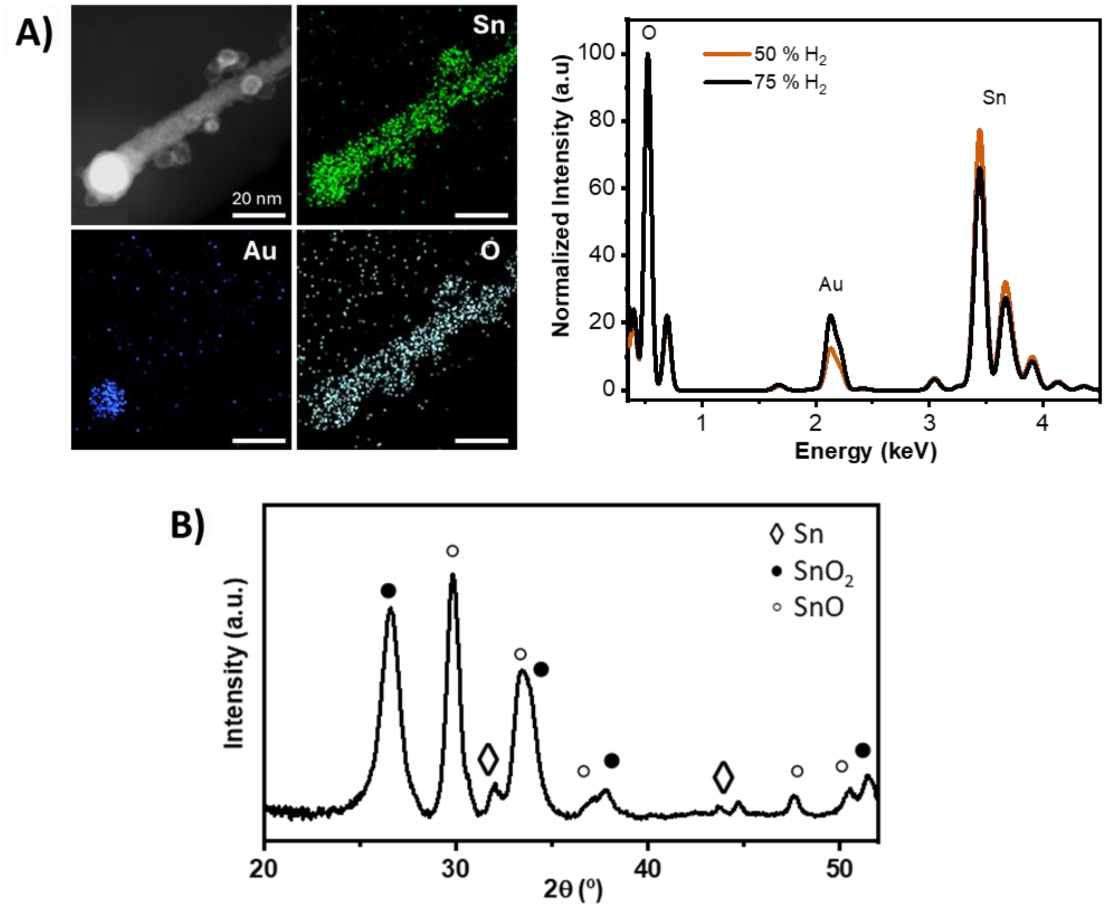

Figure 5.14 A) EDX map and spectra of a SnO nanowire. B) WAXS pattern of a sample consisting of nanowires and soot nanoparticles.

Nanowires were inspected by HRTEM (Figure 5.15), they present high crystallinity with rough edges. The interplanar spacing of 0.305 nm coincides with the tetragonal phase of SnO. The SAED patterns give a planar spacing of 0.27, 0.30 and 0.24 nm; they coincide with the tetragonal phase of SnO.[134]

Up to date, SnO_2 has been reported as the product of SCVD in inert atmosphere. Only Jeong et al.[135] reported the synthesis of both SnO_2 and SnO in their synthesis process using 4% of H_2 in Ar. They attribute the coexistence of SnO and SnO_2 NWs to complicated interactions between H, Sn, and O vapours. In this work, with higher H_2 concentration (50-75%), only a few nanowires were inspected (5), but all coincide with the tetragonal SnO phase. Which was confirmed with the predominant phase found through the WAXS pattern (Figure 5.14 B) in the bulk analysis, presenting stronger peaks at 29.7 and 33.2°.[136] SnO_2 signal corresponds to the soot nanoparticles in the sample.

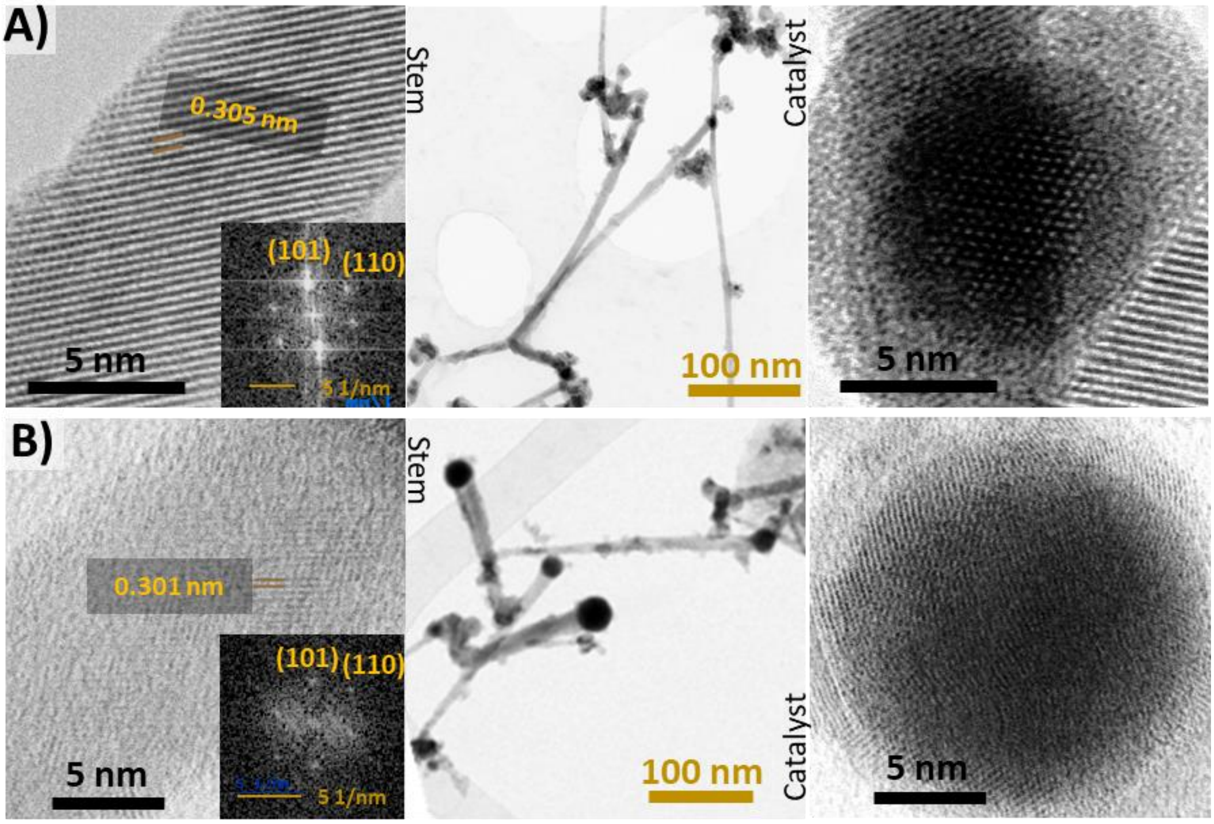

Figure 5.15 HRTEM images of SnO nanowires grown in a) 50 % and B) 75 % H_2 atmosphere. A magnification of the stem and its FFT for both are presented on the left. They show interplanar spaces corresponding to tetragonal SnO. On the right, the catalyst magnifications.

The ex-situ analysis of the catalyst composition can provide more information about the final stages of nanowire growth. Jeong et al.[135] observed an Au-rich core, while the shell was composed of AuSn alloy. A similar observation in our catalyst particle, with a thick SnO_x layer and an Au-rich core, would indicate that growth was terminated due to oxidation of the catalyst surface, deactivating its catalytic properties. While an intermetallic core rich in Sn would suggest the termination of growth due to an imbalance in the oxidation-reduction reaction, even if a thin oxide is later formed due to exposure to air. As illustrated in Figure 5.15, some lattice fringes are visible in HRTEM images of the catalyst particles, suggesting the core-shell configuration. However, precisely identifying phases in a complex mixture requires an extended elemental analysis with higher resolution.[137] Future studies will focus on this aspect.

5.7. Self-standing sheets of SnO nanowires

The maximum aspect ratio achieved for the tin oxide nanowires was 52. Despite the high selectivity towards nanowire growth, the relatively short lengths prevented the formation of self-standing samples. To favour agglomeration, the nanowire length and the volumetric concentration should increase. Both strategies are hindered by the requirement for dilute conditions to suppress homogeneous nucleation, with added difficulty due to the presence of the micro-spheres produced from the injection system.

Self-standing SnO_x sheets were instead fabricated (Figure 5.16) by simple wet processing to separate the microspheres from the nanowires. Following the preparation method designed by David Tilve: 4 mg of a collected sample was dispersed in a CTAB aqueous solution (1 mM). Positively charged surfactant has been used to obtain stable suspensions of metal oxide nanowires.[138,139] The dispersion was then mildly centrifugated at 1500 rpm for 10 min to precipitate the microspheres of high weight. Then, the supernatant was filtered using a Track-Etched polycarbonate filter with a vacuum. To separate the membrane from the filter, the latter was dissolved in N-methyl-2-pyrrolidone (NMP).

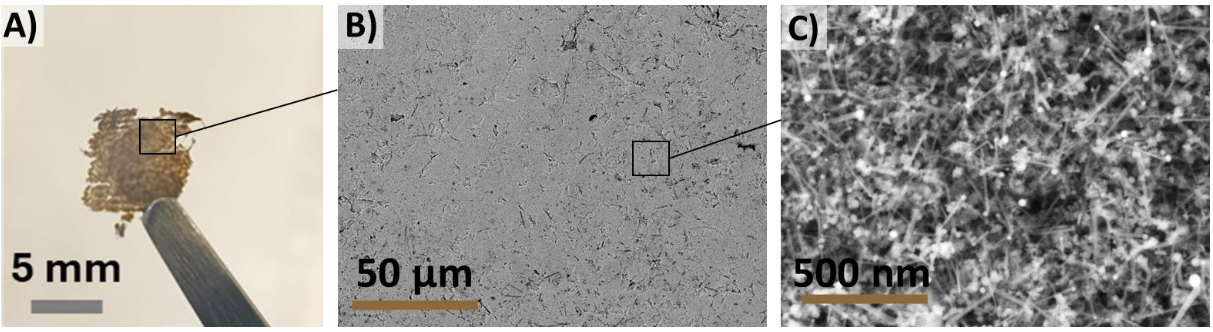

Figure 5.16 Digital picture and B-C) SEM micrographs of the self-standing nanowires sheet at different magnifications

The result is a self-standing sample composed of SnO nanowires and SnO_2 soot particles (Figure 5.16 C). To our knowledge, this is the first example of a freestanding material made of SnO NWs, and one of the few examples of MO_x nanowire network macromaterials reported.[140,141]

This format facilitates their use as high-capacity anodes for energy storage devices, namely, lithium or sodium ion batteries, with theoretical capacities of 875 and 1150 $mAhg^{-1}$, respectively[142]. Tetragonal SnO possesses a large interlayer spacing of 4.84 Å, which offers rapid ion diffusion pathways for Na^+ and Li^+ ions, while accommodating the large volume expansion during the alloying process.[143] In addition, the nanowires in the sample can provide mechanical stability avoiding the use of binders. Work is in progress to perform electrochemical tests on SnO NW electrodes.

Summary of Chapter 5:

This chapter presented the synthesis of tin oxide (SnO) nanowires via FCCVD. The resulting nanowires exhibited a tetragonal SnO crystalline structure, mean diameter of 8 nm and mean lengths of up to 257 nm. Tin(II) 2-ethylhexanoate ($Sn(oct)_2$) was employed as the tin precursor and gold as the catalyst. The in-house FCCVD reactor was adapted to facilitate the study of the three key stages of SnO nanowire growth: precursor decomposition, Au-Sn alloying, and oxidation-mediated growth.

Firstly, It was observed that, under standard conditions, the precursor tends to decompose into SnO_2 soot particles. However, in a highly reductive atmosphere (100% hydrogen), the formation of tin vapour (Sn) is promoted, which is critical for the growth of nanowires.

Then, the alloying process was investigated by maintaining the reductive atmosphere while introducing gold into the reaction chamber. The incorporation of tin into the gold catalyst particles was monitored by observing their increase in volume. The efficiency of tin incorporation into the Au-Sn alloy was found to be relatively low (2%), indicating that a significant portion of the tin remains available for either nanowire growth or soot formation.

To study the nucleation and growth of the nanowires, the reductive atmosphere was diluted with N_2 and oxygen-containing air was selectively introduced at specific points within the reactor. The optimum injection point was identified for nanowire growth, strongly influenced by the Sn/Au ratio within the catalyst particles during oxygen exposure. Excessive Sn incorporation led to the formation of core-shell particles instead of nanowires.

A systematic exploration of various parameters, including precursor and catalyst concentration, gas composition and temperature, led to the identification of optimal conditions for nanowire synthesis. Within this window, soot formation was minimised, and the nanowire length was maximised. Given their short aspect ratio and low volume concentration, a simple wet-processing method was used to produce a self-standing sheet from the nanowires, aimed at potential applications as an electrode material for energy storage devices.

6. Common features found in FCCVD 1D growth.

The results presented above summarise the contributions of this thesis in expanding the library of NWs produced by FCCVD through improved reactor designs and a better understanding of the factors controlling reaction selectivity in FCCVD.

Indirectly, this work has also produced new data related to other fundamental questions in FCCVD and NW growth in the incorporation-limited regime. This chapter presents a general view of NW growth by comparing the literature data with the new results discussed above.

6.1. Ultrafast growth

A common feature of all materials grown by FCCVD is their considerably faster growth rate compared to SCVD, leading to the formation of 1D nanoparticles with high aspect ratios in very short times. Growth rates in FCCVD can be 10 to 1000 times faster than those observed in SCVD.

Figure 6.1 A presents a comparison of reported growth rates for nanowires of GaAs, Si, SiC, and SnO, as well as nanotubes of C and BN. For this comparison, we have calculated the nanowire length increase per total growth time in SCVD, assuming a constant growth rate. Additionally, we have only included studies conducted near atmospheric pressure to ensure comparability with FCCVD experiments using the floating catalyst method.

Given the fast nature of the FCCVD process, determining an accurate average growth time can be challenging. Using the residence time of a catalyst particle throughout the entire reaction tube may overestimate the growth time. Only a few studies[65], including the one presented here for SiC nanowires, have attempted to estimate the growth time by identifying the specific region in flow reactors where nanowires/nanotubes are formed. Even if these estimates are associated with significant uncertainty, they represent a valuable step towards understanding the time scale of the FCCVD process.

The two growth modes, FCCVD and SCVD, operate in distinct regimes. Overall, SCVD is considered to be limited by the diffusion of precursors and/or adatoms to the catalyst. In contrast, FCCVD, lacking a substrate and occurring at higher pressure, is not subject to these diffusion limitations.

In the FCCVD synthesis of VGCFs and CNTs, the rapid growth was previously attributed to the presence of sulfur[144] and to the higher reaction temperatures used in FCCVD, which could influence reaction kinetics or alter the catalyst state from solid to liquid.[145] However, data for nanowire growth demonstrate faster rates at equal reaction temperature and pressure, even without suspected changes in solidification from the eutectic.

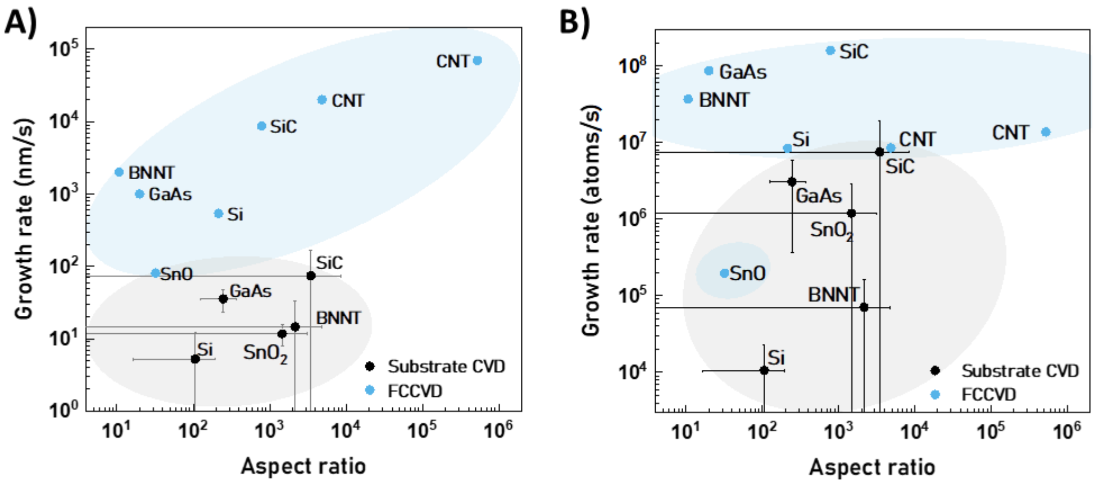

Figure 6.1 Growth rate and aspect ratio of 1D nanoparticles of Si[146], GaAs[147,148], BNNT[149–154], SiC[84,85,155–157] and SnO_2[125,129] grown by substrate CVD (black) and Si[9], GaAs[19], BNNT[158, 7], CNTs[159, 70], SiC and SnO grown by FCCVD (blue). Note the growth rate axis units: (A) nm s−1 and (B) atoms per second.

Similarly, early work proposed that FCCVD prevents the formation of a “depletion layer” by eliminating the substrate.[13] In SCVD, the local concentration near the substrate and catalyst is progressively reduced during nanowire growth, due to a higher concentration of by-products near the catalyst and a longer diffusion path. This mechanism would apply to root growth, where the catalyst stays attached to the substrate, but less so for tip growth, which is also common for all materials here compared.

Figure 6.1 B presents a similar comparison of growth rates, but this time in number of atoms per second. It suggests that in FCCVD, the limiting process is the rate of crystal step growth, as indicated by the relatively narrow band of growth rates when calculated in atoms per second. That is, the solidification process is related to the incorporation of atoms into the catalyst and not their diffusion into it.

Hence, the main difference between FCCVD and SCVD is expected to be the different rates at which the precursor species impinge on the catalyst. In SCVD, the catalyst concentration and temperature are constant, so the impingement rate is governed by precursor availability, which is also constant under equilibrium in the reactor. In FCCVD, the temperature, catalyst distribution and precursor concentrations are expected to evolve. The impingement rate would be the collision rate between the flowing species.

For comparison purposes, Miguel Vazquez-Pufleau calculated the average catalyst-precursor species separation using Montecarlo simulations. For that, he assumed typical concentrations for both processes: 10^8 particles/cm^3 for FCCVD and 82 particles/μm^2 in the bottom surface of a 1 cm^3 cube for SCVD. All particles were set with a diameter of 32 nm.

The predicted distance distribution of two randomly positioned particles is about 3 orders of magnitude smaller in the FCCVD case than in the SCVD case, indicating higher probabilities of collision. In addition, without spatial constraints, precursor species can impinge from any direction, leading to the high incorporation rate which translates to better precursor utilisation and fast growth limited by crystal formation.

Compared to other materials grown by FCCVD, the SnO nanowires described here exhibit a significantly slower growth rate. Given that all other materials demonstrate rapid growth regardless of the specific 1D crystal structure or catalyst composition, it is reasonable to extend this feature to SnO as the key feature (high partial pressure and availability of the precursor) of FCCVD is also present. Then, the difference in growth rate must be related to still not optimal growth conditions along the catalyst path. Then, the effective growth rate should be calculated using the residence time in those conditions that favour nanowire growth, which is probably lower than the approximation of 3 s in Chapter 5.

In SCVD, SnO and SnO_2 nanowires grow longer over extended time periods, which is consistent with the diffusion-limited regime. However, the SnO growth presented here, occurs over a short time before being hindered by factors such as the formation of an oxide layer or the establishment of a reduction-oxidation equilibrium, which may be limiting further growth.

6.2. Size distribution and catalyst usage

To control nanowire size, several factors are influenced by the catalyst size and interaction with the precursor species, including the percentage of the catalyst aerosol involved in 1D nanoparticle growth, the relationship between the catalyst seed and nanowire diameter, and variations in nanowire shape related to catalyst size.

In the growth of nanowires by FCCVD, a notable observation is that under successful conditions, all the catalyst that travels through the flow reactor forms nanowires. This phenomenon is generally observed for the growth of 1D nanoparticles of Si, SiC, and SnO.

In contrast, the growth of CNTs by FCCVD typically results in a large fraction of the catalyst remaining as residual particles attached to the nanotubes. Analysis of CNT dimensions and the mass fraction of carbon and iron suggests that only a small percentage (approximately 0.05 at%) of Fe nanoparticles produce CNTs.[70] Ex-situ analysis often reveals that most of the residual catalyst corresponds to metallic nanoparticles encapsulated with a graphitic shell.

Therefore, for nanowires, there is a strong correlation between nanowire diameter and the size distribution of the catalyst aerosol, as illustrated in Figure 6.2 B-D for Si, SiC, and SnO. This correlation is valid for in situ decomposition of catalyst precursors, such as ferrocene in the synthesis of SiCNW, as well as ex-situ generated aerosols from evaporation or spark discharge.

Conversely, while the outer diameter of CNTs is typically similar to the size of their catalyst particles, only the smaller end of the size distribution successfully forms nanotubes. As shown in Figure 6.2 A, the diameter distribution of CNTs represents only a small fraction of the catalyst aerosol, and even smaller for single-walled CNTs. To address this, CNT growth often involves forming the catalyst in situ, enabling the precursor to interact with smaller catalyst particles during the growth process, at a less stable stage in the evolution of the aerosol.

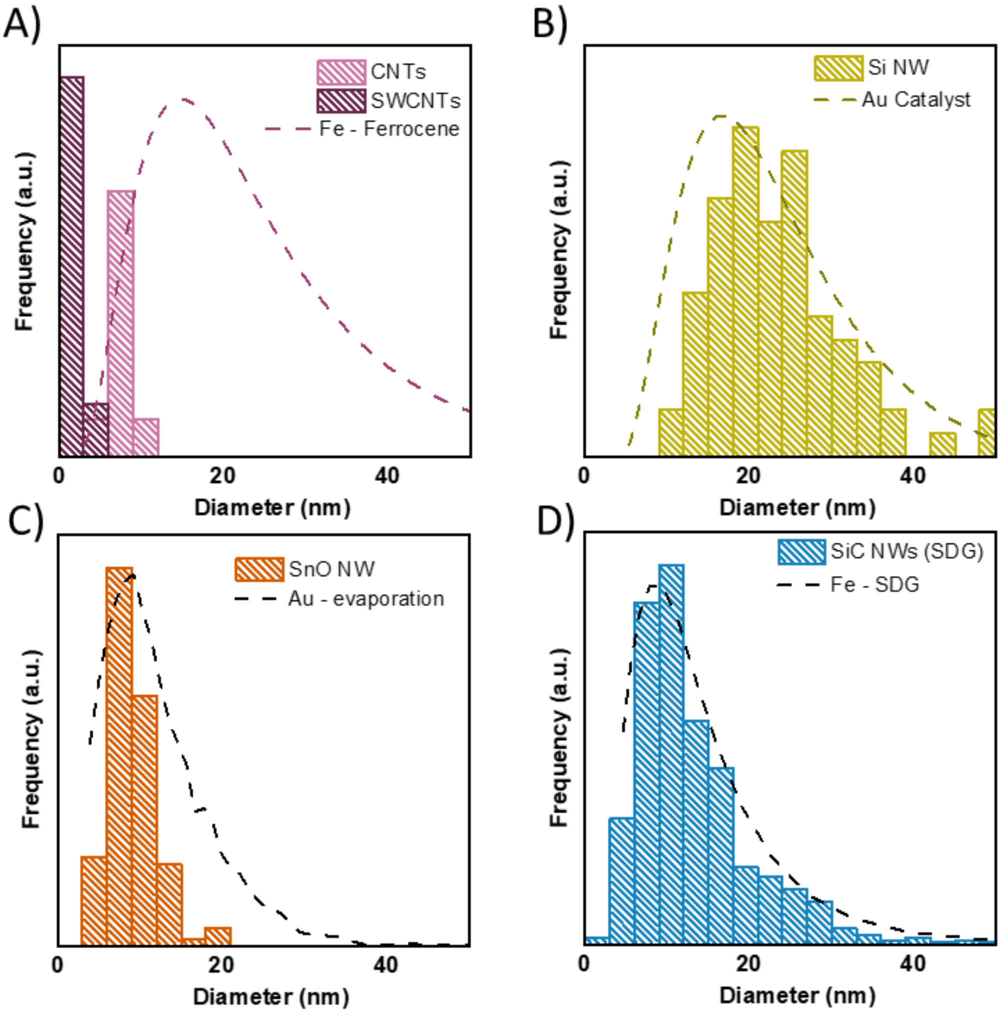

Figure 6.2 Comparison of catalyst size and nanowire/nanotube diameter distributions. A) CNT,[70] and SWCNTs[71] produced by FCCVD from ferrocene decomposition B) Si NW[27] and C) SnO NW grown from Au aerosol via thermal evaporation, D) SiC nanowires produced using spark discharge Fe aerosol

Regardless of catalyst usage, all 1D nanoparticle diameter distributions are log-normal, with geometric standard deviation > 1.36, as summarised in Table 6.1, which follows the expectation for an aerosol of metallic catalyst particles.[100]

Furthermore, there are mechanistic differences between monoelemental and bielemental nanowire growth. In the case of SiNWs, a monoelemental system, the nanowire diameter is directly related to the size of the Au tip, with Si crystals nucleating after the tip reaches saturation. In contrast, for bielemental systems like SiC and SnO nanowires, the formation depends on the introduction of nucleation agents (C, O), causing variations in tip size depending on the percentage of incorporation before nucleation. For example, in SnO nanowires, the tip is larger than in SiC due to a higher solubility of Sn in the Au catalyst. SnO does not reach saturation, whereas SiC exhibits a supersaturation limit that controls the alloy tip size.

Diameter uniformity also varies across different nanowires. For example, SnO nanowires increase in diameter during growth as more Sn is incorporated. Conversely, GaAs nanowires, which use metallic gallium as a seed, show a decrease in diameter as the growth process consumes the seed.[160] SiC nanowires, on the other hand, remain in a supersaturated state, resulting in more uniform diameters throughout growth.

Table 6.1 Mean diameter and geometric standard deviation (GSD) of log–normal distributions of 1D nanoparticles produced by FCCVD

1D nanoparticle	Mean diameter (nm)	Geometric standard deviation (GSD)
Si NW	20–25	1.33–1.41
GaAs NW	65	
SiC NW	17–45	1.43–1.78
CNTs	1.9–7.1	1.21–1.36
BNNT	2.0	
SnO	8	1.53

6.3. Selectivity and conversion in FCCVD

The objective of this thesis is to demonstrate the viability of FCCVD for synthesising a broader range of materials. Additionally, it aims to show that a deeper understanding of the process enables faster adaptation to new systems, allowing researchers to experimentally achieve the conditions necessary for nanowire growth more efficiently.

Each system presents unique challenges due to competing reactions and interactions between catalyst and precursor species. For instance, in SiC synthesis, the primary issue affecting selectivity is the formation of carbon and SiC soot, which makes it impossible to isolate nanowires through filtration alone. Alternative collection methods were needed to extract the nanowires as they grew. Similarly, SnO also suffers from soot formation at high precursor concentrations, catalyst deactivation, and competing oxidation-reduction reactions. In GaAs synthesis, high V-group precursor concentrations result in increased soot particle production[8] and parasitic growth on the nanowire surface increases with excess of dopant precursors (Sn, Zn).[128,161] For CNTs and BNNTs, the main challenge is the deactivation of the catalyst, even when conditions are optimal for nanotube growth, due to competing catalysed reactions.

summarises experimental conditions found for FCCVD synthesis to reach conditions favouring 1D nanoparticle formation, it details the by-products formed along the reactor tube and compares precursor, catalyst and H2 concentrations. summarises experimental conditions found for FCCVD synthesis to reach conditions favouring 1D nanoparticle formation, it details the by-products formed along the reactor tube and compares precursor, catalyst and H_2 concentrations.

Table 6.2 Updated synthesis conditions for FCCVD-grown materials.

1D nanoparticle	***Precursor concentration (% mol)***	***H_2 in carrier gas Vol %***	***Approximate selectivity[a]***	***Catalyst concentration (cm^{-3})***	***Approximate Conversion[b] (%wt)***	***Solid by-products of reaction***
SiC	2 %	100 %	< 10 %	10^7 - 10^8	-	SiC nanoparticles C soot Si particles
SnO	0.001 %	50-75 %	75%	10^6	0.1 -0.3 %	Core-shell particle SnO_2 nanoparticles
Si[64]	1.0-3.0 %	30-70%	55-95%	10^7	0.1 - 0.6 %	Si nanoparticles
CNT[55,162,163]	0.0035 %	100 %	86 %	10^6 - 10^9	0.1 - 10 % (5%)	C soot Covered catalyst
BNNT[7]	0.067 %	63 % (NH_3)	-	10^6		BN Nanofibers Covered catalyst
GaAs[19]	0.0003 % AsH_3 0.00033 % TMGa	0 %	-	10^6	-	GaAs nanoparticles Radial deposition

[a]1D nanoparticles mass / total solid mass [b]Solid product mass / precursor mass

Despite these differences, all 1D nanoparticles produced using FCCVD, including SnO and SiC nanowires, required highly dilute precursor concentrations (10^{-4} to 3 %mol) to achieve reasonable selectivity. Moreover, the presence of H_2 or a reducing atmosphere has been crucial in shifting the equilibrium towards catalyst-driven growth rather than competing reactions such as homogeneous nucleation. Lower temperatures have also been shown to favour the formation of catalysed 1D nanoparticles.

Furthermore, flow patterns play a significant role in determining zones of high or low selectivity. For instance, if catalyst particles are located at the centre of the reactor and the precursor is injected at a different radial position, a gradient of concentrations will form. In regions with locally high precursor concentrations, soot is likely to form, while 1D nanoparticles are more likely to form within the path of the catalyst.

Additional to the low precursor concentration, the reaction conversion is also in fractional molar percentages. Which significantly limits the efficiency of the process. Only extensive research in the production of CNTs led to conversions close to 10 %.[59] For instance, by testing different hydrocarbon sources and carrier gas types.

Another possible route to increase throughput, is by optimizing the concentration of catalyst particles responsible for nanowire growth. With typical residence times of 1-60 seconds in FCCVD, the catalyst aerosol has a concentration limit of approximately 10^8-10^9 cm^{-3}.[25] Currently used catalyst concentrations in FCCVD growth are significantly lower. This suggests significant room for improvement by increasing catalyst concentrations in FCCVD.

6.4. Self-assembly of floating 1D nanoparticles

One of the defining features of FCCVD is the direct assembly of 1D nanoparticles into macroscopic structures. To achieve this, the system must transition from an aerosol, meaning a suspension of 1D nanoparticles in the gas phase, to agglomerates that progressively collide and coalesce, ultimately forming a continuous network within the reactor tube, a process known as gelation. The outcome is a 1D nanoparticle aerogel, e.g. a percolated network of 1D nanoparticles with an extremely low mass fraction or bulk density ($\rho_{aerogel}/\rho_{1D\ Nanoparticle} < 0.01$), which is mechanically stable against the stresses generated from the flow and collection.

Aerogel formation is central to the synthesis of CNTs, where continuous CNT fibres can be spun directly from the reactor by withdrawing the aerogel as it is continually regenerated.[6] This phenomenon has been also observed in the growth of BNNTs at high particle concentrations through inductively coupled plasma synthesis and laser ablation.[16,164]

Similarly, as discussed in Chapter 3, an aerogel of SiC nanowires is formed due to an increase in nanowire concentration around a collecting rod, aided by thermophoretic deposition. Nevertheless, in the case of SnO nanowires and Si NW, the reaction shows predominance of a nanowire aerosol, with no indication of an aerogel in the reaction tube.

The study of Abomailek et al. on Si nanowire aggregation[103] suggests that the formation of an aerogel inside the reactor does not arise from individual floating nanowires, but rather from aggregates of nanowires that collide and combine into larger macrostructures. In line with such study, in the synthesis of SiC and SnO nanowires evidence was found of agglomerates collected by filtering the gas stream. Figure 6.3 A and B show SnO agglomerates composed by mainly nanowires, larger agglomerates were found at synthesis conditions of higher selectivity. Panels C and D, evidence the same behaviour in the synthesis of high-aspect ratio SiC nanowires. These agglomerates are likely formed under local conditions where the catalyst concentration is higher; nevertheless, they represent important evidence that nanowires aggregate as they travel through the reactor tube.

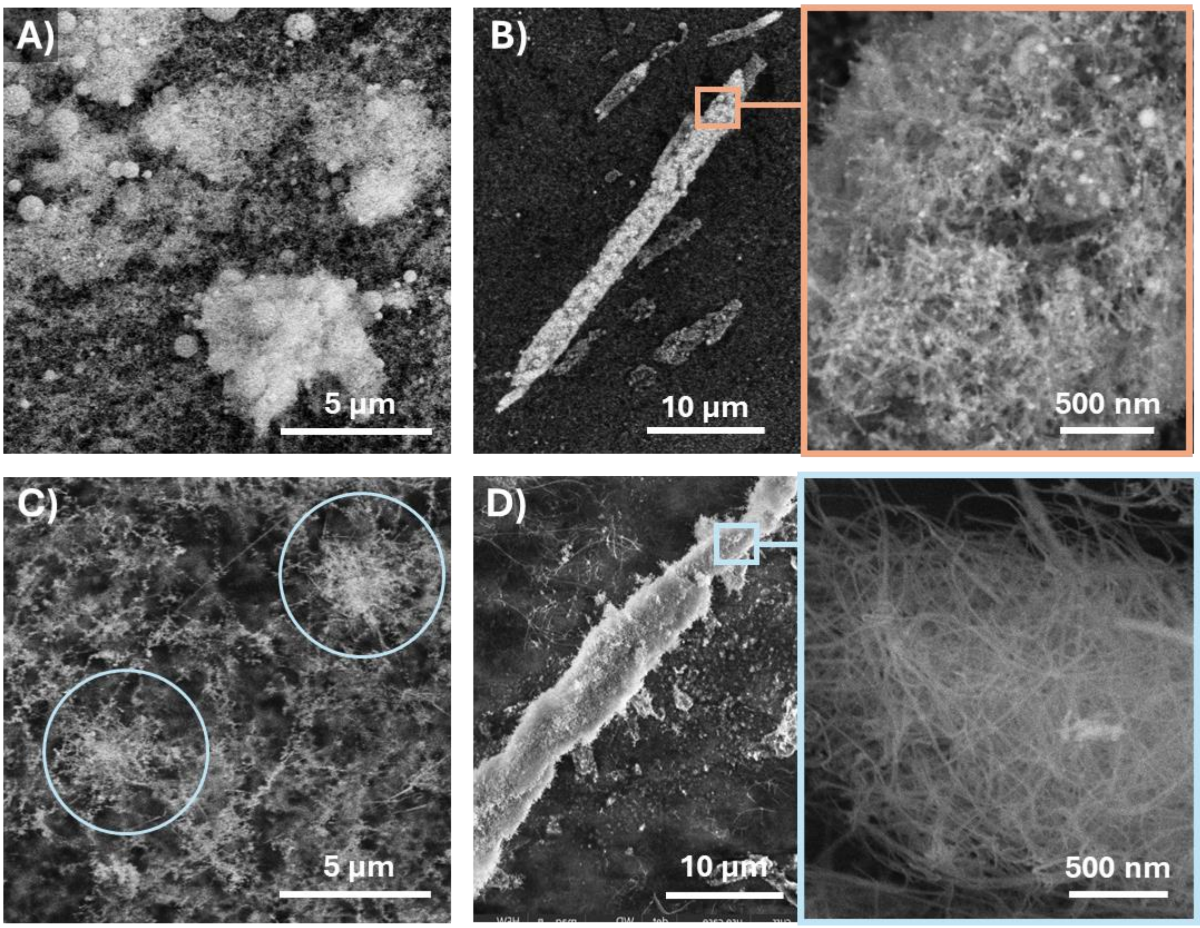

Figure 6.3 Agglomerates of SnO nanowires (top panels) and SiC nanowires (bottom panels). A and C) small agglomerates of a few nanowires. B and D) Larger agglomerates with cylindric shape. Similar behaviour was found in SnO and SiC nanowires synthesis despite their difference in aspect ratio.

To understand the parameters that determine whether the system will result in an aerogel or an aerosol of agglomerates, an adapted percolation model was developed based on experimental data on Si nanowires agglomerates (similar to those in Figure 6.3 A and C) and simulations with a Brownian collision algorithm to form agglomerate models.[103]

The proposed percolation threshold is a function of nanowire length (L), radius (R_{NW}) and agglomerate radius (R_{agg}):

$$\Phi_{p,agg} = 1 - \left(1 - \frac{3k'_0 \, L \, R_{NW}{}^2}{4(bc)^{D_f}} \cdot R_{agg}{}^{D_f - 3}\right)^{0.34} \qquad \text{Equation 24}$$

Where, the experimental pre-factor (k'_0) and the fractal dimension (D_f) were found to be 2.04 and 1.8, respectively. The normalisation factor b was proposed and validated to be the volume-equivalent sphere of the monomer:

$$b = \left(\frac{3}{4} R_{NW}{}^2 L\right)^{\frac{1}{3}} \qquad \text{Equation 25}$$

Finally, c, with a value of 5.58, represents the distribution of masses within the volume of the agglomerate and corresponds to the scaling factor between the agglomerate radius of gyration (R_g), and the agglomerate radius (R_{agg}), defined as the radius of the smallest circumference that can enclose the agglomerate. This value was also obtained experimentally.

Although the proposed model was developed using Si nanowires, it provides a reasonable approximation for other FCCVD systems. Therefore, assuming the same values for c, k'_0 and D_f, the percolation threshold for SiC, SnO and CNTs was calculated using mean values of L and R_{NW}. Figure 6.4 illustrates the resulting percolation line (Equation 24) as a function of the mean agglomerate radius, alongside nanowire volumetric concentration calculated from the experimental condition for each system.

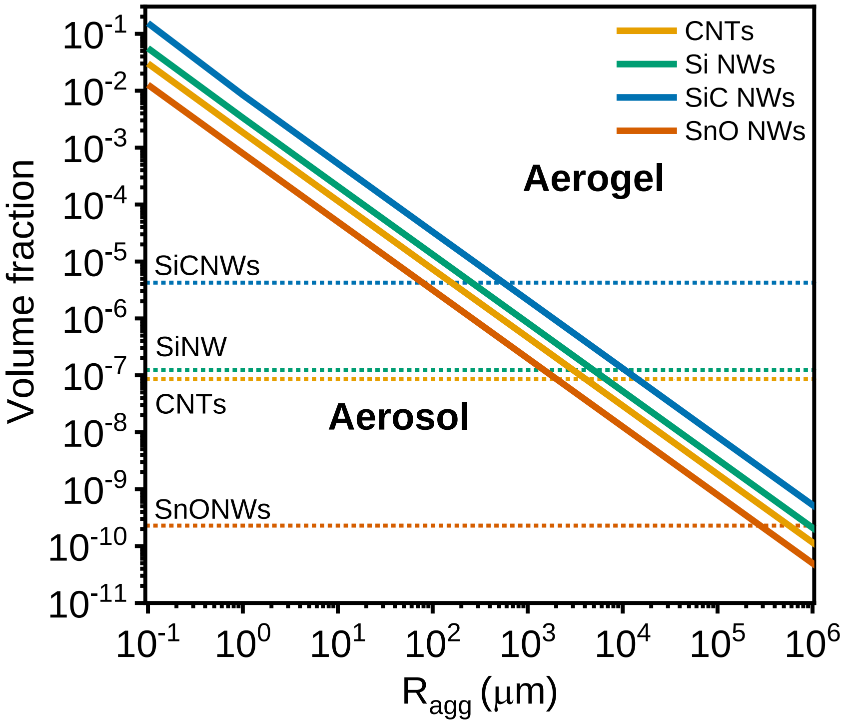

Figure 6.4 Percolation threshold as a function of agglomerate size for SiNW (calculated in ref [103]), CNTs with data from [165], SnO and SiC. The horizontal lines correspond to experimental conditions of volumetric concentration.

Since a systematic study of SiC and SnO aggregates has not yet been conducted, the nanowire volume fraction was estimated assuming full conversion of the catalyst into nanowires and without considering potential flow patterns that could lead to localised concentration increases (4.25×10^{-6} and 2.28×10^{-10}, for SiC and SnO, respectively). Future work will be focused on experimentally determine the agglomerate size distribution and its evolution along the reaction tube. For CNTs, the volumetric fraction corresponds to the conditions that result in aerogel formation (8.55×10^{-8}).[103]

The experimental observations are that all nanowire systems remain in the aerosol form, while CNTs surpass the percolation threshold even under more dilute conditions. This is probably due to the significantly higher aspect ratio of CNTs, almost two orders of magnitude greater than the other nanowires, resulting in larger agglomerate sizes. Following their percolation threshold in Figure 6.4, the agglomerate size can be comparable to the radius of the reactor (3.5 cm).

SiC and Si nanowires show similar behaviour, lying on the aerosol side of the plot. These systems would require higher concentrations or larger average agglomerate sizes to achieve gelation. For example, SiC nanowires are predicted to percolate when the mean agglomerate size reaches 640 µm, equivalent to approximately 4.7×10^5 nanowires, which is within the range of achievable number concentration with the current experimental setup. Nevertheless, the slow collision kinetics prevent the formation of an aerogel. The flow patterns and thermophoretic forces induced by the collecting rod during SiC nanowires synthesis aided the early formation of this aerogel by increasing the local concentration and, thus, probably also the aggregate size by increased interaction between them.

In the case of SnO nanowires, the extremely low concentration and low aspect ratio make aerogel formation unfeasible. For gelation to occur, a mean agglomerate size of 28 cm would be required, which is larger than the reactor tube itself, making aerogel formation impossible under the current synthesis conditions and configuration.

This model represents a significant advancement in describing nanowire assembly in the gas phase and can be easily applied to various systems using measurable parameters such as size and concentration. It is important to highlight that particle size in different systems could further affect the percolation threshold through their effect on the values of D_f and c. However, the model highlights the critical importance of increasing the number concentration, but especially the aspect ratio of 1D particles, to achieve gelation and enable the continuous withdrawal of nanowire fibres from the reactor.

7. Conclusions and Outlook

The primary objective of this thesis was to investigate the viability of extending the FCCVD synthesis method to new materials, using SiC and SnO nanowires as model systems. The successful growth of these nanowires was demonstrated and studied, providing valuable insights into the factors affecting nanowire morphology, precursor conversion, reaction selectivity, and self-assembly into macroscopic networks.

The growth of ultra-long SiC NW provided evidence of the faster growth rates compared with SCVD. This was attributed to a higher impingement rate of precursor species on the catalyst, indicating that growth is limited by incorporation into the catalyst and subsequent solidification of new nanowire layers. The fast growth led to the formation of an aerogel by the high-aspect ratio SiC nanowires, previously observed only for CNTs and BNNTs, suggesting that this is a transversal feature of FCCVD but is prevented by low catalyst concentration and shorter aspect ratios (CNTs are typically an order of magnitude longer).

As our understanding of FCCVD advances, the opportunities to optimise each system become clearer. It was noted that in all FCCVD reactions, selectivity towards 1D nanoparticle formation increases under dilute conditions and seems to be favoured by a reductive atmosphere. Further improvements in SiC nanowire synthesis, could be achieved by using separate precursors for Si and C. This approach aims to control the partial pressure of both species, as they do not participate equally in the growth of SiC nanowires through iron catalysis. According to the calculated Si-C-Fe phase diagram, the catalyst incorporates a larger amount of Si, while C, due to its low solubility, induces solidification. Therefore, using a precursor (HMDS) with a C:Si ratio of 3:1 directly created an excess of C species, which readily forms soot. Silane (SiH_4) and acetylene (C_2H_2), which are used in the synthesis of SiNWs and CNTs, represent a good alternative to replace the current precursor.

In the case of SnO, a broader exploration of temperatures and oxygen precursors is needed to find a wider window of selectivity towards the catalysed reaction without the formation of undesired soot. Nevertheless, even in FCCVD systems where all catalyst is used to form nanowires, as in the case of SnO, the low precursor conversion (in this case, 0.3%) remains a challenge for achieving larger throughput and commercialisation of this method. Although increasing nanowire density is restricted by the catalyst concentration, which has the natural limit of an evolving aerosol, the FCCVD reactions discussed here still have room for improvement before reaching this limit (around 10^9 cm^{-3}). Furthermore, increasing the length of nanowires can improve the material-to-catalyst ratio, enhancing the industrial efficiency of the process. Achieving higher aspect ratios has other positive implications, such as promoting faster agglomeration and increased mechanical stability of the produced networks.

To achieve this, a better understanding of the growth termination process is needed. On the one hand, the thermodynamics of nucleation and termination processes need to be studied in detail, considering the arrangement of species within the catalyst, including factors such as solubility and surface energies. On the other hand, a better understanding of precursor decomposition and the role of the catalyst in this process is required. Future research should focus on acquiring quantitative data to create kinetic models that take into account flow dynamics and catalyst interactions.

Moreover, future efforts should be directed toward controlling uniformity in nanowire morphology and crystal structure. This is a significant challenge given that the diameter distributions of nanowires, all of which are log-normal, are influenced by the self-preserving distribution of the catalyst. Furthermore, the fast growth rates and relatively high pressures used in FCCVD do not facilitate controlled crystal growth. To achieve greater control, the focus should be on the solidification process and how different catalysts can affect it.

Additionally, in this work, the design and construction of the new reactor facilitated a more systematic exploration of the numerous variables influencing the FCCVD process. The modularity of the different parts allowed for adjustments to the design as the synthesis exploration progressed; for example, the need to adjust the injection points was found crucial. Further improvements, such as assessing wall losses and increasing flexibility in the high-temperature sections (e.g., transversal feeding ports), can lead to better control of the growth stages.

Tools such as in-line monitoring, in situ, and continuous sampling were paramount, not only to gather more information faster but also to extrapolate physicochemical information from the acquired data, such as the interaction between precursor and catalyst. In the short term, covering more phenomena in real-time, such as using gas chromatography to assess the decomposition and evolution of gas species, is crucial for continuing to deepen our understanding of this technique.

A major advancement would be the development of in-situ characterisation methods to quantitatively analyse the composition and morphology during 1D nanoparticle growth and aggregation. The primary challenge lies in accessing the reaction zone in typically closed reactors. Furthermore, coupling high-throughput data acquisition (e.g., automation of reaction experiments, online and in-situ characterisation) with data analysis using artificial intelligence could significantly enhance the efficiency of research in FCCVD.

References

1. Dasgupta, N. P. *et al.* 25th anniversary article: Semiconductor nanowires - Synthesis, characterization, and applications. *Adv. Mater.* **26**, 2137–2184 (2014).
2. Devan, R. S., Patil, R. A., Lin, J. H. & Ma, Y. R. One-dimensional metal-oxide nanostructures: Recent developments in synthesis, characterization, and applications. *Adv. Funct. Mater.* **22**, 3326–3370 (2012).
3. Graves, J. E. *et al.* A new procedure for the template synthesis of metal nanowires. *Electrochem. commun.* **87**, 58–62 (2018).
4. Sugime, H. *et al.* Ultra-long carbon nanotube forest via in situ supplements of iron and aluminum vapor sources. *Carbon N. Y.* **172**, 772–780 (2021).
5. Rana, M., Pendashteh, A., Schäufele, R. S., Gispert, J. & Vilatela, J. J. Eliminating Solvents and Polymers in High-Performance Si Anodes by Gas-Phase Assembly of Nanowire Fabrics. *Adv. Energy Mater.* **12**, 2103469 (2022).
6. Li, Y.-L., Kinloch, I. A. & Windle, A. H. Direct Spinning of Carbon Nanotube Fibers from Chemical Vapor Deposition Synthesis. *Science (80-.).* **304**, 276 LP – 278 (2004).
7. Chatterjee, S. *et al.* Syntheses of boron nitride nanotubes from borazine and decaborane molecular precursors by catalytic chemical vapor deposition with a floating nickel catalyst. *Chem. Mater.* **24**, 2872–2879 (2012).
8. Sivakumar, S. *et al.* Aerotaxy: gas-phase epitaxy of quasi 1D nanostructures. *Nanotechnology* **32**, 025605 (2021).
9. Schäufele, R. S., Vazquez-Pufleau, M. & Vilatela, J. J. Tough sheets of nanowires produced floating in the gas phase. *Mater. Horizons* **7**, 2978–2984 (2020).
10. Endo, M. Grow carbon fibers in the vapor phase. *Chemtech* **18**, 568–576 (1988).
11. Bronikowski, M. J., Willis, P. A., Colbert, D. T., Smith, K. A. & Smalley, R. E. Gas-phase production of carbon single-walled nanotubes from carbon monoxide via the HiPco

process: A parametric study. *J. Vac. Sci. Technol. A* **19**, 1800–1805 (2001).

12. Anna Moisala, Albert G Nasibulin & Esko I Kauppinen. The role of metal nanoparticles in the catalytic production of single-walled carbon nanotubes—a review. *J. Phys. Condens. Matter* **15**, S3011 (2003).
13. Zhu, H. W. *et al.* Direct synthesis of long single-walled carbon nanotube strands. *Science (80-.).* **296**, 884–886 (2002).
14. Sehrawat, M. *et al.* Floating catalyst chemical vapour deposition (FCCVD) for direct spinning of CNT aerogel: A review. *Carbon N. Y.* **219**, 118747 (2024).
15. Kim, K. S. *et al.* Hydrogen-catalyzed, pilot-scale production of small-diameter boron nitride nanotubes and their macroscopic assemblies. *ACS Nano* **8**, 6211–6220 (2014).
16. Fathalizadeh, A., Pham, T., Mickelson, W. & Zettl, A. Scaled Synthesis of Boron Nitride Nanotubes, Nanoribbons, and Nanococoons Using Direct Feedstock Injection into an Extended-Pressure, Inductively-Coupled Thermal Plasma. *Nano Lett.* **14**, 4881–4886 (2014).
17. Kim, J. H., Pham, T. V., Hwang, J. H., Kim, C. S. & Kim, M. J. Boron nitride nanotubes: synthesis and applications. *Nano Converg.* **5**, (2018).
18. Nautiyal, P., Zhang, C., Loganathan, A., Boesl, B. & Agarwal, A. Higherature Mechanics of Boron Nitride Nanotube 'buckypaper' for Engineering Advanced Structural Materials. *ACS Appl. Nano Mater.* **2**, 4402–4416 (2019).
19. Heurlin, M. *et al.* Continuous gas-phase synthesis of nanowires with tunable properties. *Nature* **492**, 90–94 (2012).
20. Metaferia, W. *et al.* GaAsP Nanowires Grown by Aerotaxy. *Nano Lett.* **16**, 5701–5707 (2016).
21. Zhang, W. *et al.* Recombination dynamics in aerotaxy-grown Zn-doped GaAs nanowires. *Nanotechnology* **27**, 1–6 (2016).
22. Borgstrom, M. T. *et al.* Towards Nanowire Tandem Junction Solar Cells on Silicon. *IEEE J. Photovoltaics* **8**, 733–740 (2018).
23. Barrigón, E. *et al.* GaAs Nanowire pn-Junctions Produced by Low-Cost and High-Throughput Aerotaxy. *Nano Lett.* **18**, 1088–1092 (2018).
24. Schäufele, R. S., Vazquez-Pufleau, M., Pendashteh, A. & Vilatela, J. J. Controlling reaction paths for ultra-fast growth of inorganic nanowires floating in the gas phase. *Nanoscale* **14**, 55–64 (2022).
25. Feng, J., Biskos, G. & Schmidt-Ott, A. Toward industrial scale synthesis of ultrapure singlet nanoparticles with controllable sizes in a continuous gas-phase process. *Sci. Rep.* **5**, 1–9 (2015).
26. Vazquez-Pufleau, M., Gomez-Palos, I., Arévalo, L., García-Labanda, J. & Vilatela, J. J. Spark_Discharge_Generator_3. *Nano Res.* (Submitted) (2022).
27. Gómez-Palos, I. *et al.* Gas-to-nanotextile: high-performance materials from floating 1D nanoparticles. *Nanoscale* **15**, 6052–6074 (2023).
28. Pfeiffer, T. V., Feng, J. & Schmidt-Ott, A. New developments in spark production of

nanoparticles. *Adv. Powder Technol.* **25**, 56–70 (2014).

29. Boles, S. T., Fitzgerald, E. A., Thompson, C. V., Ho, C. K. F. & Pey, K. L. Catalyst proximity effects on the growth rate of Si nanowires. *J. Appl. Phys.* **106**, (2009).

30. Astié, V., Millon, C., Decams, J.-M. & Bartasyte, A. Direct Liquid Injection Chemical Vapor Deposition. *Chem. Vap. Depos. Nanotechnol.* (2019) doi:10.5772/intechopen.80244.

31. Li, N., Wang, Y. H. A., Iliev, M. N., Klein, T. M. & Gupta, A. Growth of atomically smooth epitaxial nickel ferrite films by direct liquid injection CVD. *Chem. Vap. Depos.* **17**, 261–269 (2011).

32. Khaaissa, Y. *et al.* Ultrasonic Spray-Assisted CVD Growth of Highly Transparent and Conductive Aluminum-Doped ZnO. *Surf. Rev. Lett.* **27**, (2020).

33. Park, S. H. *et al.* Efficient electrospray deposition of surfaces smaller than the spray plume. *Nat. Commun.* **14**, 1–9 (2023).

34. Mathur, S. *et al.* Metal-Organic Chemical Vapor Deposition of Metal Oxide Films and Nanostructures. *Ceram. Sci. Technol.* **3**–**4**, 291–336 (2013).

35. Müller, R. *et al.* Influence of precursor chemistry on morphology and composition of CVD-grown SnO 2 nanowires. *Chem. Mater.* **24**, 4028–4035 (2012).

36. Lee, S. H. *et al.* Deep-injection floating-catalyst chemical vapor deposition to continuously synthesize carbon nanotubes with high aspect ratio and high crystallinity. *Carbon N. Y.* **173**, 901–909 (2021).

37. Sundaram, R. M. Production , Characterisation and Properties of Carbon Nanotube fibres. *A Diss. Submitt. degree Dr. Philos. Univ. Cambridge* 210 (2012).

38. Dubrovskii, V. G., Sibirev, N. V. & Cirlin, G. E. Kinetic model of the growth of nanodimensional whiskers by the vapor-liquid-crystal mechanism. *Tech. Phys. Lett.* **30**, 682–686 (2004).

39. Wacaser, B. A. *et al.* Preferential Interface Nucleation: An Expansion of the VLS Growth Mechanism for Nanowires. *Adv. Mater.* **21**, 153–165 (2009).

40. William D. Callister, J. & Rethwisch, D. G. *Materials Science and Engineering. An Introduction*. (Wiley, 2018).

41. Maliakkal, C. B., Tornberg, M., Jacobsson, D., Lehmann, S. & Dick, K. A. Vapor-solid-solid growth dynamics in GaAs nanowires. *Nanoscale Adv.* **3**, 5928–5940 (2021).

42. Rashad, M. & Geaney, H. Vapor-solid-solid growth of silicon nanowires using magnesium seeds and their electrochemical performance in Li-ion battery anodes. *Chem. Eng. J.* **452**, 139397 (2023).

43. Kodambaka, S., Tersoff, J., Reuter, M. C. & Ross, F. M. Germanium nanowire growth below the eutectic temperature. *Science (80-.).* **316**, 729–732 (2007).

44. Maliakkal, C. B. *et al.* In situ analysis of catalyst composition during gold catalyzed GaAs nanowire growth. *Nat. Commun.* **10**, (2019).

45. Bürger, J. C., Gutsch, S. & Zacharias, M. Extended View on the Vapor-Liquid-Solid Mechanism for Oxide Compound Nanowires: The Role of Oxygen, Solubility, and Carbothermal Reaction. *Journal of Physical Chemistry C* vol. 122 24407–24414 (2018).

46. Persson, A. I. *et al.* Solid-phase diffusion mechanism for GaAs nanowire growth. *Nat. Mater.* **3**, 677–681 (2004).

47. Maliakkal, C. B. *et al.* Independent Control of Nucleation and Layer Growth in Nanowires. *ACS Nano* (2020) doi:10.1021/acsnano.9b09816.

48. Dubrovskii, V. G., Sibirev, N. V, Harmand, J. C. & Glas, F. Growth kinetics and crystal structure of semiconductor nanowires. *Phys. Rev. B* **78**, 235301 (2008).

49. Dubrovskii, V. G. & Hervieu, Y. Y. Diffusion-induced growth of nanowires: Generalized boundary conditions and self-consistent kinetic equation. *J. Cryst. Growth* **401**, 431–440 (2014).

50. Klamchuen, A. *et al.* Study on transport pathway in oxide nanowire growth by using spacing-controlled regular array. *Appl. Phys. Lett.* **99**, 58–61 (2011).

51. Johansson, J. & Magnusson, M. H. From diffusion limited to incorporation limited growth of nanowires. *J. Cryst. Growth* **525**, 125192 (2019).

52. Lu, W. & Lieber, C. M. Semiconductor nanowires. *J. Phys. D. Appl. Phys.* **39**, (2006).

53. Hong, Y. J. & Lee, C.-H. *Semiconductor Nanowires I - Growth and Theory*. *Semiconductors and Semimetals* vol. 93 (2015).

54. Metaferia, W. *et al.* GaAsP Nanowires Grown by Aerotaxy. *Nano Lett.* **16**, 5701–5707 (2016).

55. Mikhalchan, A., Vila, M., Arévalo, L. & Vilatela, J. J. Simultaneous improvements in conversion and properties of molecularly controlled CNT fibres. *Carbon N. Y.* **179**, 417–424 (2021).

56. Boies, A. M. *et al.* Agglomeration Dynamics of 1D Materials: Gas-Phase Collision Rates of Nanotubes and Nanorods. *Small* **15**, 1900520 (2019).

57. Tibbetts, G. G. Vapor-Grown Carbon Fiber Research and Applications: Achievements and Barriers. in *Carbon Filaments and Nanotubes: Common Origins, Differing Applications?* (eds. Biró, L. P., Bernardo, C. A., Tibbetts, G. G. & Lambin, P.) 1–9 (Springer Netherlands, 2001). doi:10.1007/978-94-010-0777-1_1.

58. Heurlin, M. Aerotaxy - A Gas-Phase Nanowire Growth Technique. *PhD Thesis* (Lund University, 2014).

59. Weller, L. *et al.* Mapping the parameter space for direct-spun carbon nanotube aerogels. *Carbon N. Y.* **146**, 789–812 (2019).

60. Kaniyoor, A. *et al.* High throughput production of single-wall carbon nanotube fibres independent of sulfur-source. *Nanoscale* **11**, 18483–18495 (2019).

61. Mas, B. *et al.* Group 16 elements control the synthesis of continuous fibers of carbon nanotubes. *Carbon N. Y.* **101**, 458–464 (2016).

62. Vazquez-Pufleau, M. & Yamane, M. Relative kinetics of nucleation and condensation of silane pyrolysis in a helium atmosphere provide mechanistic insight in the initial stages of particle formation and growth. *Chem. Eng. Sci.* **211**, 115230 (2020).

63. Rodiles, X. *et al.* Carbon nanotube synthesis and spinning as macroscopic fibers assisted by the ceramic reactor tube. *Sci. Rep.* **9**, 9239 (2019).

64. Schäufele, R. S., Vazquez-Pufleau, M., Pendashteh, A. & Vilatela, J. J. Controlling reaction paths for ultra-fast growth of inorganic nanowires floating in the gas phase. *Nanoscale* **14**, 55–64 (2022).

65. Weller, L. *et al.* Mapping the parameter space for direct-spun carbon nanotube aerogels. *Carbon N. Y.* **146**, 789–812 (2019).

66. Ma, Y., Dichiara, A. B., He, D., Zimmer, L. & Bai, J. Control of product nature and morphology by adjusting the hydrogen content in a continuous chemical vapor deposition process for carbon nanotube synthesis. *Carbon N. Y.* **107**, 171–179 (2016).

67. Ding, F., Rosén, A., Campbell, E. E. B., Falk, L. K. L. & Bolton, K. Graphitic encapsulation of catalyst particles in carbon nanotube production. *J. Phys. Chem. B* **110**, 7666–7670 (2006).

68. Aguiar-Hualde, J. M., Magnin, Y., Amara, H. & Bichara, C. Probing the role of carbon solubility in transition metal catalyzing single-walled carbon nanotubes growth. *Carbon N. Y.* **120**, 226–232 (2017).

69. Motta, M., Moisala, A., Kinloch, I. A. & Windle, A. H. High performance fibres from ‘dog bone’ carbon nanotubes. *Adv. Mater.* **19**, (2007).

70. Reguero, V., Alemán, B., Mas, B. & Vilatela, J. J. Controlling Carbon Nanotube Type in Macroscopic Fibers Synthesized by the Direct Spinning Process. *Chem. Mater.* **26**, 3550–3557 (2014).

71. Ghasemi, M., Sundman, B., Fries, S. G. & Johansson, J. The thermodynamic assessment of the Au-In-Ga system. *J. Alloys Compd.* **600**, 178–185 (2014).

72. Ameen, M. *et al.* Liquid Metal Alloy Catalysis – Challenges and Prospects. *ChemCatChem* **15**, (2023).

73. Lu, H. *et al.* Nanoengineering Liquid Metal Core–Shell Nanostructures. *Adv. Funct. Mater.* **34**, 1–11 (2024).

74. Oliveira, D. S. & Cotta, M. A. Role of Group v Atoms during GaAs Nanowire Growth Revealed by Molecular Dynamics Simulations: Implications in the Formation of Sharp Interfaces. *ACS Appl. Nano Mater.* **4**, 2903–2909 (2021).

75. Zhang, B. W., Yang, H. L., Wang, Y. X., Dou, S. X. & Liu, H. K. A Comprehensive Review on Controlling Surface Composition of Pt-Based Bimetallic Electrocatalysts. *Adv. Energy Mater.* **8**, 1–17 (2018).

76. Cai, K. F., Lei, Q. & Zhang, A. X. A Simple Route to Ultra Long SiC Nanowires. *J. Nanosci. Nanotechnol.* **7**, 580–583 (2007).

77. Schmidt, V., Wittemann, J. V., Senz, S. & Gósele, U. Silicon nanowires: A review on aspects of their growth and their electrical properties. *Adv. Mater.* **21**, 2681–2702 (2009).

78. Yang, Y. H., Wu, S. J., Chiu, H. S., Lin, P. I. & Chen, Y. T. Catalytic growth of silicon nanowires assisted by laser ablation. *J. Phys. Chem. B* **108**, 846–852 (2004).

79. Meuller, B. O. *et al.* Review of spark discharge generators for production of nanoparticle aerosols. *Aerosol Sci. Technol.* **46**, 1256–1270 (2012).

80. Vazquez-Pufleau, M. Venturi pump-critical orifice as an online and robust nanoparticle dilution probe for in situ powder stream characterization. *Powder Technol.* **412**, 117974 (2022).

81. Kateris, N., Kloza, P., Qiao, R., Elliott, J. A. & Boies, A. M. From Collisions to Bundles: An Adaptive Coarse-Grained Model for the Aggregation of High-Aspect-Ratio Carbon Nanotubes. *J. Phys. Chem. C* **124**, 8359–8370 (2020).

82. Morimoto, T. *et al.* Length-Dependent Plasmon Resonance in Single-Walled Carbon Nanotubes. *ACS Nano* **8**, 9897–9904 (2014).

83. Gómez-Palos, I. *et al.* Ultrafast synthesis of SiC nanowire webs by floating catalysts rationalised through in situ measurements and thermodynamic calculations. *Nanoscale* **14**, 18175–18183 (2022).

84. Rajesh, J. A. & Pandurangan, A. Extended vapor-liquid-solid growth of silicon carbide nanowires. *J. Nanosci. Nanotechnol.* **14**, 2741–2751 (2014).

85. Young Kim, H., Park, J. & Yang, H. Direct synthesis of aligned silicon carbide nanowires from the silicon substrates. *Chem. Commun.* 256–257 (2003) doi:10.1039/b210027d.

86. Meng, G. *et al.* Chemical Vapor Deposition of β -SiC Nanowires on Granular Active Carbon Cylinders Loaded with Iron Nanoparticles Inside the Pores. *Chinese Phys. Lett.* **15**, 689–691 (1998).

87. Park, B., Ryu, Y. & Yong, K. Growth and characterization of silicon carbide nanowires. *Surf. Rev. Lett.* **11**, 373–378 (2004).

88. Panda, S. K., Sengupta, J. & Jacob, C. Synthesis of β-SiC/SiO 2 core-sheath nanowires by CVD technique using Ni as catalyst. *J. Nanosci. Nanotechnol.* **10**, 3046–3052 (2010).

89. Wu, R. *et al.* Growth of tapered SiC nanowires on flexible carbon fabric: Toward field emission applications. *J. Phys. Chem. C* **116**, 12940–12945 (2012).

90. Zhang, X., Chen, Y., Xie, Z. & Yang, W. Shape and doping enhanced field emission properties of quasialigned 3 C -SiC nanowires. *J. Phys. Chem. C* **114**, 8251–8255 (2010).

91. Zhou, X. T. *et al.* β-SIC nanorods synthesized by hot filament chemical vapor deposition. *Appl. Phys. Lett.* **74**, 3942–3944 (1999).

92. Attolini, G. *et al.* Growth of SiC NWs by vapor phase technique using Fe as catalyst. *Mater. Lett.* **124**, 169–172 (2014).

93. Li, G. *et al.* Large Areas of Centimeters-Long SiC Nanowires Synthesized by Pyrolysis of a Polymer Precursor by a CVD Route. *J. Phys. Chem. C* **113**, 17655–17660 (2009).

94. Liu, X., Zhang, J., Vazquez, A., Wang, D. & Li, S. Mechanistic Study of Thermal Decomposition of Hexamethyldisilane by Flash Pyrolysis Vacuum Ultraviolet Photoionization Time-of-Flight Mass Spectrometry and Density Functional Theory. *J. Phys. Chem. A* **123**, 10520–10528 (2019).

95. Chiu, H. T. & Hsu, J. S. Low pressure chemical vapor deposition of silicon carbide thin films from hexamethyldisilane. *Thin Solid Films* **252**, 13–18 (1994).

96. Bullock, W. J., Walsh, R. & King, K. D. Very-low-pressure pyrolysis of hexamethyldisilane. Kinetic determination of the bond dissociation enthalpy DH°(Me3Si-SiMe3) and

implications for the enthalpy of formation of the trimethylsilyl radical. *J. Phys. Chem.* **98**, 2595–2601 (1994).

97. Cui, M., Lu, H., Jiang, H., Cao, Z. & Meng, X. Phase Diagram of Continuous Binary Nanoalloys: Size, Shape, and Segregation Effects. *Sci. Rep.* **7**, 41990 (2017).

98. Ghasemi, M., Zanolli, Z., Stankovski, M. & Johansson, J. Size- and shape-dependent phase diagram of In-Sb nano-alloys. *Nanoscale* **7**, 17387–17396 (2015).

99. Wilde, G. Structural Phase Transformations in Nanoscale Systems. *Adv. Eng. Mater.* **23**, 2001387 (2021).

100. Granqvist, C. G. & Buhrman, R. A. Ultrafine metal particles. *J. Appl. Phys.* **47**, 2200–2219 (1976).

101. Jamali, V. *et al.* Enhanced ordering in length-polydisperse carbon nanotube solutions at high concentrations as revealed by small angle X-ray scattering. *Soft Matter* **17**, 5122–5130 (2021).

102. Prosa, T. J., Bauer, B. J. & Amis, E. J. From stars to spheres: A SAXS analysis of dilute dendrimer solutions. *Macromolecules* **34**, 4897–4906 (2001).

103. Nabil Abomailek, Isabel Gómez-Palos, Cristian López, María Murillo, Richard Schäufele, Rulan Qiao, A. B. and J. J. V. Fractal scaling in the gas-phase agglomeration of nanowires.

104. Shi, W. *et al.* Laser Ablation Synthesis and Optical Characterization of Silicon Carbide Nanowires. *J. Am. Ceram. Soc.* **83**, 3228–3230 (2000).

105. Zhang, L., Zhuang, H., Jia, C. L. & Jiang, X. Role of catalyst in controlling the growth and morphology of one-dimensional SiC nanostructures. *CrystEngComm* **17**, 7070–7078 (2015).

106. Yu, X. *et al.* Evidence for structural phase transitions induced by the triple phase line shift in self-catalyzed GaAs nanowires. *Nano Lett.* **12**, 5436–5442 (2012).

107. Huang, C. N., Lee, J. Y. & Wang, C. C. On the 2H- to 3C-Type Transformation and Growth Mechanism of SiC Nanowires upon Carbothermal Reduction of Rice Straws. *ACS Omega* **7**, 5039–5052 (2022).

108. Johansson, J., Bolinsson, J., Ek, M., Caroff, P. & Dick, K. A. Combinatorial approaches to understanding polytypism in III-V nanowires. *ACS Nano* **6**, 6142–6149 (2012).

109. Shim, H. W., Zhang, Y. & Huang, H. Twin formation during SiC nanowire synthesis. *J. Appl. Phys.* **104**, (2008).

110. Ito, T., Sano, K., Akiyama, T. & Nakamura, K. A simple approach to polytypes of SiC and its application to nanowires. *Thin Solid Films* **508**, 243–246 (2006).

111. Fissel, A. Thermodynamic considerations of the epitaxial growth of SiC polytypes. *J. Cryst. Growth* **212**, 438–450 (2000).

112. Yu, H. *et al.* Ultraviolet-visible light photoluminescence induced by stacking faults in 3C-SiC nanowires. *Nanotechnology* **30**, (2019).

113. Bechelany, M., Brioude, A., Cornu, D., Ferro, G. & Miele, P. A Raman Spectroscopy Study of Individual SiC Nanowires. *Adv. Funct. Mater.* **17**, 939–943 (2007).

114. Iwanowski, R. J., Fronc, K., Paszkowicz, W. & Heinonen, M. XPS and XRD study of crystalline 3C-SiC grown by sublimation method. *J. Alloys Compd.* **286**, 143–147 (1999).

115. He, J., Sun, B., Sun, Y. & Wang, C. Selective growth of zinc blende, wurtzite and hybrid SiC nanowires: Via a simple chemical vapor deposition route. *CrystEngComm* **21**, 4740–4746 (2019).

116. Todoli, J.-L. & Mermet, J.-M. Pneumatic Nebulizer Design. in *Liquid Sample Introduction in ICP Spectrometry* 17–76 (Elsevier, 2008). doi:10.1016/B978-0-444-53142-1.00003-0.

117. Kashani, A., Bandura, D. & Mostaghimi, J. Spray characterization of pneumatic concentric nebulizer used in Inductively Coupled Plasma – Mass Spectrometry (ICP-MS). *11th Int. Annu. Conf. Liq. At. Spray Syst. 2009, ICLASS 2009* **20**, 415–433 (2009).

118. Foss, W., Li, W., Allen, T. M., Blair, D. S. & Davis, E. J. Studies of toxic aerosols via elastic and inelastic light scattering. *Aerosol Sci. Technol.* **18**, 187–201 (1993).

119. Ravula, S., Larm, N. E., Mottaleb, M. A., Heitz, M. P. & Baker, G. A. Vapor pressure mapping of ionic liquids and low-volatility fluids using graded isothermal thermogravimetric analysis. *ChemEngineering* **3**, 1–12 (2019).

120. Kim, J. H., Jeon, K. M., Park, J. S. & Kang, Y. C. Excellent Li-ion storage performances of hierarchical SnO-SnO2 composite powders and SnO nanoplates prepared by one-pot spray pyrolysis. *J. Power Sources* **359**, 363–370 (2017).

121. Kazemimanesh, M. *et al.* A comparative study on effective density, shape factor, and volatile mixing of non-spherical particles using tandem aerodynamic diameter, mobility diameter, and mass measurements. *J. Aerosol Sci.* **161**, 105930 (2022).

122. Sipkens, T. A. *et al.* Overview of methods to characterize the mass, size, and morphology of soot. *J. Aerosol Sci.* **173**, 106211 (2023).

123. Li, H. *et al.* The gas-phase formation of tin dioxide nanoparticles in single droplet combustion and flame spray pyrolysis. *Combust. Flame* **215**, 389–400 (2020).

124. Shigeno, E., Seki, S., Shimizu, K. & Sawada, Y. Formation Process oflndium Oxide Thin Films from Indium 2-Ethylhexanoate Monohydroxide, ln(OH)(0. **1238**, 1235–1238 (2001).

125. Fang, Z. *et al.* Growth of tin dioxide nanobelts via au-catalytic VLS process. *J. Nanosci. Nanotechnol.* **7**, 4567–4570 (2007).

126. Ge, J. *et al.* Thermodynamic Description of the Au-Sb-Sn Ternary System. *Metals (Basel).* **13**, (2023).

127. Alemán, B., Ranchal, R., Reguero, V., Mas, B. & Vilatela, J. J. Carbon nanotube fibers with martensite and austenite Fe residual catalyst: room temperature ferromagnetism and implications for CVD growth. *J. Mater. Chem. C* **5**, 5544–5550 (2017).

128. Yang, F. *et al.* Zn-doping of GaAs nanowires grown by Aerotaxy. *J. Cryst. Growth* **414**, 181–186 (2015).

129. Bürger, J. C., Gutsch, S. & Zacharias, M. Transition from freestanding SnO2 nanowires to laterally aligned nanowires with a simulation-based experimental design. *Beilstein J. Nanotechnol.* **11**, 843–853 (2020).

130. Leveîque, G. & Abanades, S. Thermodynamic and kinetic study of the carbothermal reduction of SnO 2 for solar thermochemical fuel generation. *Energy and Fuels* **28**, 1396–1405 (2014).

131. Kim, B. S., Lee, J. C., Yoon, H. S. & Kim, S. K. Reduction of SnO2 with hydrogen. *Mater. Trans.* **52**, 1814–1817 (2011).

132. Klamchuen, A. *et al.* Rational Concept for Designing Vapor-Liquid-Solid Growth of Single Crystalline Metal Oxide Nanowires. *Nano Lett.* **15**, 6406–6412 (2015).

133. Zhu, Z. *et al.* Rational Concept for Reducing Growth Temperature in Vapor-Liquid-Solid Process of Metal Oxide Nanowires. *Nano Lett.* **16**, 7495–7502 (2016).

134. Caraveo-Frescas, J. A. & Alshareef, H. N. Transparent p-type SnO nanowires with unprecedented hole mobility among oxide semiconductors. *Appl. Phys. Lett.* **103**, (2013).

135. Jeong, W. & Kang, H. C. Thermal chemical vapor deposition of tin oxide nanowires in a hydrogen reduction atmosphere. *Ceram. Int.* **44**, 9801–9808 (2018).

136. Jang, D. M. *et al.* Tin oxide-carbon nanotube composite for NO X sensing. *J. Nanosci. Nanotechnol.* **12**, 1425–1428 (2012).

137. Knappett, B. R. *et al.* Characterisation of Co@Fe3O4 core@shell nanoparticles using advanced electron microscopy. *Nanoscale* **5**, 5765–5772 (2013).

138. Castro, R. H. R. & Gouvêa, D. The influence of the Chitosan adsorption on the stability of SnO2 suspensions. *J. Eur. Ceram. Soc.* **23**, 897–903 (2003).

139. Zhao, C. *et al.* Shape-selective isolation of Au nanoplates from complex colloidal media by depletion flocculation. *Colloids Surfaces A Physicochem. Eng. Asp.* **568**, 216–223 (2019).

140. Yu, L., Ruan, S., Xu, X., Zou, R. & Hu, J. One-dimensional nanomaterial-assembled macroscopic membranes for water treatment. *Nano Today* **17**, 79–95 (2017).

141. Niu, Y., Li, F., Zhao, W. & Cheng, W. Fabrication and application of macroscopic nanowire aerogels. *Nanoscale* **13**, 7430–7446 (2021).

142. Jaśkaniec, S. *et al.* Solvent engineered synthesis of layered SnO for high-performance anodes. *npj 2D Mater. Appl.* **5**, (2021).

143. Zhang, F., Zhu, J., Zhang, D., Schwingenschlögl, U. & Alshareef, H. N. Two-Dimensional SnO Anodes with a Tunable Number of Atomic Layers for Sodium Ion Batteries. *Nano Lett.* **17**, 1302–1311 (2017).

144. Tibbetts, G. G., Bernardo, C. A., Gorkiewicz, D. W. & Alig, R. L. Role of sulfur in the production of carbon fibers in the vapor phase. *Carbon N. Y.* **32**, 569–576 (1994).

145. Rao, R. *et al.* Revealing the Impact of Catalyst Phase Transition on Carbon Nanotube Growth by in Situ Raman Spectroscopy. *ACS Nano* **7**, 1100–1107 (2013).

146. Kikkawa, J., Ohno, Y. & Takeda, S. Growth rate of silicon nanowires. *Appl. Phys. Lett.* **86**, 1–3 (2005).

147. Dhaka, V. *et al.* High Quality GaAs Nanowires Grown on Glass Substrates. *Nano Lett.* **12**, 1912–1918 (2012).

148. Ramdani, M. R. *et al.* Fast Growth Synthesis of GaAs Nanowires with Exceptional Length. *Nano Lett.* **10**, 1836–1841 (2010).

149. Tang, C., Bando, Y., Sato, T. & Kurashima, K. A novel precursor for synthesis of pure boron nitride nanotubesElectronic supplementary information (ESI) available: (a) experimental apparatus and details; (b) Fig. S2, XRD pattern of BN nanotubes; (c) XRD pattern of the product formed by dispersive Mg a. *Chem. Commun.* **2**, 1290–1291 (2002).

150. Tang, C., Bando, Y. & Sato, T. Catalytic growth of boron nitride nanotubes. *Chem. Phys. Lett.* **362**, 185–189 (2002).

151. E, S. *et al.* Growth of boron nitride nanotubes from magnesium diboride catalysts. *Nanoscale* **10**, 13895–13901 (2018).

152. Pakdel, A., Zhi, C., Bando, Y., Nakayama, T. & Golberg, D. A comprehensive analysis of the CVD growth of boron nitride nanotubes. *Nanotechnology* **23**, 215601 (2012).

153. Huang, Y., Lin, J., Tang, C. & Bando, Y. Bulk synthesis , growth mechanism and properties of highly pure ultrafine boron nitride nanotubes with diameters of sub-10 nm. *Nanotechnology* **22**, 145602 (2011).

154. Lee, C. H., Xie, M., Kayastha, V., Wang, J. & Yap, Y. K. Patterned Growth of Boron Nitride Nanotubes by Catalytic Chemical Vapor Deposition. *Chem. Mater.* **22**, 1782–1787 (2010).

155. Park, B., Ryu, Y. & Yong, K. Growth and characterization of silicon carbide nanowires. *Surf. Rev. Lett.* **11**, 373–378 (2004).

156. Panda, S. K., Sengupta, J. & Jacob, C. Synthesis of β-SiC/SiO 2 core-sheath nanowires by CVD technique using Ni as catalyst. *J. Nanosci. Nanotechnol.* **10**, 3046–3052 (2010).

157. Attolini, G. *et al.* Growth of SiC NWs by vapor phase technique using Fe as catalyst. *Mater. Lett.* **124**, 169–172 (2014).

158. Myung, J. K. *et al.* Double-walled boron nitride nanotubes grown by floating catalyst chemical vapor deposition. *Nano Lett.* **8**, 3298–3302 (2008).

159. Zhang, Q. *et al.* Large-Diameter Carbon Nanotube Transparent Conductor Overcoming Performance–Yield Tradeoff. *Adv. Funct. Mater.* **32**, 2103397 (2022).

160. Ceccarelli, E. & Magnusson, S. M. Aerotaxy-grown GaAs nanowires using Ga seed particles Co-supervisor : Sudhakar Sivakumar Thesis submitted for the degree of Master in Material Science Faculty of science Department of physics. *Master Thesis* (2021).

161. Metaferia, W. *et al.* N-type doping and morphology of GaAs nanowires in Aerotaxy. *Nanotechnology* **29**, (2018).

162. Hoecker, C., Smail, F., Bajada, M., Pick, M. & Boies, A. Catalyst nanoparticle growth dynamics and their influence on product morphology in a CVD process for continuous carbon nanotube synthesis. *Carbon N. Y.* **96**, 116–124 (2016).

163. Ahmad, S. *et al.* Systematic investigation of the catalyst composition effects on single-walled carbon nanotubes synthesis in floating-catalyst CVD. *Carbon N. Y.* **149**, 318–327 (2019).

164. Bae, D. S. *et al.* Spontaneous formation of boron nitride nanotube fibers by boron impurity reduction in laser ablation of ammonia borane. *Nano Converg.* **9**, (2022).

165. Vazquez-Pufleau, M., Torres, R. F., Arevalo, L., Abomailek, N. & Vilatela, J. J. Mapping carbon nanotube aspect ratio, concentration and spinning in FCCVD synthesis controlled by sulphur. *Carbon Trends* **15**, 100355 (2024).

Annexes

Annex 1. Catalytic-CVD grown materials

Material	Family	Group	Material	Family	Group	Material	Family	Group
LiF	Compound	IA-VII	ITO	Oxide	III-IV	Si_3N_4	Nitride	IV-V
CaO	Oxide	IIA	GaAs*	Compound	III-V	PbSe	Compound	IV-V
MgO	Oxide	IIA	GaP	Compound	III-V	PbS	Compound	IV-VI
$Mg_2B_2O_5$	Borate	IIA-III	GaSb	Compound	III-V	SnS	Compound	IV-VI
CaB_6	Hexaboride	IIA-III	InAs	Compound	III-V	PbI_2	Compound	IV-VII
MgB_2	Metallic boride	IIA-III	InAsP	Compound	III-V	Bi_2O_3	Oxide	V
CdO	Oxide	II	InP	Compound	III-V	Sb	Single element	V
ZnO	Oxide	II	InSb	Compound	III-V	Sb_4Te_1	Compound	V-VI
$ZnGa_2O_4$	ternary oxide	II-III	GaN	Nitride	III-V	Bi_2Te_3	Compound	V-VI
Zn_2SnO_4	ternary oxide	II-IV	InN	Nitride	III-V	TeO_2	Oxide	VI
Zn_3P_2	Compound	II-V	AlN	Nitride	III-V	Se	Single element	VI
CdS	Compound	II-VI	BN	Nitride	III-V	W	Single element	TM
CdSe	Compound	II-VI	In_2Se_3	Compound	III-VIB	MoS_2	TM dichalcogenide	TM-VI
CdTe	Compound	II-VI	GaAsP	Compound	III-V-V	HfC	TM carbide	TM-IV
ZnS	Compound	II-VI	$In_3Sb_1Te_2$	Compound	III-V-VI	TiC	TM carbide	TM-IV
ZnSe	Compound	II-VI	SiO_2	Oxide	IV	Fe_2O_3	Oxide	TMO
ZnTe	Compound	II-VI	SnO_2	Oxide	IV	MnO	Oxide	TMO
GaS	Monochalcogenides	III	CNT*	Single element	IV	NiO	Oxide	TMO
Al_2O_3	Oxide	III	Ge	Single element	IV	TiO_2	Oxide	TMO
Ga_2O_3	Oxide	III	Si*	Single element	IV	V_2O_5	Oxide	TMO
In_2O_3	Oxide	III	SiC*	Carbide	IV-IV	WO_3	Oxide	TMO
B	Single element	III	GeSn	Compound	IV-IV	LaB_6	RE hexaboride	RE-III
In	Single element	III	SiGe	Compound	IV-IV	SmB_6	RE hexaboride	RE-III
AlB_2	Boride	III-III	CN	Nitride	IV-V	Eu_2O_3	Oxide	REO
						Sm_2O_3	Oxide	REO

TM(O): Transition metal (oxide), RE(O): Rare-earth oxide *FCCVD grown

Annex 2. SiC Nanowires experimental data

Code	Experimental conditions									SOLID PRODUCTS		
	Sampling method	Sampling position (cm)	T Set Point (ºC)	T real (ºC)	Carrier gas flow (lpm)	Catalyst precursor	Precursor feed rate (ml/h)	Injection aid flow (ml/min)	Injector position (cm)	Solid Product	Colour	Nanowire index
R4_1	Filter	93, centre	1300		3	F	1	20	16	Soot + few nanowire	yellow	1
R4_2	Filter	93, centre	1300		3	F	1	20	16	Soot	grey	0
R4_3	Filter	93, centre	1300		3	F	1	20	16	Soot	grey	0
R4_4	Filter	93, centre	1300		3	F	1	0	16	Soot	grey	0
R4_5	Filter	93, centre	1300		4	F	2	20	16	Soot	grey + yellow	0
R4_6	Filter	93, centre	1300		4	F	1	20	16	Soot	brown	0
R4_7	Filter	93, centre	1300		4	F	1	20	13	Soot + some Nanowires	grey + yellow	1
R4_8	Filter	93, side	1300		4	F	1	25	13	Soot + Nanowires agglomerates	dark yellow	2
R4_9	Filter	93, side	1300		2	F	0.7	60	13	Soot + some Nanowires	dark yellow	1
R4_10	Filter	93, side	1300		2	F	0.5	60	13	Soot	dark yellow	0
R4_11	Filter	93, side	1300		3	F	0.5	60	13	Soot	yellow	0
R4_9	Rod	35	1300	1170	2	F	0.7	60	13	Soot + Nanowires	blue	2
R4_10	Rod	35	1300	1170	2	F	0.5	60	13	Nanowires	blue	2
R4_11	Rod	35	1300	1170	3	F	0.5	60	13	Soot + Nanowires	blue	2
R4_11	Rod	33	1300	1157	3	F	0.5	60	13	Free-standing Nanowires	blue	3
R5_1	Rod	32	1300	1149	3	F	0.5	60	13	Nanowires	blue grey	2
R5_3	Rod	32	1250	1105	3	F	0.5	60	13	Soot + Nanowires	blue grey	2
R5_4	Rod	9	1300	445.5	3	F	0.5	60	13	Spherical particles	yellow	0
R5_4	Rod	21	1300	887	3	F	0.5	60	13	None	black	0
R5_4	Rod	26	1300	1050	3	F	0.5	60	13	Silicon particulate microwires	brown, yellow	0
R5_4	Rod	30	1300	1128	3	F	0.5	60	13	Nanowires	blue	3
R5_4	Rod	60	1300	1175	3	F	0.5	60	13	Soot + one nanowire	white	1

Code	Experimental conditions									SOLID PRODUCTS		
	Sampling method	Sampling position (cm)	T Set Point (°C)	T real (°C)	Carrier gas flow (lpm)	Catalyst precursor	Precursor feed rate (ml/h)	Injection aid flow (ml/min)	Injector position (cm)	Solid Product	Colour	Nanowire index
R5_5	Rod	10.5	1250	492.5	3	F	0.5	60	13	Soot	grey	0
R5_5	Rod	23	1250	930	3	F	0.5	60	13	Big particles	grey	0
R5_5	Rod	27.25	1250	1044	3	F	0.5	60	13	branched thick Nanowires	yellow	1
R5_5	Rod	30	1250	1084	3	F	0.5	60	13	Nanowires	blue	3
R5_5	Rod	30	1250	1084	3	F	0.5	60	13	branched thin Nanowires	blue	0
R5_5	Rod	59	1250	1130	3	F	0.5	60	13	Soot + few nanowire	grey	1
R5_6	Rod	9	1300	445.5	3	F	0.5	150	13	Spherical particles	yellow	0
R5_6	Rod	20.5	1300	867.5	3	F	0.5	150	13	None	black	0
R5_6	Rod	25	1300	1026	3	F	0.5	150	13	Silicon particulate microwires	brown, yellow	0
R5_6	Rod	30	1300	1125	3	F	0.5	150	13	Nanowires	blue	3
R5_6	Rod	59	1300	1157	3	F	0.5	150	13	Soot + few nanowire	grey	1
R5_7	Rod	9	1300	445.5	3	F	1	60	13	Spherical particles	yellow	0
R5_7	Rod	21.5	1300	902	3	F	1	60	13	None	black	0
R5_7	Rod	26	1300	1057	3	F	1	60	13	Silicon particulate microwires	brown, yellow	0
R5_7	Rod	30	1300	1128	3	F	1	60	13	Nanowires	blue	2
R5_7	Rod	58.5	1300	1175	3	F	1	60	13	Soot	white	0
R6_1	Rod	7.5	1300	365	3	F	0.5	60	16	Soot	white	0
R6_1	Rod	18.5	1300	773	3	F	0.5	60	16	None	black	0
R6_1	Rod	476.5	1300	931	3	F	0.5	60	16	Nanowires	blue grey	1
R6_1	Rod	23.5	1300	986.5	3	F	0.5	60	16	Nanowires	granular beige	1
R6_1	Rod	26	1300	1057	3	F	0.5	60	16	Nanowires	granular white	1
R6_1	Rod	29	1300	1115	3	F	0.5	60	16	Thick Nanowires	plain white	1
R6_1	Rod	33	1300	1155	3	F	0.5	60	16	Thick Nanowires	pink	1

Code	Experimental conditions									SOLID PRODUCTS		
	Sampling method	Sampling position (cm)	T Set Point (°C)	T real (°C)	Carrier gas flow (lpm)	Catalyst precursor	Precursor feed rate (ml/h)	Injection aid flow (ml/min)	Injector position (cm)	Solid Product	Colour	Nanowire index
R6_4	Rod	23.5	1300	982	3	SDG	1	80	16	None	black	0
R6_4	Rod	27	1300	1080	3	SDG	1	80	16	None	brown	0
R6_4	Rod	32.5	1300	1146	3	SDG	1	80	16	Nanowires	transparent	3
R6_4	Rod	80	1300		3	SDG	1	80	16	Soot	white	0
R6_5	Rod	11	1300	532	3	SDG	0.5	80	3	Soot	orange	0
R6_5	Rod	23.5	1300	985	3	SDG	0.5	80	3	None	gray	0
R6_5	Rod	25	1300	1033	3	SDG	0.5	80	3	Silicon particulate microwires	brown, yellow	0
R6_5	Rod	27	1300	1081	3	SDG	0.5	80	3	Silicon particulate microwires	white hair	0
R6_5	Rod	28.5	1300	1100	3	SDG	0.5	80	3	None	brown	0
R6_5	Rod	32.5	1300	1150	3	SDG	0.5	80	3	Nanowires	transparent	3
R6_5	Rod	80	1300		3	SDG	0.5	80	3	Soot	gray	0
R7_12	Filter	28	1300	1100	3	F	0.5	60	14	Soot	brown	0
R7_13	Filter	32	1300	1149	3	F	0.5	60	14	Soot + some Nanowires	yellow	1
R7_14	Filter	34	1300	1164	3	F	0.5	60	14	Soot + some Nanowires	yellow	1
R7_15	Filter	32	1300	1149	4	F	0.5	60	14	Soot	yellow	0
R7_16	Filter	32	1300	1149	4	F	0.5	60	11	Soot	yellow	0
R7_18	Filter	32	1300	1149	3	SDG	0.5	60	11	Soot + some Nanowires	yellow	1
R7_19	Filter	32	1300	1149	3	SDG	0.5	60	14	Soot + some Nanowires	yellow	1
R7_20	Filter	32	1300	1149	4	SDG + F	0.5	60	14	Soot + some Nanowires	yellow	2

F = Ferrocene (16 mg/ml)

SDG = Spark Discharge generator (Fe electrodes)

Nanowire index is equivalent to nanowire percentage, 0 = none, 3 = mostly nanowires

All experiments were conducted in 100 H_2 atmosphere

Annex 3. SnO Nanowires experimental data

Code	EXPERIMENTAL INPUTS^b							CONCENTRATIONS				SOLID PRODUCTS			
	Temp.	Catalyst	Precursor nebulisation		Sheath / Dilution	Air injection		Sn	H	O	N	NW (%)	Alloy / core-shell particle (%)	Soot (%NW)	Obs.
	(°C)	Evaporator power (W)	T (°C)	Nom. Injec. (ml/h)	H_2 %	Flow (sccm)	Injection pos. (cm)	%mol	%mol	%mol	%mol				
Alloying															
R1_1	700	422	100	***0***	100	0	0	3.60E-04	100	0	0		100		Alloy. Figure 5.4
R1_2	700	426	100	***0.12***	100	0	0	5.70E-04	100	0	0		100		
R1_3	700	424	100	***0.2***	100	0	0	7.00E-04	100	0	0		100		
R1_4	700	428	100	***0.3***	100	0	0	8.70E-04	100	0	0		100		
Alloying - Precursor concentration															
R2_1	700	422	100	***0.06***	0	0	0	4.70E-04	50	0	50		100		Alloy
R2_2	700	426	50	***0.12***	0	0	0	3.20E-04	50	0	50		100		Alloy - selected
R2_3	700	422	50	***0.25***	0	0	0	5.40E-04	50	0	50		60	40	
R2_4	700	422	50	***0.5***	0	0	0	9.60E-04	50	0	50		50	50	NP favoured
R2_5	700	422	50	***1***	0	0	0	1.80E-03	50	0	50		40	60	NP favoured
Growth - Oxygen concentration															
R3_1	700	412	50	0.12	0	***250***	22	3.00E-04	50	1.3	48.7			100	NP favoured
R3_2	700	298	100	0.15	0	***100***	22	6.00E-04	50	0.5	49.5	20	30	50	Short NW
R3_3	700	298	100	0.15	0	***50***	22	6.10E-04	50	0.3	49.7	85		15	NW lateral growth
R3_4	700	301	100	0.12	0	***20***	22	5.60E-04	50	0.1	49.9	80		20	Short NW - Selected
Growth - Oxygen position															
R4_1	700	270	130	0.12	50	20	***0***	6.80E-04	75	0.1	24.9			100	Decomposition to particles
R4_2	700	270	130	0.12	50	20	***8***	6.80E-04	75	0.1	24.9	5	90	5	NW too short
R4_3	700	270	130	0.12	50	20	***15***	6.80E-04	75	0.1	24.9	60	20	20	-
R4_4	700	270	130	0.12	50	20	***22***	6.80E-04	75	0.1	24.9	90	20	10	Optimum - Selected

Code	EXPERIMENTAL INPUTS[b]							CONCENTRATIONS				SOLID PRODUCTS			
	Temp.	Catalyst	Precursor nebulisation		Sheath / Dilution	Air injection		Sn	H	O	N	NW (%)	Alloy / core-shell particle (%)	Soot (%NW)	Obs.
	(°C)	Evaporator power (W)	T (°C)	Nom. Injec. (ml/h)	H_2 %	Flow (sccm)	Injection pos. (cm)	%mol	%mol	%mol	%mol				
Growth - Oxygen position															
R4_5	700	270	130	0.12	50	20	***30***	6.80E-04	75	0.1	24.9		100		See Figure 5.6
R4_6	700	256	140	0.12	50	20	***34.1***	7.10E-04	75	0.1	24.9		100		
R4_7	700	256	140	0.12	50	20	***41.1***	7.10E-04	75	0.1	24.9		100		
R4_8	700	256	140	0.12	50	20	***48.1***	7.10E-04	75	0.1	24.9		100		
R4_9	700	256	140	0.12	50	20	***55.1***	7.10E-04	75	0.1	24.9		100		
R4_10	700	256	140	0.12	50	20	***62.1***	7.10E-04	75	0.1	24.9		100		
R4_11	700	256	140	0.12	50	20	***69.1***	7.10E-04	75	0.1	24.9		100		
Selectivity control - Length increase															
R5_1	700	***430***	100	0.15	0	20	22	6.10E-04	50	***0.1***	49.9	60	40	5	Nucleation
R5_2	700	***379***	100	0.15	0	20	22	6.10E-04	50	***0.1***	49.9	90		10	Short NW
R6_7	700	***364***	180	0.12	50	20	22	1.10E-03	83.3	0.1	16.5	60		40	-
R5_3	700	***304***	100	0.15	0	20	22	6.10E-04	50	***0.1***	49.9	90		10	Optimal-selected
R6_6	700	***252***	130	0.15	50	20	22	7.30E-04	75	0.1	24.9	30		70	-
R5_4	700	298	***60***	0.12	0	20	22	3.70E-04	50	***0.1***	49.9		100		-
R5_5	700	298	***100***	***0.22***	0	20	22	7.30E-04	***50***	***0.1***	49.9	50		30	Length increase
R5_6	700	298	***120***	0.15	0	20	22	6.90E-04	***50***	***0.1***	49.9	85		15	
R5_7	700	301	100	0.12	0	*20*	22	5.60E-04	50	***0.1***	49.9	80		20	
R5_8	700	302	***130***	0.12	0	20	22	6.80E-04	50	***0.1***	49.9	80		20	
R5_9	700	301	***150***	0.12	8	20	22	7.40E-04	54	***0.1***	45.9	75		25	Optimal-selected
R5_10	700	298	***190***	0.12	0	20	22	8.30E-04	50	***0.1***	49.9			100	NP favoured

Code	EXPERIMENTAL INPUTS^b							CONCENTRATIONS				SOLID PRODUCTS			
	Temp.	Catalyst	Precursor nebulisation		Sheath / Dilution	Air injection		Sn	H	O	N	NW (%)	Alloy / core-shell particle (%)	Soot (%NW)	Obs.
	(°C)	Evaporator power (W)	T (°C)	Nom. Injec. (ml/h)	H_2 %	Flow (sccm)	Injection pos. (cm)	%mol	%mol	%mol	%mol				
Selectivity control - Length increase															
R5_1	700	***430***	100	0.15	0	20	22	6.10E-04	50	***0.1***	49.9	60	40	5	Nucleation
R5_2	700	***379***	100	0.15	0	20	22	6.10E-04	50	***0.1***	49.9	90		10	Short NW
R6_7	700	***364***	180	0.12	50	20	22	1.10E-03	83.3	0.1	16.5	60		40	-
R5_3	700	***304***	100	0.15	0	20	22	6.10E-04	50	***0.1***	49.9	90		10	Optimal-selected
R6_6	700	***252***	130	0.15	50	20	22	7.30E-04	75	0.1	24.9	30		70	-
R5_4	700	298	***60***	0.12	0	20	22	3.70E-04	50	***0.1***	49.9		100		-
R5_5	700	298	***100***	***0.22***	0	20	22	7.30E-04	***50***	***0.1***	49.9	50		30	Length increase
R5_6	700	298	***120***	0.15	0	20	22	6.90E-04	***50***	***0.1***	49.9	85		15	
R5_7	700	301	100	0.12	0	*20*	22	5.60E-04	50	***0.1***	49.9	80		20	
R5_8	700	302	***130***	0.12	0	20	22	6.80E-04	50	***0.1***	49.9	80		20	
R5_9	700	301	***150***	0.12	8	20	22	7.40E-04	54	***0.1***	45.9	75		25	Optimal-selected
R5_10	700	298	***190***	0.12	0	20	22	8.30E-04	50	***0.1***	49.9			100	NP favoured
Selectivity control - Nanoparticles suppression															
R6_1	700	298	100	0.12	0	20	22	5.60E-04	37.5	0.1	62.4			100	Decomposition to particles
R6_2	700	301	150	0.12	25	20	22	7.40E-04	62.5	0.1	37.4	90		10	Optimal-selected
R6_3	700	270	145	0.12	50	20	22	7.20E-04	75	0.1	24.9	90		10	Optimal-selected
R6_4	700	275	140	0.12	50	***100***	22	6.90E-04	75	0.5	24.5	50		50	-
R6_5	700	298	100	0.15	50	20	22	6.10E-04	75	0.1	24.9	80		20	-
R6_8	700	275	140	0.12	100	20	22	7.10E-04	99.9	0.1	0		90	10	Hinder nucleation
R6_9	700	298	100	0.15	100	20	22	6.10E-04	99.9	0.1	0		100		Hinder nucleation
R6_10	700	298	100	0.15	100	**100**	22	6.00E-04	99.5	0.5	0		100		Hinder nucleation

Code	EXPERIMENTAL INPUTS[b]							CONCENTRATIONS				SOLID PRODUCTS			
	Temp.	Catalyst	Precursor nebulisation		Sheath / Dilution	Air injection		Sn	H	O	N	NW (%)	Alloy / core-shell particle (%)	Soot (%NW)	Obs.
	(°C)	Evaporator power (W)	**T (°C)**	**Nom. Injec. (ml/h)**	H_2 %	Flow (sccm)	Injection pos. (cm)	%mol	%mol	%mol	%mol				
Temperature effect															
R7_1	***650***	265.1	140	0.12	50	20	22	7.10E-04	75	***0.1***	24.9			100	Figure 5.11
R7_2	***675***	265.1	140	0.12	50	20	22	7.10E-04	75	***0.1***	24.9			100	
R7_3	***725***	265.1	140	0.12	50	20	22	7.10E-04	75	***0.1***	24.9	15	50	35	
R7_4	***750***	265.1	140	0.12	50	20	22	7.10E-04	75	***0.1***	24.9		100		

Publications:

I. Gómez-Palos, J. J. Vilatela. Gas-phase synthesis of SnOx nanowires by floating catalyst. *Nanoscale*, 2025, *Under review*.

I. Gómez-Palos, M. Vazquez-Pufleau, J. Valilla, Á. Ridruejo, D. Tourret and J. J. Vilatela, Ultrafast synthesis of SiC nanowire webs by floating catalysts rationalised through in-situ measurements and thermodynamic calculations, *Nanoscale*, 2022, *14, 18175–18183*.

I. Gómez-Palos, M. Vazquez-Pufleau, R. S. Schäufele, A. Mikhalchan, A. Pendashteh, Á. Ridruejo and J. J. Vilatela, Gas-to-nanotextile: high-performance materials from floating 1D nanoparticles, Nanoscale, 2023, 15, 6052–6074.

N. Abomailek, I. Gómez-Palos, C. López, M. Murillo, Ri. Schäufele, R. Qiao, A. Boies and J. J. Vilatela, Fractal scaling in the gas-phase agglomeration of nanowires, *Wiley*, 2024, *Under review*.

M. Vazquez-Pufleau, I. Gomez-Palos, L. Arévalo, J. García Labanda and J. J. Vilatela, Spark discharge generator as a stable and reliable nanoparticle synthesis device: Analysis of the impact of process and circuit variables on the characteristics of synthesized nanoparticles, Adv. Powder Technol., 2023, 34, 103955.

Patents (from related previous work):

P20984PC00, Nanowire network, licensed to Floatech for exploitation. Patent application extended to most European countries and over 20 additional countries around the world.

Conferences and events:

I. I. Gómez-Palos, M. Vazquez-Pufleau, J. J. Vilatela. EUROMAT 2023 (Frankfurt, Germany). Oral Presentation. *Nanowire network: Synthesis by floating catalyst and parameter exploration through in situ sampling*

II. La Noche Europea de los Investigadores e Investigadoras de Madrid 2022 (Madrid, Spain). Panel Event. *Las 5 misiones de la UE vistas por los investigadores de IMDEA (I)*

III. I. Gómez-Palos, M. Vazquez-Pufleau, J. Valilla, L. Arévalo, D. Tourret and J.J. Vilatela. III Congreso sobre Materiales Multifuncionales 2022 (Granada, Spain). Oral Presentation. *Nanowire networks formation by floating catalyst synthesis, Case of Study: Silicon Carbide Nanowires*

IV. I. Gómez-Palos, M. Vazquez-Pufleau, J. Valilla, L. Arévalo, D. Tourret and J.J. Vilatela. Nanowire Week 2022 (Chamonix, France). Poster session. *Ultrafast synthesis of SiC nanowire webs by floating catalysts*